A Velocity Decomposition Method For Efficient Numerical Computation of Steady External Flows

by

Deborah Osborn Edmund

A dissertation submitted in partial fulfillment
of the requirements for the degree of
Doctor of Philosophy
(Naval Architecture and Marine Engineering)
in The University of Michigan
2012

Doctoral Committee:

Professor Robert F. Beck, Co-Chair
Assistant Professor Kevin J. Maki, Co-Chair
Professor William W. Schultz
Associate Professor Yin Lu Young

To my family.

ACKNOWLEDGEMENTS

My path through the process of completing this work has been shaped by many people, from professors to family and friends. I am very thankful for the guidance of my advisors, Dr. Kevin Maki and Dr. Robert Beck, in my research, development as an educator, and much more throughout my tenure in the department. I appreciate the knowledge and wisdom they have shared with me over the last few years. I enjoyed working with Dr. William Schultz on an independent research project, and appreciate the insights into academia he provided during that time, as well as his guidance on my thesis work. In addition to her help with my research, I appreciated the chance to briefly be a part of the passionate teaching environment Dr. Julie Young creates for students exploring the field.

The members of my research group and friends in the department have helped me along the way. Bill Rosemurgy was particularly helpful with some of my coding challenges.

The support of my family has played an essential role in my journey at the University of Michigan. I must specifically thank my parents for their love and support, my husband, Steven, for standing by me and encouraging me every step of the way, and my son, Henry, for inspiring me.

I am grateful for the support I received to complete this work from the Department of Defense (DoD) through the National Defense Science & Engineering Graduate Fellowship (NDSEG) Program. This work was also funded by grant numbers N00014-10-1-0301, N00014-11-1-0484, and N00014-05-1-0537.

TABLE OF CONTENTS

CHAPTER

LIST OF FIGURES

Figure

LIST OF TABLES

ABSTRACT

A Velocity Decomposition Method For Efficient Numerical Computation of Steady External Flows

by

Deborah Osborn Edmund

Co-Chairs: Robert F. Beck and Kevin J. Maki

Modeling forces on surface vessels to determine their hydrodynamic performance in the marine environment is integral to vessel design. Many hydrodynamic solution methods exist, ranging from the geometrically simplified strip theory, to inviscid approaches and fully nonlinear unsteady Reynolds-Averaged Navier-Stokes (RANS) solvers. The former approaches are less expensive, but neglect various aspects of the relevant physics including viscous effects and, often, wave breaking. RANS solvers can include viscosity and handle wave breaking; however, they are generally too expensive to be widely utilized at the design stage. The decomposition method presented in this work provides equivalent accuracy to that of RANS solvers, but with decreased computational expense by combining RANS and potential flow solvers to deliver the benefits of each in a unified methodology.

The decomposition method in this work utilizes a Helmholtz-type velocity decomposition to describe the total velocity field as the sum of an irrotational component and a vortical component. Applying the decomposition to the body boundary condition allows the effects of viscosity to be included in the potential velocity field. The viscous-potential-velocity field then fully represents the real fluid velocity everywhere the vorticity has decreased to a negligible level. The computational domain can therefore be reduced to extend just beyond the vortical region surrounding the body and in the wake, with the viscous potential velocity acting as the inlet and farfield boundary conditions for the total fluid velocity. The potential velocity is determined in the infinite-fluid domain using a boundary-element method, and the RANS equations model the total fluid velocity using a finite-volume method.

The velocity decomposition solver developed in this work has matched the accuracy of a RANS solver in decreased computation time for a variety of steady two-dimensional and three-dimensional, laminar and turbulent, external, incompressible flows. The computation time was reduced between 3% and 68% for the cases studied in this thesis.

CHAPTER I

Introduction

Designers and engineers in a wide range of industries rely on modeling fluid flows to aid the design process. Computational Fluid Dynamics (CFD) is used to model fluid flows and gain insight into how ship, airplane, automobile, wind turbine, and many other designs will perform. The benefit to the designer of using a modeling tool increases with the fidelity of the tool and decreases with the amount of time it takes to use the tool. Most of the existing methods to model fluid flow offer either high computational efficiency with lower accuracy or high accuracy with significant computational cost. The method presented in this thesis aims to provide high accuracy at a decreased computational cost.

In the marine industry specifically, modeling forces on surface vessels to determine their hydrodynamic performance in the marine environment is integral to vessel design. Many hydrodynamic solution methods exist, ranging from the geometrically simplified strip theory, to inviscid approaches and fully nonlinear unsteady CFD solvers. The former approaches are less expensive, but neglect various aspects of the relevant physics including viscous effects and, frequently, wave breaking. CFD solvers, such as RANS solvers, can include viscosity and handle wave breaking (Muscari and Di Mascio 2003a, Muscari and Di Mascio 2003b, Rhee and Stern 2002); however, they are generally too expensive to be widely utilized at the design stage.

A large number of evaluations in different sea states and operating conditions are necessary to obtain measures of performance that can guide the design process for a ship in a seaway. At the present time, such computations are prohibitively time consuming except for those performed based on the assumptions of potential flow.

To model high-Reynolds number flows using CFD, models such as the Reynolds-Averaged Navier-Stokes (RANS) equations, large eddy simulations, or detached eddy simulations must be used since all of the relevant scales can not be resolved in a reasonable computation time. Even using one of these CFD models to narrow the range of scales that must be resolved, the spatial discretization of the flow domain can be on the order of tens-of-millions of cells, leading to high computational costs. The decomposition method presented in this work provides equivalent accuracy to that of RANS solvers, but with decreased computational expense by combining RANS and potential flow solvers to deliver the benefits of each in a unified methodology.

The decomposition method in this work utilizes a Helmholtz-type velocity decomposition to describe the total velocity field $\mathbf{u}$ as the sum of an irrotational component that can be expressed as the gradient of a potential, $\nabla\Phi$, and a vortical component $\mathbf{w}$:

$$\mathbf{u} = \nabla\Phi + \mathbf{w} \tag{1.1}$$

This velocity decomposition can be applied to any total velocity solution, $\mathbf{u}$. For a given total velocity, the velocity decomposition is not unique in that an infinite number of irrotational velocities and their corresponding vortical components can be combined to accurately describe the total velocity. The velocity decomposition pursued in this work achieves an irrotational component $\nabla\Phi$ that fully represents the total velocity outside of the vortical regions around a body and in the wake, and therefore drives the vortical component to zero as the vorticity falls to a negligible level.

For high-Reynolds number external flows, the real fluid around a body is rotational, or vortical, in a small region surrounding the body and in the wake. The majority of the flow field outside of this vortical region is irrotational and can be expressed as the gradient of a scalar potential, $\nabla\Phi$, which is the basis for the use of potential flow methods. Frequently, potential flow methods do not include the effects of viscosity in the solution of the potential itself, and for many flows this causes what we call the 'inviscid' potential velocity to not match the real fluid velocity even in the irrotational region. The effect of viscosity around the body and in the wake must be included in the potential velocity for it to represent the true viscous fluid velocity everywhere in the irrotational region. Once this 'viscous' potential velocity is available, it can be used to describe the fluid velocity everywhere outside of the vortical regions around the body and in the wake, allowing the computational domain for the CFD solver to be reduced to include only these vortical regions.

The key is to find the correct potential, Φ. In conventional potential flow methods, the non-penetration condition specifying no flow through the body is met. However, this does not account for the no-slip condition on the body surface that specifies no tangential flow on the body surface due to viscous effects, and consequently gives an incorrect potential, Φ, even in the farfield. The method presented in this thesis develops a new body boundary condition for the potential that depends on the real viscous flow solution.

Applying the decomposition to the body boundary condition allows the effects of viscosity to be included in the potential velocity field. The viscous-potential-velocity field then fully represents the fluid velocity outside of the vortical region surrounding the body and in the wake. The computational domain can therefore be reduced to extend just beyond the vortical region. The decomposition is applied to the inlet and farfield boundaries, and since the vortical velocity is negligible on these boundaries, the fluid velocity is set equal to the viscous potential velocity. The potential velocity is determined in the infinite-fluid domain with a boundary-element method and the RANS equations are used to model the total fluid velocity with a finite-volume method.

Decreasing the computational domain increases the computational efficiency. The solver itself requires less computation time since the number of unknowns in the field discretization used to solve the RANS equations is significantly reduced. While the velocity decomposition solver implemented in this work includes steps to calculate the potential velocity and update the boundary conditions that the RANS solver does not include, these steps are less computationally expensive than running the RANS solver on the larger domain. Another significant source of time savings comes from the reduced effort required to generate meshes for smaller domains. The quality of the spatial discretization of the fluid domain in the form of a mesh directly impacts the quality of the solution. Generating appropriate meshes can be time consuming and challenging. Reducing the size of the domain generally makes the mesh generation process faster and less challenging as it is easier to maintain high quality cells throughout the domain.

While the required computational domain is limited to surrounding the vortical region around the body and in the wake, the flow solution is available everywhere in the infinite fluid region through the viscous potential velocity. The viscous potential velocity includes the effects of viscosity around the body and hence fully represents the fluid velocity everywhere outside of the vortical region. One possible application of this feature is problems with multiple bodies. Rather than discretizing the fluid flow in a large domain that encompasses all of the bodies, the flow could be modeled in small domains surrounding each body individually. The influence of each body on the others would be included through the viscous potential velocity which would calculate the velocity at any given point by including the influence of the singularity elements from all of the bodies. The RANS solution around each body would receive the influence of the other bodies through the inlet and farfield boundary conditions where the fluid velocity is set equal to the viscous potential velocity.

The velocity decomposition method presented also offers a theoretical advancement to including the effects of the viscous boundary layer in the calculation of the potential flow. The derivation of the modified body boundary condition necessary to include the viscous effects in the potential velocity presented by Morino (1986) offers improvements in accuracy and applicability from Lighthill's equivalent source method (1958). The inclusion of viscous effects through the modified body boundary condition also works for flows with thick boundary layers and separation. The work in this thesis is strongly motivated by Morino's development, and implements and demonstrates the effectiveness of including the viscous effects in this way.

The ultimate applications of the velocity decomposition method presented are three-dimensional bodies moving at high Reynolds numbers through a free surface. In this work, the velocity decomposition method is developed for and demonstrated on two-dimensional and three-dimensional deeply submerged bodies in steady laminar and turbulent flows.

1.1 Background

The benefits of coupling viscous and inviscid solvers have led many to explore this field. Two fairly straightforward applications are improving the potential velocity solution by including the influence of the viscous boundary layer through methods such as Lighthill's displacement thickness (Lighthill 1958), or improving the RANS solution by using the potential velocity as the inlet and farfield boundary conditions on reduced domains where the free-stream velocity is less applicable (for example, Eça and Hoekstra 2009). Another approach is to decompose the domain into an area around the body and wake, where the viscous equations are solved, and the remaining irrotational domain, where the potential equations apply. This domain decomposition technique imposes an artificial boundary between the two solution methods that can be problematic. The current work focuses on decomposing the velocity rather than the domain, which has also been investigated with promising results.

Kendon et al. (2003) applies the Helmholtz-type decomposition of the velocity vector shown in Equation 1.1 in a numerical procedure for wave-body interaction problems dominated by diffraction forces with viscous shear forces important to the calculation of the response motion. First, a boundary-element technique utilizing linearized boundary conditions on the mean free surface in the frequency domain is used to solve for the potential from the wave-body problem. The potential is then transferred to the time domain where the rotational velocity component is calculated. This two-dimensional numerical method has yielded promising results for a submerged circular cylinder close to the free surface. While this method uses different solution techniques than the currently proposed method, it demonstrates the usefulness of the decomposition in free-surface applications which are the ultimate application. The proposed method offers an improvement to Kendon's work by seeking an improved velocity decomposition where the potential solution drives the rotational component to zero in the majority of the computational domain.

The SWENSE (Spectral Wave Explicit Navier-Stokes Equations) approach presented by Luquet et al. (2004) and Luquet et al. (2007) provides another numerical approach to modeling wave-body interactions utilizing the strengths of both potential flow formulations and RANS formulations. The SWENSE method decomposes the primitive variables, velocity and pressure, and the free-surface elevation into incident and diffracted components. The regular incident wave field is modeled using an algorithm based on stream function theory and the irregular incident wave field is modeled using a Higher Order Spectral scheme. The diffracted component, or the difference between the total field and the incident field, is solved for using a modified form of the RANS equations. Using potential flow theory to calculate the incident wave field is highly accurate and efficient, while the use of RANS to solve for the diffracted flow allows the inclusion of viscous effects. Summing the incident and diffracted components then provides the overall flow field desired. The SWENSE method has been successfully applied to a ship in regular waves with forward speed and a tension leg platform in waves, among other bodies. The decomposition of the flow field into components described by potential flow and the RANS equations is very similar to the approach presented here. The main difference between the SWENSE method and the current method is that the current method includes viscous effects in the potential flow in order to reduce the flow domain. The viscous flow does not influence the potential flow in the SWENSE method. Also, the current method does not solve the decomposed equations, which are more computationally expensive.

Hafez et al. combines a modified domain decomposition technique with a Helmholtz-type velocity decomposition to simulate steady laminar incompressible two-dimensional flows with promising success (Hafez et al. 2006 and Hafez et al. 2007). A modified form of the momentum balance equations are used to solve for the rotational velocity component only inside the boundary layer, the extent of which is conservatively defined prior to the calculations. The potential flow is solved everywhere in the domain by setting the Laplacian of the potential equal to the divergence of the rotational velocity, satisfying the continuity equation. The potential solution then essentially represents a set of sources in the viscous boundary layer, creating a potential velocity field that includes viscous effects around the body. Since the potential velocity field is based on the rotational velocity and calculated continuously in the domain, it eliminates the problematic interface between the potential and the viscous solutions found in many domain decompositions.

An analytical discussion of the velocity decomposition can be found in Morino's work. Morino has been exploring the application of a decomposition of the general form shown in Equation 1.1 to analyze viscous incompressible flows, primarily with limited vortical regions around the body and in the wake (Morino 1986, 1994, 2003, Morino et al. 1995, Morino et al. 1999). Morino uses this decomposition to solve for the flow given a vorticity field using the boundary integral method to determine the potential velocity. This method offers the benefit of eliminating the pressure in the vorticity transport equations; however, the boundary conditions in the vorticity formulation are not physically straightforward. The current method uses a primitive variable formulation with easier-to-specify boundary conditions than the vorticity formulation.

The current effort originated with the work presented in Kim et al. (2005). Kim uses the Helmholtz-type velocity decomposition to derive the complementary RANS equations by substituting the decomposed velocity into the Navier-Stokes equations for the total velocity. The complementary RANS equations are similar to the modified form of the momentum equations used by Hafez et al. (2006 and 2007). Given a potential field, the complementary RANS equations can be solved for the corresponding rotational velocity and the total velocity can be constructed as the sum of the potential and rotational parts. Kim notes that the decomposition is not unique; the rotational velocity component is dependent on the potential field. Since the goal is to minimize the computational domain of the RANS equations for the rotational velocity, a potential field that most closely captures the total velocity field outside the boundary layer and wake is desired. Kim achieved good results using this method for both laminar and turbulent flows. However, he found that the complementary RANS solution method did not reduce the computation time when compared to RANS due to the inability to decrease the computational domain.

The complementary RANS equations were implemented early on in the current efforts. The finding of Kim et al. (2005) was reproduced; while the complementary RANS equations function well, they do not provide computational savings. Including the effects of viscosity in the potential flow is essential to being able to reduce the computational domain; the potential velocity that satisfies the non-penetration body boundary condition will not fully represent the real fluid velocity at finite distances from the body where the vorticity has decreased to a negligible level. The process of including the viscous effects relies on the velocity decomposition, but does not require the complementary velocity to be solved for directly. Using the RANS equations to solve for the total fluid velocity and expressing the complementary velocity as the difference between the fluid velocity and the viscous potential velocity rather than solving the complementary RANS equations for the complementary velocity is more efficient since it eliminates the additional term introduced by decomposing the momentum equation.

As Kim et al. (2005) noted, the velocity decomposition is not unique for a given total velocity. To reduce the computational domain, the current work seeks a velocity decomposition in which the vortical component goes to zero as the vorticity decreases to a negligible level away from the body and wake. For the vortical component to go to zero, the irrotational potential velocity must fully represent the total fluid velocity outside of the boundary layer and wake. The potential velocity must therefore include the effects of the viscous boundary layer and wake.

Lighthill presented four possible methods to account for viscous effects in the potential velocity solution including flow reduction, equivalent sources, velocity comparison, and mean vorticity (Lighthill 1958). The equivalent source method distributes sources on the body surface to push the inviscid streamlines outward to match the viscous boundary layer thickness, and has since been called the transpiration velocity to reflect the apparent flow through the body surface.

Lemmerman and Sonnad (1979) affectively used a surface transpiration in an inviscid three-dimensional panel method iteratively corrected by a two-dimensional integral boundary layer method. The boundary layer method is used to determine the boundary layer thickness, and then the surface transpiration necessary to impose that boundary layer thickness is added to the three-dimensional panel method

(Lemmerman and Sonnad 1979).

Morino presents an exact formulation for Lighthill's equivalent source method in the context of his velocity decomposition (Morino 1986, 2003, Morino et al. 1995, Morino et al. 1999). In addition, he shows that the divergence of the defect velocity, or the difference between the total velocity and the potential velocity due to vorticity, can be integrated along the body normal to provide an exact equation for the transpiration velocity which is a generalized form of Lighthill's result (Morino 1986). This formulation has strongly motivated the inclusion of viscous effects in the potential flow which is central to this work.

1.2 Objectives

The objectives stated at the outset of this research were to:

1. Develop and implement an improved velocity decomposition by finding a potential velocity solution which minimizes the extent of the vortical velocity and therefore allows the computational domain to be significantly reduced.

2. Extend the velocity decomposition method to turbulent flows through the use of existing turbulence models.

3. Extend the solver to three-dimensional and/ or free-surface flows around simple bodies as time permits.

The completion of each of these objectives is described in this thesis, with the exception of extending the solver to free-surface flows, which is also being done with promising results (Rosemurgy et al. 2012).

The governing equations, boundary conditions, and velocity decomposition are presented in Chapter 2. Chapter 3 describes the numerical implementation of the

RANS equations using a finite-volume method, the potential flow using a boundary-element method, and the algorithm that implements the velocity decomposition approach to interface the two solutions.

Chapter 4 presents two-dimensional laminar flows over a flat plate, a circular cylinder, and a NACA 0012 airfoil. Turbulent flows over a flat plate and a NACA 0012 airfoil are presented in Chapter 5. Three-dimensional laminar and turbulent flows over the Afterbody 1 are presented in Chapter 6 and the turbulent results are compared to experimental data (Huang et al. 1978). The contributions of this work, and possible areas of future work are discussed in Chapter 7.

CHAPTER II

Mathematical Formulation

Steady incompressible external flows are considered in this thesis. The governing equations for the total fluid velocity, $\mathbf{u}$, and the irrotational potential velocity, $\nabla\Phi$, are presented in this chapter, along with their conventional boundary conditions. The velocity decomposition is then restated and applied to the body boundary condition, allowing the viscous effects in the fluid velocity $\mathbf{u}$ to be included in the viscous potential velocity. The velocity decomposition is also applied to the inlet and farfield boundary conditions.

A diagram of a general flow domain is shown in Figure 2.1 with the positive $x-$axis aligned with the free-stream velocity, the $y-$axis perpendicular to the $x-$axis, and the positive $z-$axis pointing out of the paper according to the right-hand rule. The origin is generally aligned with either the leading edge of the body as shown here, or the center of the body. The inlet, farfield, outlet, and body boundaries are labeled for reference.

2.1 RANS Equations

The governing equations for the fluid velocity $\mathbf{u}$ are found by simplifying the conservation equations for mass and momentum with the assumptions that the flow does not vary in time, and has constant density and viscosity. These simplifications

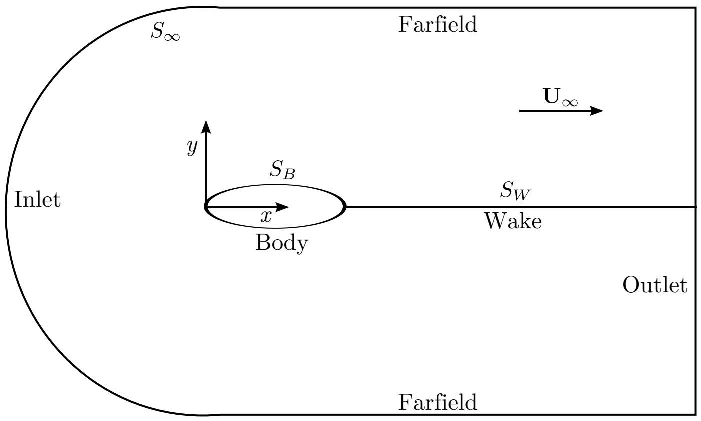

Figure 2.1: General flow domain showing orientation of the global coordinate system and the boundary surface labels.

lead to the continuity equation and the steady incompressible Navier-Stokes equation as shown in Equations 2.1 and 2.2.

$$\nabla \cdot \mathbf{u} = 0 \tag{2.1}$$

$$\nabla \cdot \mathbf{u}\mathbf{u} = -\frac{\nabla p}{\rho} + \nu \nabla^2 \mathbf{u} \tag{2.2}$$

where p is the dynamic pressure, ρ is density, and ν is kinematic viscosity. The total pressure P equals the dynamic pressure plus the static pressure, $P = p + \rho \mathbf{g} \cdot \mathbf{x}$, where $\mathbf{g}$ represents the gravitational body forces and $\mathbf{x}$ is a position vector.

The Reynolds-Averaged Navier-Stokes (RANS) equations are used to model turbulent flows in this work. The velocity and pressure variables in Equations 2.1 and 2.2 are expressed as the sum of a mean, $\overline{\mathbf{u}}$ and $\overline{p}$, plus a fluctuating component, $\mathbf{u}'$ and p'. Taking the Reynolds time average of the resulting equations, dropping the bars indicating the average on all but the new term, and re-arranging leads to the RANS equations, as shown in Equations 2.3 and 2.4. Note that the average of the mean equals the mean and the average of the fluctuating component equals zero.

$$\nabla \cdot \mathbf{u} = 0 \tag{2.3}$$

$$\nabla \cdot \mathbf{u}\mathbf{u} = -\frac{\nabla p}{\rho} + \nabla \cdot [\nu(\nabla \mathbf{u} + \nabla \mathbf{u}^{\mathrm{T}})] - \nabla \cdot \overline{\mathbf{u}'\mathbf{u}'} \tag{2.4}$$

Here, p is the time-averaged dynamic pressure, and $\mathbf{u}$ is the time-averaged velocity vector. The resulting continuity equation for the time averaged fluid velocity vector is identical to the instantaneous form shown in Equation 2.1. The momentum equation is also the same as the instantaneous form, with the addition of the term $\nabla \cdot \overline{\mathbf{u}'\mathbf{u}'}$, which arises from averaging the fluctuating components of the convection term. The Boussinesq approximation is used to express this new term, which represents the transfer of momentum due to turbulence, using an eddy viscosity model as shown in Equation 2.5.

$$-\overline{\mathbf{u}'\mathbf{u}'} = \nu_t(\nabla \mathbf{u} + \nabla \mathbf{u}^{\mathrm{T}}) - \frac{2}{3}k\mathbf{I} \tag{2.5}$$

where ν_t is the kinematic eddy viscosity, $k = 1/2\,\mathrm{tr}(\overline{\mathbf{u}'\mathbf{u}'})$ is the turbulent kinetic energy, and $\mathbf{I}$ is the identity matrix. Including the expression in Equation 2.5 in Equation 2.4 results in Equation 2.6, where the turbulent kinetic energy is included in the pressure.

$$\nabla \cdot \mathbf{u}\mathbf{u} = -\frac{\nabla p}{\rho} + \nabla \cdot [(\nu + \nu_t)(\nabla \mathbf{u} + \nabla \mathbf{u}^{\mathrm{T}})] \tag{2.6}$$

Equations 2.3 and 2.6 will be referred to as the RANS equations throughout this thesis. Please note that the working variables $\mathbf{u}$ and p represent both the instantaneous value in laminar cases, where the instantaneous Navier-Stokes equations apply, and the time-averaged value in turbulent cases, where the RANS equations apply. The solvers in this work use the RANS equations with a user-specified turbulence model to solve for the kinematic eddy viscosity, ν_t. In laminar cases, the turbulence model is turned off, essentially removing the eddy viscosity from the RANS equations and making them function as Navier-Stokes equations.

2.1.1 Turbulence Model

The velocity decomposition approach applied in the current solver should be independent of the turbulence model for the kinematic eddy viscosity, ν_t. For the sake of demonstrating the performance of the solver on turbulent flows, the $k-\omega$ Shear Stress Transport (SST) turbulence model developed by Menter (1994, 1996) and Menter et al. (2003) has been used. The $k-\omega$ SST model uses blending functions to utilize the accuracy of the $k-\omega$ model, which solves governing equations for the turbulent kinetic energy k and the specific dissipation rate ω, as formulated by Wilcox (2006) in near wall layers and the lower sensitivity to free-stream values of the $k-\epsilon$ model, which solves governing equations for the turbulent kinetic energy k and the dissipation rate ϵ. The model's ability to handle strong adverse pressure gradients and separation, combined with its accuracy and robustness, has caused it to become common in industrial, commercial, and research codes (Menter et al. 2003).

2.1.2 Conventional RANS Boundary Conditions

The fluid velocity $\mathbf{u}$ is subject to the no-slip boundary condition on the body, as shown in Equation 2.7 for a fixed body.

$$\mathbf{u}\big|_{\text{body}} = 0 \tag{2.7}$$

At the inlet and farfield boundaries, the velocity is often set equal to the free-stream value; this boundary condition is modified using the velocity decomposition as described in Section 2.3.2.

$$\mathbf{u}\big|_{\text{inlet \& farfield}} = \mathbf{U}_\infty \tag{2.8}$$

The velocity boundary condition at the outlet boundary is zero normal gradient. The pressure boundary conditions on the body, inlet, and farfield boundaries are also zero normal gradient. The pressure at the outlet is set to zero to serve as the reference pressure. While these pressure boundary conditions are frequently used, pressure boundary conditions are still a debated topic (Gresho and Sani 1987, Sani et al. 2006, Rempfer 2006, and Rempfer 2008).

For turbulent flows, the turbulent kinetic energy, k, and the specific dissipation rate, ω, are set equal to their free-stream values on the inlet and farfield boundaries. The outlet boundary condition for the turbulent kinetic energy and specific dissipation rate is zero normal gradient. The kinematic eddy viscosity, ν_t, is initially set equal to the free-stream value, then calculated on the inlet, farfield, and outlet boundaries. Wall functions model each of the turbulent quantities on the wall and in the first cell so that the viscous sublayer does not need to be resolved by the mesh. The first mesh point away from the wall is placed in the log layer, where the law of the wall applies.

2.2 Velocity Potential

The irrotational potential velocity can be expressed in terms of the gradient of a scalar potential, $\nabla\Phi$. Since the flow is incompressible, substitution into the continuity equation leads to the Laplace equation. While the irrotational and vortical velocity components could have counteracting divergence to maintain a divergence-free total fluid velocity, this does not seem to offer any benefit and has not been pursued. The Laplace equation is then the governing equation for both the inviscid and viscous potential flow:

$$\nabla^2\Phi = 0 \tag{2.9}$$

2.2.1 Conventional Potential Boundary Conditions

The Laplace equation in the volume surrounding the body is subject to boundary conditions on the body and far from the body. The inviscid potential velocity is subject to the non-penetration boundary condition, which states that the velocity normal to a solid surface must be zero. In a body-fixed reference frame this is expressed as

$$\nabla\Phi \cdot \mathbf{n}\big|_{\text{body}} = 0 \tag{2.10}$$

This non-penetration body boundary condition is modified using the velocity decomposition as described in Section 2.3.2 to achieve the viscous potential velocity.

The radiation condition for an infinite fluid requires the disturbance due to the body to decay as the distance, r, from the body increases, and hence the velocity to return to the undisturbed velocity far from the body, as shown in Equation 2.11.

$$\lim_{r\to\infty} (\nabla\Phi - \mathbf{U}_\infty) = 0 \tag{2.11}$$

2.3 Velocity Decomposition

The velocity decomposition method utilizes a Helmholtz-type velocity decomposition to describe the total velocity field $\mathbf{u}$ as the sum of an irrotational component $\nabla\Phi$ and a vortical component $\mathbf{w}$, as stated in Equation 1.1, and re-stated here:

$$\mathbf{u} = \nabla\Phi + \mathbf{w} \tag{2.12}$$

For a given total velocity, this velocity decomposition is not unique. We seek the decomposition that drives the vortical velocity $\mathbf{w}$ to zero as the vorticity falls to a negligible value outside of the boundary layer and wake. The desired decomposition will therefore be found if the irrotational potential velocity matches the fluid velocity outside of the vortical region. For the potential velocity to fully represent the fluid velocity outside of the vortical region, it must include the effects of the viscous boundary layer and wake.

Applying the decomposition to the body boundary condition allows the effects of viscosity to be included in the potential-velocity field. This ‘viscous potential’ velocity then fully represents the fluid velocity outside of the vortical region surrounding the body and in the wake, and hence the vortical velocity is negligible. If the inclusion of viscous effects through the body boundary condition is successful, the computational domain can be reduced to extend just beyond the vortical region, as will be demonstrated for a variety of flows in Chapters IV, V, and VI. The decomposition can then be applied to the inlet and farfield boundaries, and since the vortical velocity is negligible, the fluid velocity is set equal to the viscous potential velocity on those boundaries. The details of the application of the velocity decomposition to the boundaries are described in the following sections.

2.3.1 Velocity Decomposition of the Body Boundary Condition

The viscous potential developed in this work uses the velocity decomposition to modify the non-penetration potential velocity body boundary condition in order to include the effects of viscosity in the calculation of the irrotational potential velocity. The total velocity $\mathbf{u}$ is subject to the no-slip boundary condition on the body, as shown in Equation 2.7 for a fixed body. Applying the velocity decomposition to the no-slip body boundary condition for $\mathbf{u}$ indicates the irrotational velocity $\nabla\Phi$ must be equal and opposite to the vortical velocity $\mathbf{w}$ on the body, as shown by the progression from Equation 2.13 to Equation 2.14.

$$\mathbf{u}\big|_{\text{body}} = \nabla\Phi\big|_{\text{body}} + \mathbf{w}\big|_{\text{body}} = 0 \tag{2.13}$$

$$\nabla\Phi\big|_{\text{body}} = -\mathbf{w}\big|_{\text{body}} \tag{2.14}$$

Taking the normal component of Equation 2.14 provides the new body boundary condition for the viscous potential in terms of the normal component of the vortical velocity on the body:

$$\left.\frac{\partial\Phi}{\partial n}\right|_{\text{body}} = -(\mathbf{w}\cdot\mathbf{n})\big|_{\text{body}} = -w_n(0) \tag{2.15}$$

The final term, w_n, expresses the normal component of the vortical velocity in a local orthogonal coordinate system on the body surface aligned with the normal pointing out of the body into the fluid.

The flow 'through' the body boundary is how the viscous effects are included in the viscous potential velocity, and has been suggested in various forms since Lighthill introduced the equivalent source method (1958). Based on the nature of having an apparent flow through the body surface, this approach has since been called a 'transpiration velocity.' The versions proposed by Lighthill as an equivalent source method (1958) and subsequent users, such as Lemmerman and Sonnad (1979), are based on the continuity equation and include approximations. Morino (1986, Appendix C) offers a theoretical presentation of an improved formulation. His formulation is based on the solenoidal nature of the 'defect velocity,' as he calls the difference between the fluid velocity and the potential velocity, since he defines it as the contribution due to a vector potential. This allows the formulation to theoretically hold for unsteady, compressible, and separated flows. We limit our current definition of the vortical velocity to incompressible flows where the continuity equation enforces zero divergence, but note the possibility of extension to compressible flows. As shown below, following the formulation from Morino provides an expression for the normal component of the vortical velocity on the body, as needed in the body boundary condition for the viscous potential velocity given by Equation 2.15. The novel implementation of this body boundary condition for the viscous potential velocity is explored and demonstrated in this work.

In the incompressible cases considered in this work, conservation of mass dictates that the fluid velocity **u** must be divergenceless. The irrotational component is also divergence free, and hence the vortical component must also be divergenceless. The resulting continuity equation for the vortical component **w** is expressed in Equations 2.16 and 2.17, where the latter expression is written in a local coordinate system.

$$\nabla \cdot \mathbf{w} = 0 \tag{2.16}$$

$$\frac{\partial w_n}{\partial n} + \frac{\partial w_{t_1}}{\partial t_1} + \frac{\partial w_{t_2}}{\partial t_2} = 0 \tag{2.17}$$

In the local orthogonal coordinate system, n is aligned with the normal pointing out of the body into the fluid, and t_1 and t_2 are aligned with two in-plane tangent vectors. The subscripts n, t_1, and t_2 denote the component in the corresponding direction.

Integrating the divergence of the vortical velocity in the normal direction through the vortical region leads to Equation 2.18, which can be simplified to Equation 2.19, and rearranged to yield Equation 2.20.

$$\int_0^\delta \left(\frac{\partial w_n}{\partial n} + \frac{\partial w_{t_1}}{\partial t_1} + \frac{\partial w_{t_2}}{\partial t_2} \right) dn = 0 \tag{2.18}$$

$$\int_0^\delta \left(\frac{\partial w_{t_1}}{\partial t_1} + \frac{\partial w_{t_2}}{\partial t_2} \right) dn + w_n(\delta) - w_n(0) = 0 \tag{2.19}$$

$$w_n(0) = \int_0^\delta \left(\frac{\partial w_{t_1}}{\partial t_1} + \frac{\partial w_{t_2}}{\partial t_2} \right) dn + w_n(\delta) \tag{2.20}$$

The upper limit of the integration, δ, is outside of the vortical region. Since we seek a vortical velocity, **w**, that goes to zero where the vorticity is negligible, we desire that $w_n(\delta) = 0$, in which case

$$w_n(0) = \int_0^\delta \left(\frac{\partial w_{t_1}}{\partial t_1} + \frac{\partial w_{t_2}}{\partial t_2} \right) dn \tag{2.21}$$

Substituting Equation 2.21 into Equation 2.15, results in the following expression for the normal component of the potential velocity on the body in terms of the vortical velocity.

$$\left.\frac{\partial \Phi}{\partial n}\right|_{\text{body}} = -\int_0^\delta \left(\frac{\partial w_{t_1}}{\partial t_1} + \frac{\partial w_{t_2}}{\partial t_2} \right) dn \tag{2.22}$$

For convenience we define

$$f(\mathbf{w}) = -\int_0^\delta \left(\frac{\partial w_{t_1}}{\partial t_1} + \frac{\partial w_{t_2}}{\partial t_2} \right) dn \tag{2.23}$$

This version of the body boundary condition is also used for the wake sources.

Equation 2.22 is the basis for including the effects of viscosity present in the total fluid velocity, $\mathbf{u}$, in the viscous potential velocity. This version of the 'transpiration velocity' concept has not been numerically implemented before now. Using this body boundary condition allows the total fluid velocity to define the viscous potential velocity. The viscous potential velocity can then be used as the external boundary conditions for the total fluid velocity on a small domain while maintaining the availability of the velocity in the infinite fluid domain. The numerical implementation of this body boundary condition is discussed in Section 3.3.1.

2.3.2 Velocity Decomposition of Inlet and Farfield Boundary Conditions

On large computational domains where the fluid velocity at the domain boundary is undisturbed by the presence of the body, setting the fluid velocity equal to the free-stream value on the inlet and farfield boundaries works well. On reduced domains, using the free-stream velocity as the inlet and farfield boundary conditions leads to an incorrect velocity field since it is essentially the wrong boundary value problem to be solving. For the reduced domains used with the velocity decomposition solver, the total velocity is set equal to the potential velocity. This modified boundary condition is based on the decomposition of the velocity on the inlet and farfield boundaries, and the assumption that the vortical velocity **w** is negligible since the boundaries are outside of the vortical region.

$$\mathbf{u}\big|_{\text{inlet \& farfield}} = \nabla\Phi\big|_{\text{inlet \& farfield}} \tag{2.24}$$

Eça and Hoekstra (2009) applied this form of the inlet and farfield boundary conditions using an inviscid potential and showed that it was an improvement over the free-stream value for moderate domain sizes. While using the potential velocity rather than the free-stream velocity value does offer an improvement on moderate domains, the desired accuracy can not be achieved using the inviscid potential velocity on significantly reduced domains.

The effects of viscosity must be included in the potential velocity to successfully use it as the inlet and farfield boundary conditions as stated in Equation 2.24. If the viscous effects are not included in the irrotational velocity, $\nabla\Phi$, the vortical velocity component, **w**, is not negligible outside of the vortical region and hence can not be neglected on the boundaries. Using the body boundary condition for the viscous potential provided in Equation 2.22 drives the vortical velocity to a negligible level outside of the vortical region so Equation 2.24 may be used, as demonstrated in the results chapters.

CHAPTER III

Numerical Implementation

The computational fluid dynamics environment Open Source Field Operation and Manipulation (OpenFOAM®) was chosen to implement the solver based on its vast open source C++ libraries that provide both tested RANS solvers and the ability to modify the existing solvers.

The RANS equation solution using a finite-volume method is discussed, followed by the numerical implementation of the potential flow solution using a two-dimensional constant-source-strength panel method and a three-dimensional constant-source-strength quadrilateral panel method. The velocity decomposition solver algorithm is then presented. The numerical implementation of the viscous potential velocity body boundary condition is described, followed by a description of the velocity decomposition solver parameters.

3.1 RANS Solution

Within OpenFOAM, the steady incompressible viscous flow solver simpleFoam was chosen as the base RANS solver since it represents an industry standard steady RANS solver. The simpleFoam solver is so named because it uses the Semi-Implicit Method for Pressure-Linked Equations (SIMPLE) algorithm as described by Patankar (1980). The simpleFoam solver will be referred to as the RANS solver throughout this work.

The RANS equations are discretized using the finite-volume method. The semi-discrete form for the total velocity vector is

$$a_P \mathbf{u}_P + \sum_N a_N \mathbf{u}_N = \mathbf{r}_P - \nabla p_P \tag{3.1}$$

where a is the matrix influence coefficient, $\mathbf{r}$ is the source term, and the subscripts P and N denote the point at the cell center and the neighboring cell centers respectively. If the term

$$H(\mathbf{u}) = \mathbf{r}_P - \sum_N a_N \mathbf{u}_N \tag{3.2}$$

is introduced, the momentum predictor step and pressure correction step of the SIMPLE algorithm for the RANS equations can be expressed as

$$\mathbf{u}_P = \frac{1}{a_P}[H(\mathbf{u}) - \nabla p^*_P] \tag{3.3}$$

$$\nabla \cdot \left[\frac{\nabla p_P}{a_P}\right] = \nabla \cdot \left[\frac{H(\mathbf{u})}{a_P}\right] \tag{3.4}$$

respectively, where p^* is the pressure from the previous iteration. The pressure correction step given by Equation 3.4 is derived by substituting the expression for $\mathbf{u}$ given in Equation 3.3 into the continuity equation given in Equation 2.1, and is used to make the total velocity field divergenceless. The convergence of the solution of this segregated solver is judged by monitoring the residuals, defined as a scaled L1 norm, for each variable.

The RANS solver uses second order Gaussian integration with linear interpolation of the cell center values to the face centers for the gradient and Laplacian terms. The Laplacian terms also use an explicit non-orthogonal correction for the surface normal gradient. The divergence terms are also discretized by Gaussian integration, but use a bounded first/ second order linear upwind interpolation scheme that uses Gaussian integration and linear interpolation to calculate the gradient. The divergence of the turbulent quantities, k and ω, are discretized by Gaussian integration using a first order upwind interpolation scheme. Overall, the equation discretization is formally of second order except for the turbulent quantities which are first order, or near extrema.

The ASME (Celik et al. 2008) procedure and a similar procedure utilizing a least squares fit presented by Eça and Hoekstra (2006) are used to estimate the uncertainty due to discretization. Details are provided in Appendix A. The drag coefficient for laminar flow over a NACA 0012 airfoil at a Reynolds number of 2000 is used to analyze the uncertainty. The ASME procedure provided an observed order of accuracy of $p = 1.3$ and a numerical uncertainty of $\mathrm{GCI}^{21}_{\mathrm{fine}} = 0.05\%$ for the medium-fine mesh. The least square root procedure presented by Eça and Hoekstra (2006) gave an observed order of accuracy of $p = 1.7$ and a numerical uncertainty of $U^{\mathrm{fine}}_{\mathrm{Cd}} = 0.002\%$ for the fine mesh. Both of the observed orders are close to, but lower than, the theoretical value of 2.0.

3.2 Potential Velocity Solution

As described in Section 2.2, the scalar potential used to define the potential velocity must satisfy Laplace's equation in the volume, V, surrounding the body. The body boundary condition applies on the body surface, S_B, and the radiation boundary condition applies on the outer boundary surface S_∞. A wake surface, S_W, is also included to allow a distribution of wake sources. The surfaces are labeled in Figure 2.1. The progression to the boundary integral equation for the potential is briefly outlined here, following the presentation in Katz and Plotkin (2001). The details are included in many sources, including Katz and Plotkin (2001) and Newman (1977).

Green's second identity relates a volume integral to a surface integral, defining the boundary integral equation that expresses the Laplace equation for the potential in the volume, V, as shown in Equation 3.5.

$$\int\limits_{S} (\Phi_1 \nabla \Phi_2 - \Phi_2 \nabla \Phi_1) \cdot \mathbf{n}\, dS = \int\limits_{V} (\Phi_1 \nabla^2 \Phi_2 - \Phi_2 \nabla^2 \Phi_1) dV \tag{3.5}$$

Here, $\mathbf{n}$ is the surface normal pointing out of the fluid domain and the surface S must completely surround the fluid domain. In this case, S is the sum of the body, wake, and outer surfaces.

$$S = S_B + S_W + S_\infty \tag{3.6}$$

Φ_1 and Φ_2 are defined as follows where r is the distance between a singularity element and a point, P:

$$\Phi_1 = \frac{1}{r} \qquad \text{in 3D} \tag{3.7}$$

$$\Phi_1 = \ln r \qquad \text{in 2D} \tag{3.8}$$

$$\Phi_2 = \Phi \tag{3.9}$$

The potential at the point, P, can then be expressed in three-dimensions as

$$\Phi(P) = -\frac{1}{4\pi} \int\limits_{S_B + S_W} \left[\sigma \left(\frac{1}{r} \right) - \mu \frac{\partial}{\partial n} \left(\frac{1}{r} \right) \right] dS + \Phi_\infty(P) \tag{3.10}$$

where σ is a source strength, μ is a doublet strength, and Φ_∞ is the free-stream potential. Since only flows without circulation are considered in this thesis, only the source elements are used and Equation 3.10 reduces to

$$\Phi(P) = -\frac{1}{4\pi} \int\limits_{S_B + S_W} \sigma \left(\frac{1}{r} \right) dS + \Phi_\infty(P) \tag{3.11}$$

In two dimensions, the potential at a point utilizing only source elements can be represented as

$$\Phi(P) = -\frac{1}{2\pi} \int\limits_{S_B+S_W} \sigma \ln r \, dS + \Phi_\infty(P) \tag{3.12}$$

A distribution of wake sources is also included in this work. For symmetric bodies, the influences of the body source elements cancel each other out along the centerline of the wake, which extends from the trailing edge of the body. If no flow is desired through the wake surface, as is generally the case, any source elements distributed along the wake would have a strength of zero. To achieve the viscous potential, it is desired to include the viscous effects in the wake, so wake sources are included subject to the same decomposed body boundary condition as the body.

The potential can be expressed as

$$\Phi = \phi + \mathbf{U}_\infty \cdot \mathbf{x} \tag{3.13}$$

where ϕ is the perturbation potential given by the integral terms in Equations 3.11 and 3.12, and $\mathbf{U}_\infty \cdot \mathbf{x}$ is the free-stream potential, Φ_∞.

To perform the calculation of the velocity field, the source strengths must be known. The source strengths are determined by satisfying the Neumann body boundary condition of non-penetration for the inviscid potential velocity or the decomposed body boundary condition for the viscous potential, as shown for the perturbation potential in Equations 3.14 and 3.15 respectively.

$$\left.\frac{\partial \phi}{\partial n}\right|_{\text{body}} = -(\mathbf{U}_\infty \cdot \mathbf{n})\big|_{\text{body}} \qquad \text{Inviscid Potential} \tag{3.14}$$

$$\left.\frac{\partial \phi}{\partial n}\right|_{\text{body \& wake}} = -(\mathbf{U}_\infty \cdot \mathbf{n})\big|_{\text{body \& wake}} - (\mathbf{w} \cdot \mathbf{n})\big|_{\text{body \& wake}} \qquad \text{Viscous Potential} \tag{3.15}$$

Equation 3.16 is constructed by satisfying the body boundary condition at each body panel center and wake source location, where the latter term on the right side is dropped in the inviscid case.

$$[\mathbf{A}][\sigma_{\text{body \& wake}}] = -[(\mathbf{U}_\infty \cdot \mathbf{n})\big|_{\text{body \& wake}}] - [(\mathbf{w} \cdot \mathbf{n})\big|_{\text{body \& wake}}] \qquad (3.16)$$

The matrix of influence coefficients, $\mathbf{A}$, is generated by calculating the normal velocity at collocation point i due to source j with a source strength of one, where $i = 1 : N$, $j = 1 : N$, and N is the number of sources. The terms on the right side represent vectors of the body boundary condition at each collocation point, which consist of the body panel centers and wake source locations. The inverse of the influence coefficient matrix, $\mathbf{A}$, is calculated using LU (Lower-Upper) decomposition. The vector of source strengths for each body panel and wake source, $[\sigma_{\text{body \& wake}}]$, is solved for by multiplying both sides of the equation by the inverted influence coefficient matrix, $\mathbf{A}^{-1}$. In the two-dimensional cases, constant strength source panels are used for the wake sources as well as the body sources. While point sources could be used in the wake, using panel sources offers some benefits in specifying the wake source strengths, as described in the following section.

The second boundary condition imposed on the potential velocity is the radiation condition, which ensures that the undisturbed velocity, $\mathbf{U}_\infty$, is recovered far from the body; the constant-strength source solution satisfies this naturally.

The perturbation potential is calculated using constant-strength source elements as described in the following sections for two- and three- dimensional cases. The velocity contributions are defined in local panel coordinate systems, denoted by the subscript p. In the two-dimensional case, x_p is aligned with the panel tangent, $\mathbf{t}_1$, and y_p is aligned with the outward panel normal, $\mathbf{n}$, as shown in Figure 3.1. In three dimensions, x_p and y_p are aligned with two orthogonal panel tangents, $\mathbf{t}_1$ and $\mathbf{t}_2$, and z_p is aligned with the outward panel normal, $\mathbf{n}$. Note that the panel normals are defined pointing out of the body into the fluid for the body boundary conditions and panel coordinate systems. The normal direction used across the body boundary condition is independent from the normal used in Green's Theorem since the normal is present in each term of the boundary condition.

3.2.1 Two-Dimensional Potential Velocity

The two-dimensional potential velocity field is determined using a constant-strength source panel method as described by Katz and Plotkin (2001). The velocity contribution at a collocation point due to the perturbation potential of a single panel in the $x-$ and $y-$ directions of the local panel coordinate system are given by

$$\frac{\partial \phi}{\partial x_p} = \frac{\sigma}{4\pi} \ln \frac{r_1^2}{r_2^2} \tag{3.17}$$

$$\frac{\partial \phi}{\partial y_p} = \frac{\sigma}{2\pi} (\theta_2 - \theta_1) \tag{3.18}$$

respectively, where σ is the source strength of the panel, the subscript p denotes panel coordinates, and r_1, r_2, θ_1, and θ_2 correspond to the distances and angles shown in Figure 3.1.

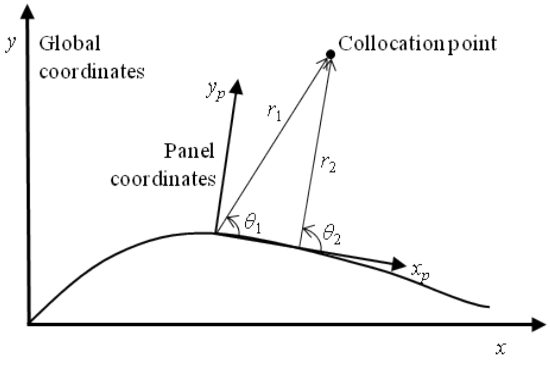

Figure 3.1: Coordinate system and variable definitions for the two-dimensional perturbation potential (based on Katz and Plotkin 2001).

It follows from Equations 3.17 and 3.18 that the perturbation velocity for a collocation point centered just above a panel will be given by

$$\frac{\partial \phi}{\partial x_p}(x_p, 0) = 0 \tag{3.19}$$

$$\frac{\partial \phi}{\partial y_p}(x_p, 0) = \frac{\sigma}{2} \tag{3.20}$$

Due to the symmetry of the bodies considered in this work and the alignment of the wake sources on the center-line, each of the wake panels is only influenced by itself, so Equation 3.20 can be re-arranged to solve for each of the wake source strengths, noting that $\partial\phi/\partial y_p = \partial\phi/\partial n$.

$$\sigma_{\text{wake}} = 2\frac{\partial \phi}{\partial y_p}(x_p, 0) \tag{3.21}$$

3.2.2 Three-Dimensional Potential Velocity

The three-dimensional potential velocity field is determined using a constant-strength source distribution over planar quadrilateral panels as developed by Hess and Smith (1967) and described by Katz and Plotkin (2001). The integral of the three-dimensional Green function over the quadrilateral source gives the potential at a point $P(x, y, z)$. The velocity contribution at a collocation point due to the perturbation potential of a single panel in the $x-$, $y-$, and $z-$ directions of the local panel coordinate system, are given by Equations 3.22, 3.23, and 3.24 respectively. The collocation point P is located at (x, y, z). The panel corners are assigned subscripts 1 through 4, and the $z-$ coordinate of the panel corners is zero since the panel is planar and the panel coordinate system origin is located at the centroid of the panel.

$$
\begin{aligned}
\frac{\partial\phi}{\partial x_p} =& \frac{\sigma}{4\pi}\left[\frac{y_2-y_1}{d_{12}}\ln\frac{r_1+r_2-d_{12}}{r_1+r_2+d_{12}}+\frac{y_3-y_2}{d_{23}}\ln\frac{r_2+r_3-d_{23}}{r_2+r_3+d_{23}}\right.\\
&\left.+\frac{y_4-y_3}{d_{34}}\ln\frac{r_3+r_4-d_{34}}{r_3+r_4+d_{34}}+\frac{y_1-y_4}{d_{41}}\ln\frac{r_4+r_1-d_{41}}{r_4+r_1+d_{41}}\right] \qquad (3.22)
\end{aligned}
$$

$$
\begin{aligned}
\frac{\partial\phi}{\partial y_p} =& \frac{\sigma}{4\pi}\left[\frac{x_1-x_2}{d_{12}}\ln\frac{r_1+r_2-d_{12}}{r_1+r_2+d_{12}}+\frac{x_2-x_3}{d_{23}}\ln\frac{r_2+r_3-d_{23}}{r_2+r_3+d_{23}}\right.\\
&\left.+\frac{x_3-x_4}{d_{34}}\ln\frac{r_3+r_4-d_{34}}{r_3+r_4+d_{34}}+\frac{x_4-x_1}{d_{41}}\ln\frac{r_4+r_1-d_{41}}{r_4+r_1+d_{41}}\right] \qquad (3.23)
\end{aligned}
$$

$$
\begin{aligned}
\frac{\partial\phi}{\partial z_p} =& \frac{\sigma}{4\pi}\left[\tan^{-1}\left(\frac{m_{12}e_1-h_1}{zr_1}\right)-\tan^{-1}\left(\frac{m_{12}e_2-h_2}{zr_2}\right)\right.\\
&+\tan^{-1}\left(\frac{m_{23}e_2-h_2}{zr_2}\right)-\tan^{-1}\left(\frac{m_{23}e_3-h_3}{zr_3}\right)\\
&+\tan^{-1}\left(\frac{m_{34}e_3-h_3}{zr_3}\right)-\tan^{-1}\left(\frac{m_{34}e_4-h_4}{zr_4}\right)\\
&\left.+\tan^{-1}\left(\frac{m_{41}e_4-h_4}{zr_4}\right)-\tan^{-1}\left(\frac{m_{41}e_1-h_1}{zr_1}\right)\right] \qquad (3.24)
\end{aligned}
$$

The following equations define the included terms.

$$d_{12} = \sqrt{(x_2 - x_1)^2 + (y_2 - y_1)^2} \tag{3.25}$$

$$d_{23} = \sqrt{(x_3 - x_2)^2 + (y_3 - y_2)^2} \tag{3.26}$$

$$d_{34} = \sqrt{(x_4 - x_3)^2 + (y_4 - y_3)^2} \tag{3.27}$$

$$d_{41} = \sqrt{(x_1 - x_4)^2 + (y_1 - y_4)^2} \tag{3.28}$$

$$m_{12} = \frac{y_2 - y_1}{x_2 - x_1} \tag{3.29}$$

$$m_{23} = \frac{y_3 - y_2}{x_3 - x_2} \tag{3.30}$$

$$m_{34} = \frac{y_4 - y_3}{x_4 - x_3} \tag{3.31}$$

$$m_{41} = \frac{y_1 - y_4}{x_1 - x_4} \tag{3.32}$$

$$r_k = \sqrt{(x - x_k)^2 + (y - y_k)^2 + z^2}, \qquad k = 1,\ 2,\ 3,\ 4 \tag{3.33}$$

$$e_k = (x - x_k)^2 + z^2, \qquad k = 1,\ 2,\ 3,\ 4 \tag{3.34}$$

$$h_k = (x - x_k)(y - y_k), \qquad k = 1,\ 2,\ 3,\ 4 \tag{3.35}$$

It should be noted that the inverse tangent in Equation 3.24 is evaluated in the principle-value range of $-\pi/2$ to $\pi/2$; Hess and Smith also present an alternate form of Equation 3.24 where the inverse tangent is defined in the principle-value range of $-\pi$ to π (Hess and Smith 1967). When the collocation point approaches $z = 0$ in panel coordinates,

$$\frac{\partial \phi}{\partial z_p}(z = 0\pm) = \frac{\pm\sigma}{2} \tag{3.36}$$

if the point is inside the quadrilateral, and

$$\frac{\partial \phi}{\partial z_p}(z = 0\pm) = 0 \tag{3.37}$$

if the point is outside the quadrilateral.

When the collocation point is sufficiently far from the panel center, the quadrilateral source can be estimated as a point source to reduce the computational expense. Based on the conservative recommendations in Katz and Plotkin (2001), the collocation point must be five times the average panel diameter away from the panel to use the point source estimation. In this case, Equations 3.38 through 3.40 may be used in place of Equations 3.22 through 3.24.

$$\frac{\partial \phi}{\partial x_p} = \frac{\sigma A(x - x_0)}{4\pi[(x - x_0)^2 + (y - y_0)^2 + z^2]^{3/2}} \tag{3.38}$$

$$\frac{\partial \phi}{\partial y_p} = \frac{\sigma A(y - y_0)}{4\pi[(x - x_0)^2 + (y - y_0)^2 + z^2]^{3/2}} \tag{3.39}$$

$$\frac{\partial \phi}{\partial z_p} = \frac{\sigma A(z - z_0)}{4\pi[(x - x_0)^2 + (y - y_0)^2 + z^2]^{3/2}} \tag{3.40}$$

where A is the panel area. The point source approximation is not currently implemented in the three-dimensional code, and hence offers a source of further computational time reduction.

3.3 Velocity Decomposition Solver Algorithm

The algorithm used by the velocity decomposition solver is shown in the form of a flow chart in Figure 3.2. The steps on the flow chart are described below. The details of the numerical implementation of the viscous potential velocity body boundary condition are discussed, followed by a description of the velocity decomposition solver parameters.

The steps of the velocity decomposition solver algorithm are:

1. Initiate solver by providing the mesh, boundary conditions, and initial conditions. The solver parameters must also be specified.
2. Solve for the inviscid potential velocity, $\nabla\Phi$.
3. Set $\mathbf{u} = \nabla\Phi$ to initialize the flow field (optional).
4. Set $\mathbf{u}\big|_{\text{inlet \& farfield}} = \nabla\Phi\big|_{\text{inlet \& farfield}}$.
5. Solve for the total fluid velocity, pressure, and turbulence quantities using the RANS solver on a small domain surrounding the vortical regions around the body and in the wake.
6. When the maximum velocity residual, $\max[res(\mathbf{u})]$, drops below the user-specified update residual, res_{update}, update the inlet and farfield boundary conditions using the following procedure where initially $i = 0$ and i is the iteration number.
    (a) Calculate the integration limit, δ, based on the vorticity field of the total fluid, $\mathbf{u}$.
    (b) Calculate the potential velocity at δ, $\nabla\Phi^i(\delta)$, using the previously calculated source strengths. Either the inviscid potential source strengths or

the final viscous potential sources strengths from the previous update can be used. The inviscid source strengths are used in the current implementation.

   (c) Iterate the following three steps according to the number of iterations specified by the user to find the source strengths for the viscous potential velocity.

      i. Set $\mathbf{w}^i(\delta) = \mathbf{u}(\delta) - \nabla\Phi^i(\delta)$ and use $\mathbf{w}^i(\delta)$ to calculate the new body boundary condition for the viscous potential velocity $\frac{\partial\Phi}{\partial n}\Big|^{i+1}_{\text{body \& wake}} = f(\mathbf{w}^i)$. The details of this step are discussed in the following section.

      ii. Use the body boundary condition $\frac{\partial\Phi}{\partial n}\Big|^{i+1}_{\text{body \& wake}}$ to calculate new source strengths, σ^{i+1}.

      iii. Use the new source strengths, σ^{i+1}, to calculate $\nabla\Phi^{i+1}(\delta)$.

   (d) Use the final source strengths, $\sigma^{i=\#\text{ of iter.}}$, to calculate the viscous potential on the inlet and farfield boundaries, $\nabla\Phi\big|_{\text{inlet \& farfield}}$.

7. Set $\mathbf{u}\big|_{\text{inlet \& farfield}} = \nabla\Phi\big|_{\text{inlet \& farfield}}$.

8. Repeat steps 5 through 7 according to the number of updates specified.

9. Solve for the total fluid velocity, pressure, and turbulence quantities using the RANS solver.

10. When the specified final residuals are reached for all variables, terminate the solver. The solution has been reached.

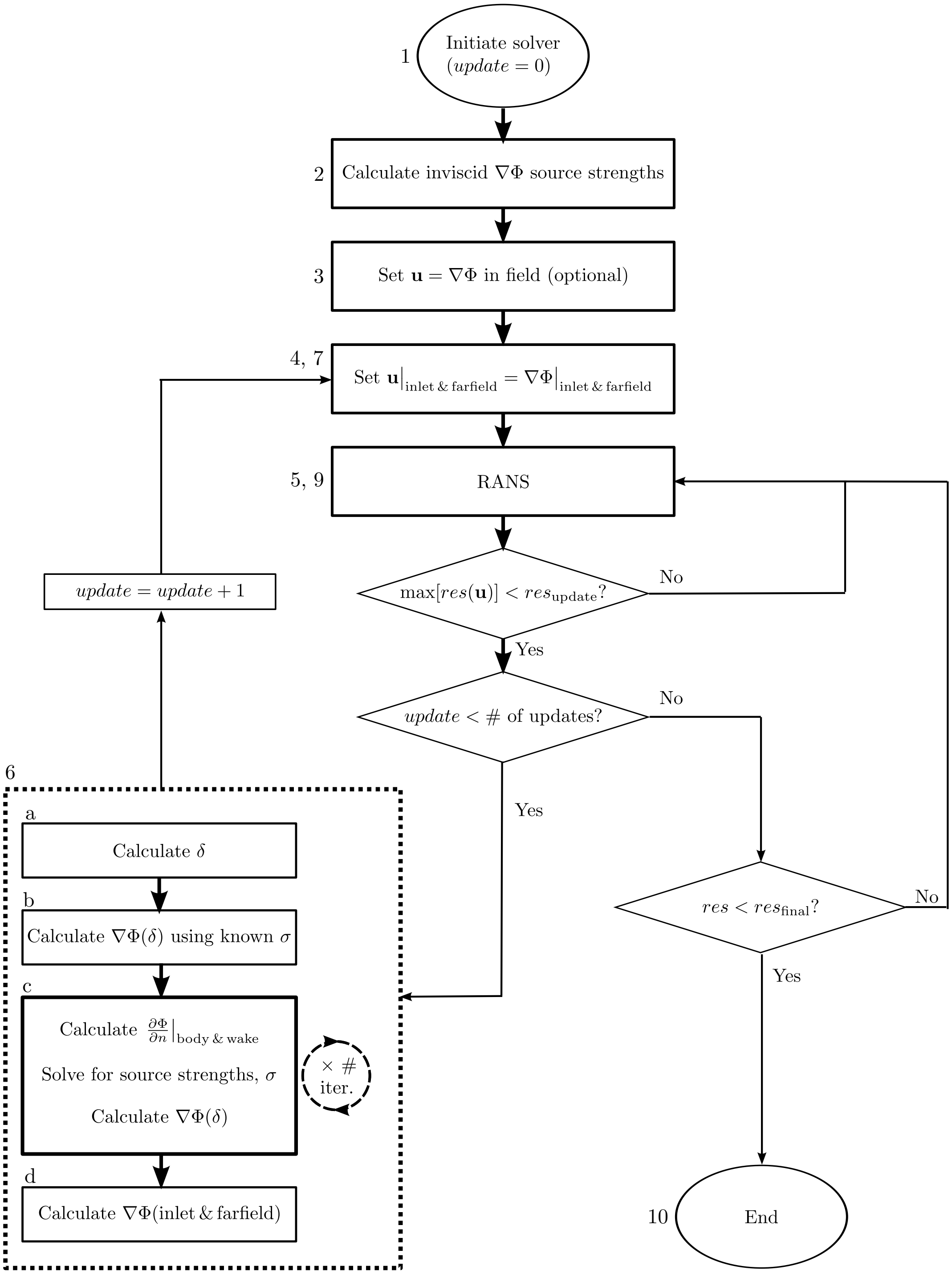

Figure 3.2: Velocity decomposition solver flow chart with numbers and letters corresponding to the description in the text. Step 8 is to repeat steps 5 through 7.

3.3.1 Viscous Potential Velocity Body Boundary Condition

Section 2.3.1 describes the derivation of the viscous potential body boundary condition given by Equation 2.22 and re-stated here.

$$\left.\frac{\partial \Phi}{\partial n}\right|_{\text{body \& wake}} = -\int_0^\delta \left(\frac{\partial w_{t_1}}{\partial t_1} + \frac{\partial w_{t_2}}{\partial t_2} \right) dn \tag{3.41}$$

In the iterative framework of the implementation described in Step 6c of the algorithm in the previous section, the body boundary condition can be expressed as

$$\left.\frac{\partial \Phi}{\partial n}\right|_{\text{body \& wake}}^{i+1} = f(\mathbf{w}^i) \tag{3.42}$$

where, for convenience, we defined

$$f(\mathbf{w}^i) = -\int_0^\delta \left(\frac{\partial w^i_{t_1}}{\partial t_1} + \frac{\partial w^i_{t_2}}{\partial t_2} \right) dn \tag{3.43}$$

We seek the value of the integral term in Equation 3.43. While numerically integrating the gradient of the vortical velocity does work, revisiting the original expression for the integral of the divergence along the normal offers a more accurate and less computationally expensive alternative. The integral of the divergence of the vortical component of the velocity, **w**, along the local normal is shown in Equation 3.44 and simplified to Equation 3.45, where i indicates the iteration level.

$$\int_0^\delta \left(\frac{\partial w^i_n}{\partial n} + \frac{\partial w^i_{t_1}}{\partial t_1} + \frac{\partial w^i_{t_2}}{\partial t_2} \right) dn = 0 \tag{3.44}$$

$$\int_0^\delta \left(\frac{\partial w^i_{t_1}}{\partial t_1} + \frac{\partial w^i_{t_2}}{\partial t_2} \right) dn + w^i_n(\delta) - w^i_n(0) = 0 \tag{3.45}$$

Re-arranging the terms in Equation 3.45 results in Equation 3.46.

$$\int_{0}^{\delta} \left(\frac{\partial w_{t_1}^i}{\partial t_1} + \frac{\partial w_{t_2}^i}{\partial t_2} \right) dn = w_n^i(0) - w_n^i(\delta) \tag{3.46}$$

Substituting Equation 3.46 into Equation 3.43 leads to the following expression:

$$f(\mathbf{w}^i) = -w_n^i(0) + w_n^i(\delta) \tag{3.47}$$

The viscous potential body boundary condition can therefore be stated in terms of the values of the normal vortical velocity component on the body and at δ from the previous iteration:

$$\left.\frac{\partial \Phi}{\partial n}\right|_{\text{body \& wake}}^{i+1} = f(\mathbf{w}^i) = -w_n^i(0) + w_n^i(\delta) \tag{3.48}$$

Using Equation 3.48 to calculate the desired viscous potential velocity body boundary condition rather than numerically calculating the integral form of the equation significantly reduces the computational expense. The potential velocity only needs to be calculated at δ for each panel rather than in the whole field. The computational expense and errors introduced by a numerical integration scheme are eliminated.

3.3.2 Velocity Decomposition Solver Parameters

The value of δ used to determine the body boundary condition for the viscous potential velocity is defined as the normal distance from each panel where the vorticity has dropped to a negligible value. The vorticity is defined as $\boldsymbol{\omega} = \nabla \times \mathbf{u}$. Technically, δ can be any distance past the vortical region. However, it has been observed that using the minimal value of δ outside the vortical region provides a viscous potential velocity that matches the fluid velocity better in fewer iterations. δ essentially defines the thickness of the vortical region. The value of δ for each body and wake panel is determined for a given fluid velocity field by calculating the vorticity in the field, then sampling the value of the vorticity in each cell the panel normal crosses out to some distance, δ_{max}. The maximum vorticity, ω_{max}, from the sampled set is then found for each panel. The negligible level of vorticity is defined as $\omega_{\mathrm{limit}} = \alpha_{\mathrm{vort}}\omega_{\mathrm{max}}$, where α_{vort} is a fraction input by the user. The location of δ can then be determined by finding the cell closest to the body along the normal sample line where the average of the vorticity in that cell and the cells before and after that cell is less than the vorticity limit, ω_{limit}. The three-point averaging procedure prevents δ from being located at a dip in the vorticity rather than where the vorticity is truly trending towards zero. If the negligible vorticity value is not found on the sample line, δ is set to zero to prevent calculating the boundary condition based on a velocity that is within the vortical region. In this case, the non-penetration condition is the boundary condition on that panel. It may be possible to assign the viscous potential velocity body boundary condition on the panels where the desired vorticity drop is not found based on the neighboring panels, rather than using the non-penetration condition.

The parameters involved in determining δ are the distance along the normal to sample the vorticity, δ_{max}, for each panel on the body and in the wake, and the fraction, α_{vort}, of the maximum sampled vorticity used to define the negligible vorticity limit. The sampling distance, δ_{max}, is assigned separate values for panels on the body and panels in the wake.

The user must also define the location of the wake panels by specifying the end of the body, the initial wake panel length, w_{s}, the panel growth rate, w_{g}, and the number of wake panels, n_{wp}. The wake panels are then distributed according to a geometric growth rate. The panel centers are defined by

$$x_{wp,i} = x_{wp,i-1} + \frac{1}{2}w_{\mathrm{s}}(1 + w_{\mathrm{g}})^{i-1} + \frac{1}{2}w_{\mathrm{s}}(1 + w_{\mathrm{g}})^{i} \tag{3.49}$$

where $x_{wp,i}$ indicates the $x-$ coordinate of the center of the ith wake panel. The first wake panel center is located half of the initial wake panel length, w_s, from the trailing edge of the body. The $y-$ and $z-$ coordinates of the wake panel centers are assigned as constants equal to their value at the center of the trailing edge of the body. The current implementation of the wake panel distribution is limited to symmetric bodies and will need to be modified to handle more complex wake structures.

The number of iterations used to modify the body boundary condition for the viscous potential velocity for a given velocity field, the number of times to update the inlet and farfield boundary conditions for the fluid velocity based on the viscous potential, and the residual at which to perform those updates must also be specified by the user. The parameters are further described and demonstrated in the results chapters.

CHAPTER IV

Laminar Two-Dimensional Results

Results for steady laminar flow over a flat plate, a circular cylinder, and a NACA 0012 airfoil are presented. The RANS solver is used to generate solutions with which to compare the velocity decomposition solver results. The parameters used in the velocity decomposition solver are studied in the flat plate and the circular cylinder cases. Those cases are then used to guide the selection of the parameters for the NACA 0012 airfoil. The velocity decomposition solver is shown to obtain results that compare very well with the RANS solutions in less computation time.

For each case, the problem is stated and the RANS solution is developed. The velocity decomposition parameters are then discussed. Finally, the velocity decomposition solver solution is compared to the RANS solver solution.

4.1 Laminar Flat Plate

Laminar flow over a flat plate at a Reynolds number of 2000 based on the plate length is studied with a RANS solver and the velocity decomposition solver. While the geometry of this case is quite simple, it offers insight into the ability of the viscous potential velocity to account for the boundary layer effects. The computational domain and coarse $10L$ mesh used for the RANS solver are shown in Figure 4.1, where $L = 1.0$ m is the plate length. As described in the next section, the coarse $10L$

mesh is the coarsest of a set of systematically refined meshes that extend ten plate lengths from the plate in the inlet and farfield directions. The reduced domain for the velocity decomposition solver is outlined to show the scale of the reduction. The plate is located on the $x-$axis from $x = 0$ to $x = 1$.

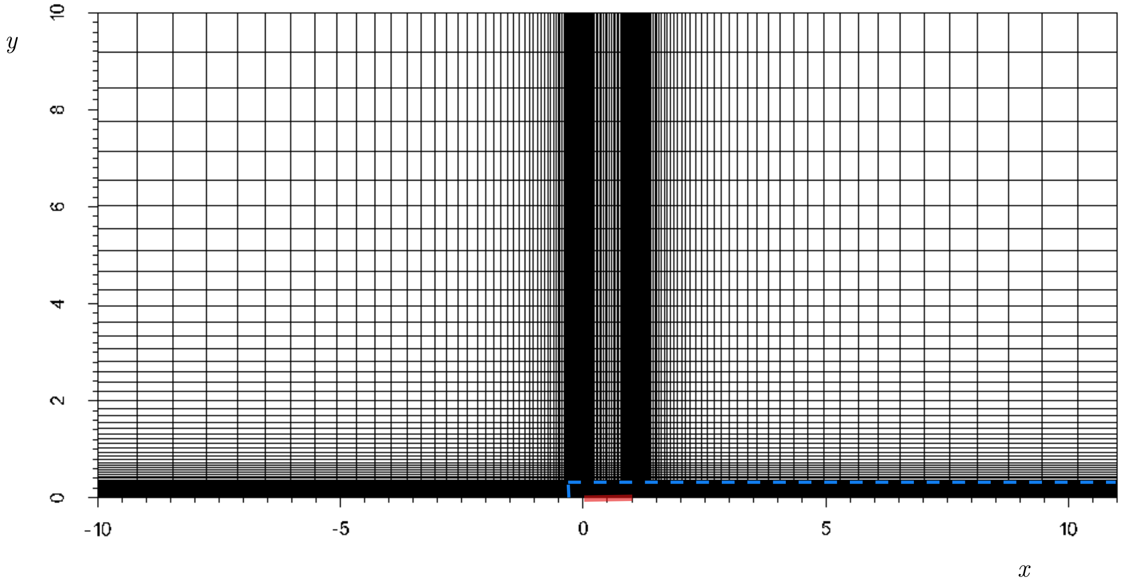

Figure 4.1: Laminar flat plate coarse $10L$ mesh with the plate located on the $x-$axis from $x = 0$ to $x = 1$ and the reduced $0.3L$ domain outlined by the blue dashed line.

For the RANS solver, the velocity is set equal to the free-stream velocity, $U_\infty = 0.002$ m/s at the inlet and farfield boundaries, and zero at the wall. The outlet pressure is set to zero to serve as the reference pressure. The velocity at the outlet, and the pressure at the inlet, farfield, wall, and center plane are calculated to achieve zero normal gradient. A slip boundary condition, which sets the normal component to zero and enforces zero normal gradient on the tangential component, is used for the velocity on the center plane before and after the plate. The pressure field is initially set to zero, and the velocity is initially set equal to the free-stream velocity.

The only modification to the boundary conditions for the velocity decomposition solver is that the fluid velocity on the inlet and farfield boundaries is set equal to the potential velocity.

4.1.1 RANS Domain Dependence Study

To ensure the accuracy of the RANS solution used to validate the velocity decomposition solver, a study of the computational domain resolution and extent was performed. Coarse, medium, and fine structured meshes extending ten plate lengths, L, in the inlet, farfield, and outlet directions from the plate were systematically created by doubling the resolution. The meshes are concentrated around the leading and trailing edges of the plate, and in the boundary layer. Table 4.1 provides the mesh resolution given as the number of cells normal to the plate by the number along the length of the domain, number of panels (faces) along the plate, total number of cells, and mesh refinement factor $r_j = h_j/h_{\text{fine}}$ where j is the mesh being evaluated. The representative mesh size h is defined for two-dimensional cases by

$$h = \left[\frac{1}{N}\sum_{i=1}^{N}\Delta A_i\right]^{1/2} \tag{4.1}$$

where N is the number of cells in the mesh and ΔA_i is the area of the ith cell. In three-dimensional cases, ΔA_i is replaced by ΔV_i, which is the volume of the ith cell and the power of 1/2 is replaced by 1/3. The domain extents of the coarse mesh were doubled from ten to twenty times the plate length by extending the original coarse mesh to ensure the overlapping portion is identical. The coarse $20L$ mesh has a larger mesh refinement factor due to the addition of larger cells outside of the original $10L$ domain.

Velocity profiles at $x/L = 0.05, 0.25, 0.5, 0.95$, and 1.5 from the three mesh resolutions on the $10L$ domain, and the coarse $20L$ domain are shown to match quite well in the top of Figure 4.2. The bottom of Figure 4.2 shows the error in the drag coefficient

Table 4.1: Laminar flat plate mesh characteristics.

Mesh	Resolution	Plate panels	# of Cells	$r_j = h_j/h_{\text{fine}}$
Fine 10L	300 x 800	200	240,000	1.0
Medium 10L	150 x 400	100	60,000	2.0
Coarse 10L	75 x 200	50	15,000	4.0
Coarse 20L	85 x 220	50	18,700	7.1

and the root mean square (RMS) of the error in the x-component of the velocity, u, at ten points located at $y/L = 0.05$ and 0.2 and $x/L = 0.05, 0.25, 0.5, 0.95$, and 1.5 with respect to the fine mesh solution as a function of the mesh refinement factor. Note that the highest mesh refinement factor corresponds to the larger domain. The drag coefficient is defined in Equation 4.2 and the error in the drag coefficient is defined in Equation 4.3.

$$\text{Cd} = \frac{F}{0.5\rho \mathbf{U}_\infty{}^2 LW} \tag{4.2}$$

$$\text{Cd}\,\%\,\text{error} = 100\frac{\text{Cd}_i - \text{Cd}_j}{\text{Cd}_i} \tag{4.3}$$

where F is the drag force, L is the body length, and W is the width of the body or computational domain. The indices i and j represent the value being compared to and the value being compared respectively. The RMS of the error in the x-component of the velocity, u, is defined in Equation 4.4.

$$\text{RMS}\,\%\,\text{error} = 100\frac{\sqrt{\sum_{k=1}^{n}(u_{i,k} - u_{j,k})^2/n}}{U_\infty} \tag{4.4}$$

where n is the number of points considered.

Table 4.2 provides the error values described above, as well as the errors with respect to the next finer or smaller mesh, and the drag coefficient values. All of the errors are less than 0.5%. The error in the drag coefficient between the coarse 10L mesh and the medium 10L mesh is 0.21%, and the error between the coarse 20L mesh and the coarse 10L mesh is 0.096%, so the coarse 10L mesh appears to sufficiently capture the solution and will be the standard against which to compare the velocity

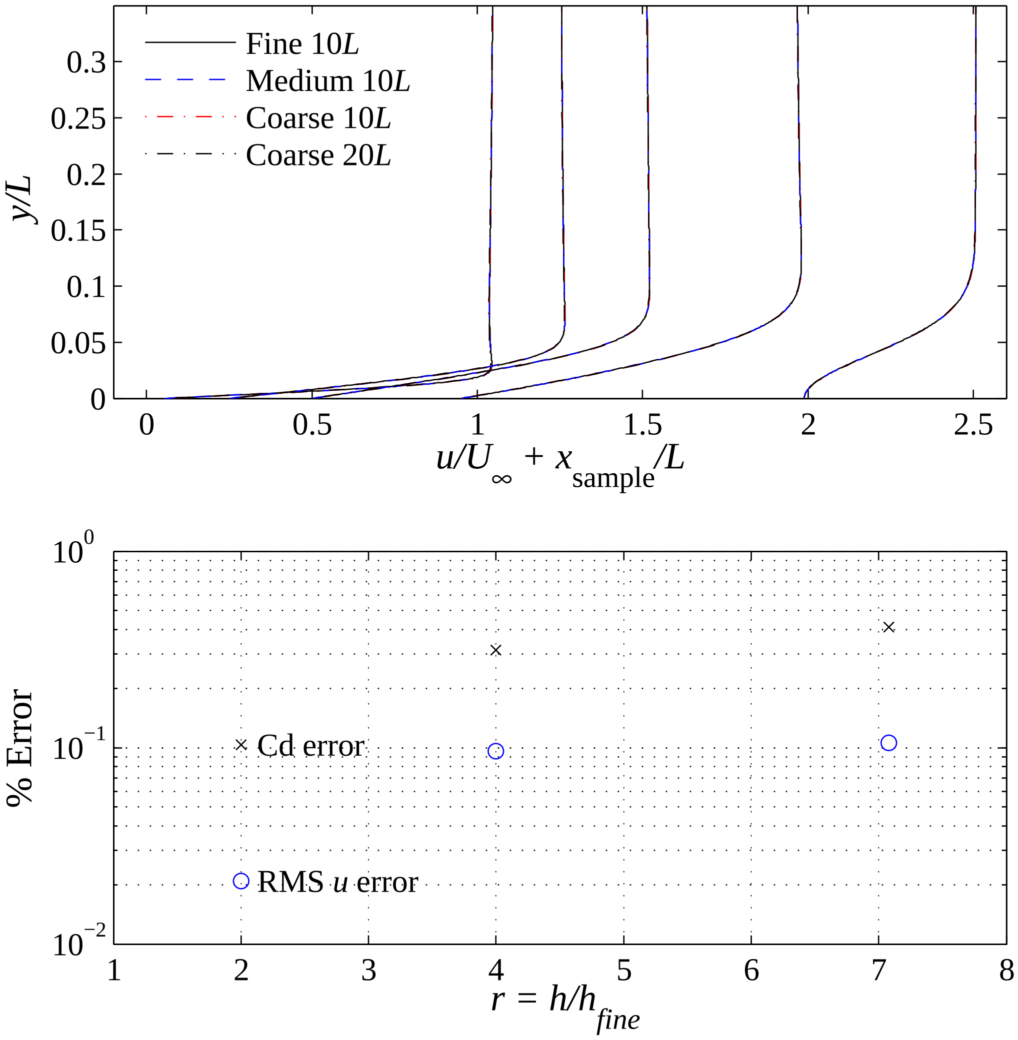

Figure 4.2: RANS solver results for laminar flow over a flat plate at Re = 2000. Top: Velocity profiles at $x/L = 0.05, 0.25, 0.5, 0.95$, and 1.5. Bottom: Drag coefficient error and RMS velocity error with respect to the finest resolution as a function of mesh refinement factor.

decomposition solver.

4.1.2 Velocity Decomposition Parameters

To observe the effects of the velocity decomposition parameters, the velocity decomposition solver was used to calculate the viscous potential velocity given the con-

Table 4.2: Laminar flat plate at Re = 2000 drag coefficients and error in RANS solver due to domain resolution and extent.

Mesh	Cd	Cd error w/fine	Cd relative error	RMS velocity error w/ fine	RMS velocity relative error
Fine $10L$	0.03315				
Medium $10L$	0.03312	0.10%	0.10%	0.024%	0.024%
Coarse $10L$	0.03305	0.31%	0.21%	0.11%	0.086%
Coarse $20L$	0.03301	0.41%	0.096%	0.11%	0.071%

verged coarse $10L$ RANS fluid velocity field described in the previous section. The parameters influencing the viscous potential include the limits on how far from the body and wake panels to scan the vorticity field, $\delta_{\text{max, body}}$ and $\delta_{\text{max, wake}}$, the fraction of the maximum vorticity, α_{vort}, on a given panel normal that is used to define the negligible vorticity limit, the distribution of wake panels, and the number of iterations used to calculate the body boundary condition for the viscous potential. The effects of these parameters are presented in terms of the average error between the magnitude of the viscous potential velocity and the fluid velocity at δ above each body panel, as shown in Equation (4.5).

$$\text{Err}(\delta)\% = \frac{100}{n_{\text{bp}}} \sum_{i=1}^{n_{\text{bp}}} \frac{|\mathbf{u}_i(\delta_i) - \nabla\Phi_i(\delta_i)|}{|\mathbf{u}_\mathbf{i}(\delta_i)|} \tag{4.5}$$

where n_{bp} is the number of panels on the body.

The value of δ_{max} for the body and the wake should be outside of the expected boundary layer and inside of the flow domain. For the flat plate at a Reynolds number of 2000, δ_{max} was set to $0.3L$ on the body and $0.5L$ in the wake. These values allowed the algorithm to find the desired vorticity drop for all panels in a reasonable amount of computation time. Using a higher δ_{max} than needed will add computation time, and if the sampled line ends close to the outer boundaries on a reduced computational domain, the vorticity introduced by the boundary may make the calculation of δ inaccurate.

As shown in the first section of Table 4.3, fractions ranging from 0.1 to 0.0001 were tested as the fraction, α_{vort}, of the maximum vorticity on a given panel normal that is used to define a negligible vorticity. The average error at δ shows that $\alpha_{\text{vort}} = 0.01$ provides the lowest error between the viscous potential velocity and the converged fluid velocity. Using a larger fraction causes a significant increase in the error between the viscous potential velocity and the fluid velocity since it causes δ to be located within the vortical region. Lower fractions are acceptable, but they result in larger δ values which essentially relax the inclusion of the viscous effects.

The second section of Table 4.3 shows the average error at δ for a range of wake panel distributions. The lowest error is achieved with an initial spacing of $w_{\text{s}} = 0.2L$, and a growth rate of $w_{\text{g}} = 0.25$. The number of panels, n_{wp}, is determined according to the length of the computational domain in the downstream direction. For the distribution mentioned above, eleven panels are used. The error is increased by both coarsening and refining the wake distribution from these values, though refining the distribution only slightly increases the error. The number of panels could be reduced as the first few have the most impact, but allowing them to extend to the downstream boundary adds very little computation time with this distribution.

The final section in Table 4.3 shows the influence of the number of iterations on the average error at δ for a given fluid velocity field. The best vorticity fraction and wake distribution, as described above, are used, and the average errors between the viscous potential velocity and the fluid velocity are provided at iterations $0-5$, 10, 15, 20, and 25. Note that iteration zero uses the inviscid potential velocity. The viscous potential velocity approximates the fluid velocity at δ quite well, and converges toward a solution with an average error of approximately 0.07% by 25 iterations for the flat plate. The average error at δ decreases from 5% with the inviscid potential to under 1% by the second iteration, so two iterations appear to be sufficient and will be used in the solver for the flat plate case. The fewest number of iterations that achieve the desired level of accuracy should be used. More iterations can be used to further improve the solution, but will slightly increase the computational cost.

Table 4.3: Influence of the vorticity limit fraction, α_{vort}, wake distribution, and number of iterations on the average error between the viscous potential velocity and the fluid velocity at δ for all body panels for flow over a flat plate at Re = 2000.

α_{vort}	n_{wp}	w_{s}/L	w_{g}	# of Iter.	Err(δ)
0.1	11	0.20	0.25	4	1.10%
0.01	11	0.20	0.25	4	0.31%
0.001	11	0.20	0.25	4	0.38%
0.0001	11	0.20	0.25	4	0.45%
0.01	0	–	–	4	0.85%
0.01	8	0.40	0.25	4	0.32%
0.01	11	0.20	0.25	4	0.31%
0.01	14	0.10	0.25	4	0.32%
0.01	29	0.01	0.2	4	0.32%
0.01	11	0.20	0.25	0	5.01%
0.01	11	0.20	0.25	1	1.48%
0.01	11	0.20	0.25	2	0.69%
0.01	11	0.20	0.25	3	0.44%
0.01	11	0.20	0.25	4	0.31%
0.01	11	0.20	0.25	5	0.24%
0.01	11	0.20	0.25	10	0.12%
0.01	11	0.20	0.25	15	0.09%
0.01	11	0.20	0.25	20	0.08%
0.01	11	0.20	0.25	25	0.07%

The final two parameters are the residual, res_{update}, at which to update the velocity boundary conditions, and the number of times to update the velocity boundary conditions. To determine recommended values for these parameters, the velocity decomposition solver was applied to a reduced domain, and the result compared to the RANS solution on the full domain. The coarse $10L$ flat plate mesh described above was trimmed to extend $0.3L$ in the inlet and farfield directions. The outlet extent was not modified. Further details on the reduced mesh case are provided in the following section.

The drag coefficient error and the RMS velocity error are used to assess the performance of the velocity decomposition solver on a reduced domain with different parameter values. The coarse $10L$ domain RANS solution is used as the benchmark. The RMS velocity error is based on the x-component of the velocity, u, at ten points located at $y/L = 0.05$ and 0.2 and $x/L = 0.05, 0.25, 0.5, 0.95$, and 1.5.

The first section of Table 4.4 shows the influence of the residual, res_{update}, at which the boundary condition update occurs. Reducing the residual limit from 1×10^{-3} to 1×10^{-4} reduces the error seen in both the drag coefficient and the RMS velocity error. Decreasing the residual further to 1×10^{-5} does not offer any further advantage. Using lower residuals tends to increase the overall computation time since the solver is spending longer finding the solution to the boundary value problem with inlet and farfield boundary conditions that are not as accurate as their final values. The residual at which to update the inlet and farfield boundaries will therefore be $res_{\text{update}} = 1 \times 10^{-4}$.

The influence of the number of times the inlet and farfield boundary conditions are updated by setting the total fluid velocity on those boundaries equal to the viscous potential velocity is shown in the second section of Table 4.4. Both the drag coefficient error and the RMS velocity error decrease as the number of updates is increased. The errors converge to 0.29% for the drag coefficient and 0.15% for the RMS velocity error by around twenty updates. The majority of the error decrease is seen in the first three updates, so three updates will be used in the velocity decomposition solver on the reduced domain.

The parameters selected to be used in the velocity decomposition solver on the reduced domain for the laminar flat plate case are summarized in Table 4.5.

4.1.3 Velocity Decomposition Results

The coarse $10L$ domain used for the RANS solver was trimmed to extend $0.3L$ in the inlet and farfield directions. The reduced domain is shown outlined by a blue

Table 4.4: Influence of update residual, res_{update}, and the number of updates on the drag coefficient error and RMS velocity error for flow over a flat plate at Re = 2000.

res_{update}	# of Updates	Cd Error	RMS u Error
1.0x10^{-3}	2	0.92%	0.47%
1.0x10^{-4}	2	0.77%	0.36%
1.0x10^{-5}	2	0.77%	0.36%
1.0x10^{-4}	1	2.4%	1.3%
1.0x10^{-4}	2	0.77%	0.36%
1.0x10^{-4}	3	0.42%	0.19%
1.0x10^{-4}	4	0.34%	0.16%
1.0x10^{-4}	5	0.32%	0.16%
1.0x10^{-4}	20	0.29%	0.15%
1.0x10^{-4}	50	0.28%	0.15%

Table 4.5: Velocity decomposition solver parameters selected for flow over a flat plate at Re = 2000.

Parameter	Value
α_{vort}	0.01
n_{wp}	11
w_{s}/L	0.2
w_{g}	0.25
# of iterations	2
res_{update}	1.0x10^{-4}
# of updates	3

dashed line in Figure 4.1. The Blasius boundary layer thickness, $\delta^{99\%}$, is defined as

$$\delta^{99\%} = \frac{5.0x}{\sqrt{\text{Re}_x}} \tag{4.6}$$

where x is the distance from the leading edge of the plate. At $x = L$, the Blasius boundary layer thickness is $0.1L$. The vorticity thickness, defined as the distance for the maximum vorticity on the normal to drop two orders of magnitude, is approximately $0.1L$ at the end of the plate, and $0.35L$ at the outlet of the computational domain. The reduced domain extends three times the boundary layer thickness from the body, and extends slightly less than the vorticity thickness at the outlet of the domain.

The domain reduction decreased the number of cells by 64%, from 15,000 to 5,406. The parameters summarized in Table 4.5 are used in the velocity decomposition solver. The values of $\delta_{\max}$ for the body and the wake were reduced from the values discussed in the previous section to $0.15L$ on the body and $0.25L$ in the wake since the domain was reduced to extend $0.3L$ from the body. These lower limits allow the desired vorticity decrease to be found everywhere over the body, and in the first portion of the wake. The margin between $\delta_{\max}$ and the boundary is necessary to ensure that vorticity at the outer boundary is not affecting the value of δ.

Velocity profiles at $x/L = 0.05, 0.25, 0.5, 0.95$, and 1.5 are shown for the velocity decomposition solver on the coarse $0.3L$ mesh and the RANS solver on the coarse $10L$ mesh in Figure 4.3. The solutions visually match very well in the velocity profiles. The RMS error of the x-component of the velocity, u, at ten points located at $y/L = 0.05$ and 0.2 and $x/L = 0.05, 0.25, 0.5, 0.95$, and 1.5 is 0.19%, as shown in Table 4.6. The error between the drag coefficients is 0.42%. The magnitudes of the RMS velocity error and the drag coefficient error are similar to their magnitudes between the RANS solver solutions on the coarse $10L$ domain and fine $10L$ domain of 0.11% and 0.31% respectively. The drag coefficient from the velocity decomposition solver on the $0.3L$ domain is closer to the RANS solver solution on the fine $10L$ domain than the coarse $10L$ solution, with an error of 0.10%. The velocity fields and drag coefficients indicate that the velocity decomposition solver matches the RANS solver extremely well in this laminar flat plate case.

The computation times presented in this thesis are the execution time, which is the elapsed CPU time, for the solution residuals to decrease below their specified final value. In this case, the velocity residuals were required to fall below 1.0×10^{-10} and the pressure residual was required to fall below 1.0×10^{-8}. The computations were performed on a computer with a 2.80GHz Intel® Core$^{\text{TM}}$ 2 Duo processor and 4GB of RAM. While the velocity decomposition solver was written with computation time

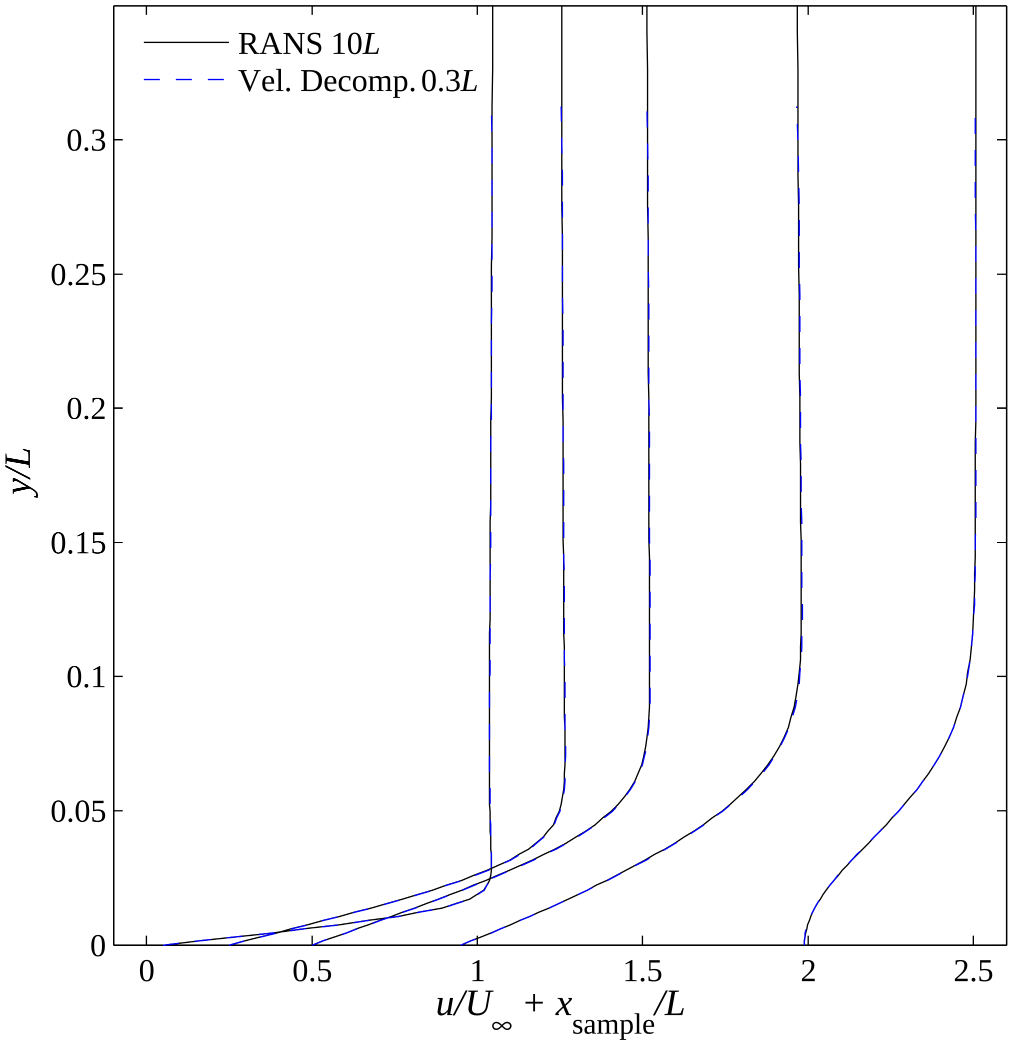

Figure 4.3: RANS and velocity decomposition velocity profiles for flow over a flat plate at Re = 2000.

in mind, the coding has not been fully optimized and hence further time reduction is possible. For this laminar flat plate case, the computation time is reduced from 69.6 seconds for the RANS solver to 22.2 seconds for the velocity decomposition solver, representing a decrease of 68%.

The performance of the velocity decomposition solver on the coarse $0.3L$ domain compared to the RANS solver on the coarse $10L$ domain is summarized in Table 4.6.

Table 4.6: Velocity decomposition solver on $0.3L$ domain compared to RANS solver on $10L$ domain for flow over a flat plate at Re $= 2000$.

# of cells RANS	15,000
# of cells Vel. Decomp.	5,406
Decrease in # of Cells	64%
RMS u error	0.19%
RANS Cd	0.03305
Vel. Decomp. Cd	0.03318
Cd Error	0.42%
RANS Time (sec)	69.6
Vel. Decomp. Time (sec)	22.2
Decrease in Time	68%

4.2 Laminar Cylinder

Laminar flow over a cylinder at a Reynolds number of 60 based on the cylinder diameter, D, is studied with a RANS solver and the velocity decomposition solver. The circular cylinder was chosen to demonstrate the ability of the velocity decomposition solver to handle massively separated flows and the low Reynolds number was chosen to ensure steady flow. Significant separation is generally extremely challenging to handle with boundary element methods; the viscous potential velocity body boundary condition enables the velocity decomposition solver to handle separation. The basic geometry of the computational domain and the coarse $50D$ domain are shown in Figure 4.4. The reduced domain for the velocity decomposition solver is outlined to show the scale of the reduction. The cylinder is centered at $(0, 0)$ with a radius of 0.5 m. The velocity is set equal to the free-stream velocity, $U = 0.00006$ m/s, at the inlet and farfield boundaries, and zero at the wall. The outlet pressure is set to zero to serve as the reference pressure. The velocity at the outlet, and the pressure at the inlet, farfield, and wall are calculated to achieve zero normal gradient. The pressure field is initially set to zero, and the velocity is initially set equal to the free-stream velocity.

The only modifications to the boundary and initial conditions for the velocity decomposition solver are that the flow velocity is initially set equal to the inviscid potential velocity, and the fluid velocity at the inlet and farfield boundaries is set equal to the potential velocity.

4.2.1 RANS Domain Dependence Study

To ensure the accuracy of the RANS solution used to validate the velocity decomposition solver, a study of the computational domain resolution and extent was performed. Coarse, medium, and fine structured meshes extending fifty diameters in the inlet, farfield, and outlet directions from the cylinder were systematically created

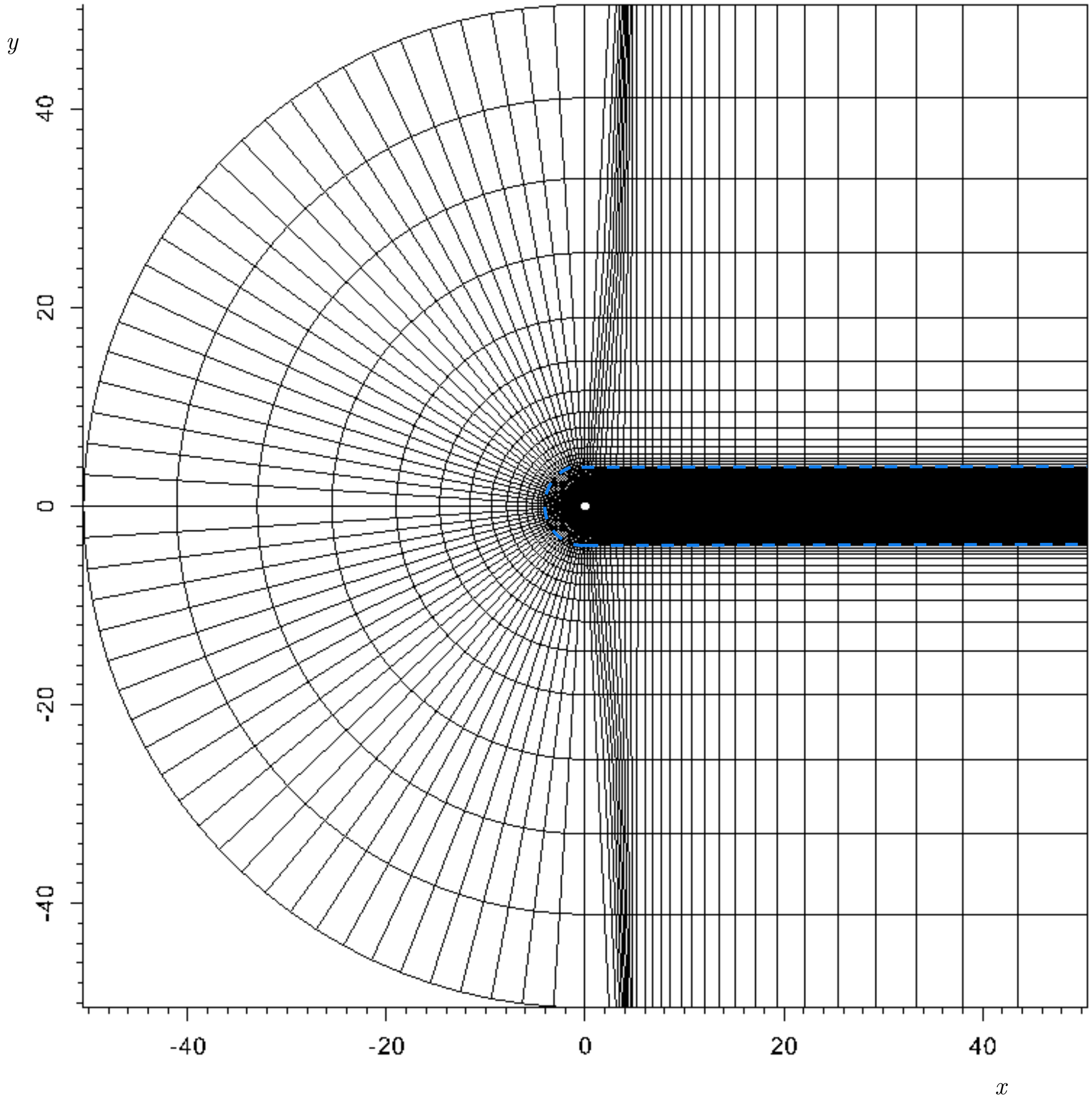

Figure 4.4: Laminar circular cylinder coarse $50D$ mesh with the reduced $3.5D$ domain outlined by the blue dashed line.

by doubling the resolution. The meshes are concentrated around the cylinder and in the wake. Table 4.7 provides the mesh resolution given as the number of cells across the outlet by the number along one side of the inlet and farfield boundaries, number of panels along the body, total number of cells, and mesh refinement factor. The domain extents of the coarse mesh were doubled from fifty to one-hundred times the cylinder diameter by extending the original coarse mesh to ensure the overlapping portion is identical. The largest mesh refinement factor corresponds to the $100D$ coarse mesh, and is due to the large cells extending from the original $50D$ domain.

Table 4.7: Laminar circular cylinder mesh characteristics.

Mesh	Resolution	Body panels	# of Cells	$r_j = h_j/h_{\text{fine}}$
Fine $50D$	416 x 216	400	108,256	1.0
Medium $50D$	208 x 108	200	27,064	2.0
Coarse $50D$	104 x 54	100	6,766	4.0
Coarse $100D$	110 x 59	100	7,640	7.5

Velocity profiles at $x/D = -0.45, -0.25, 0.0, 0.25, 0.45$, and 1 from the three mesh resolutions on the $50D$ domain, and the coarse $100D$ domain are shown to match quite well in the top of Figure 4.5. The bottom of Figure 4.5 shows the error in the drag coefficient and the RMS of the error in the x-component of the velocity, u, at twelve points located at $y/D = 0.55$ and 1.0 and $x/D = -0.45, -0.25, 0.0, 0.25, 0.45$, and 1 with respect to the fine mesh solution as a function of the mesh refinement factor. Table 4.8 provides the error values described above, as well as the errors with respect to the next finer or smaller mesh, and the drag coefficient values. All of the errors are less than 1%. The error in the drag coefficient between the coarse $50D$ mesh and the medium $50D$ mesh is 0.49%, and the error between the coarse $100D$ mesh and the coarse $50D$ mesh is 0.56%, so the coarse $50D$ mesh appears to sufficiently capture the solution and will be the standard against which to compare the velocity decomposition solver.

Table 4.8: Laminar circular cylinder at Re = 60 drag coefficients and error in RANS solver due to domain resolution and extent.

Mesh	Cd	Cd error w/fine	Cd relative error	RMS velocity error w/ fine	RMS velocity relative error
Fine $50D$	1.293				
Medium $50D$	1.295	0.14%	0.14%	0.14%	0.14%
Coarse $50D$	1.301	0.64%	0.49%	0.79%	0.66%
Coarse $100D$	1.294	0.079%	0.56%	0.71%	0.36%

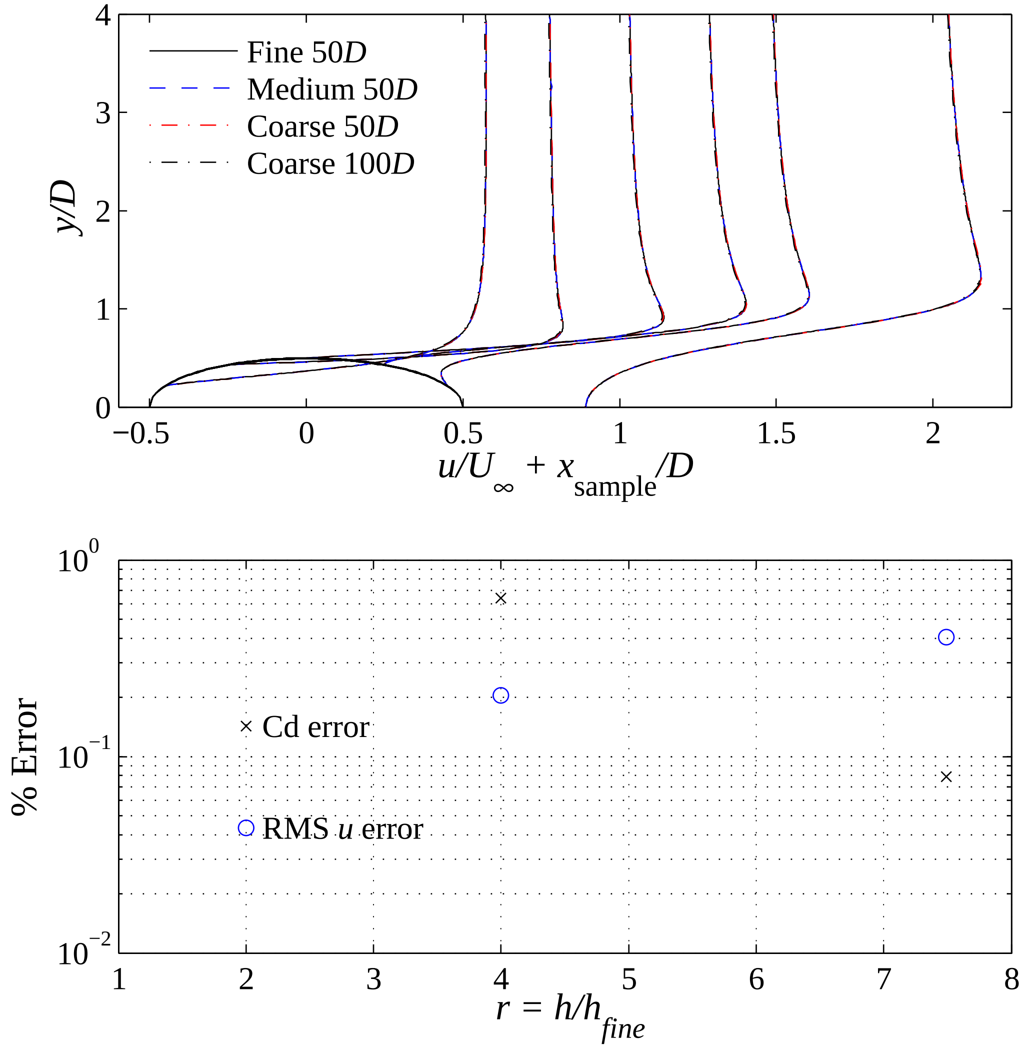

Figure 4.5: RANS solver results for laminar flow over a circular cylinder at Re = 60. Top: Velocity profiles at $x/D = -0.45, -0.25, 0.0, 0.25, 0.45$, and 1. Bottom: Drag coefficient error and RMS velocity error with respect to the finest resolution as a function of mesh refinement factor.

4.2.2 Velocity Decomposition Parameters

To determine the most effective parameters, the velocity decomposition solver was used to calculate the viscous potential velocity given the converged coarse 50D domain RANS velocity field. On the circular cylinder at a Reynolds number of 60, $\delta_{\max}$ was set to 2D on the body and 5D in the wake. The role of $\delta_{\max}$ is more complex on bluff bodies where some of the body panel normals on the downstream side are very closely aligned with the free-stream velocity and hence point into the wake. Higher values of δ_{max} on the body will allow δ to be found further around the trailing edge of the body as the sample line will extend through the wake even at low angles. The more panels δ is defined on, the more influence the viscous effects can have on the viscous potential velocity, leading to a better solution. Recall that if δ is not found for a panel, the non-penetration boundary condition is used on that panel. The main limiting factor for δ_{max} is the size of the reduced domain since the assigned value of δ_{max} applies to the whole body. If higher accuracy is desired on bluff bodies, modifying the algorithm to allow δ_{max} to be longer around the trailing edge would help.

In this case, using a value on the body of $\delta_{\text{max}} = 2.0D$ stays within the reduced domain which extends $3.5D$ from the body in the inlet and farfield directions while providing adequate results. Increasing the value of δ_{max} on the body does slightly improve the results, but extends past the desired reduced domain. A profile of the δ values for each panel are shown super-imposed on the vorticity contours in Figure 4.6. The background of the figure is composed of the vorticity contours on a logarithmic scale. The cells shaded dark gray indicate the cell in which the desired vorticity drop was achieved, which defines δ. The distance from the body to the shaded cell center is δ. The top side of the cylinder shows the contour formed by the cells δ is found in for panels on the body and in the wake. The bottom side only shows the cells δ is found in for panels on the body, demonstrating how far around the body $\delta_{\text{max}} = 2.0D$ allows the sample line to cross through the vorticity in the wake.

As shown in the first section of Table 4.9, fractions ranging from 0.1 to 0.0001 were tested as the fraction, α_{vort}, of the maximum vorticity on a given panel normal that is used to define a negligible vorticity. The average error at δ shows that $\alpha_{\text{vort}} = 0.01$ provides the lowest error between the viscous potential velocity and the converged

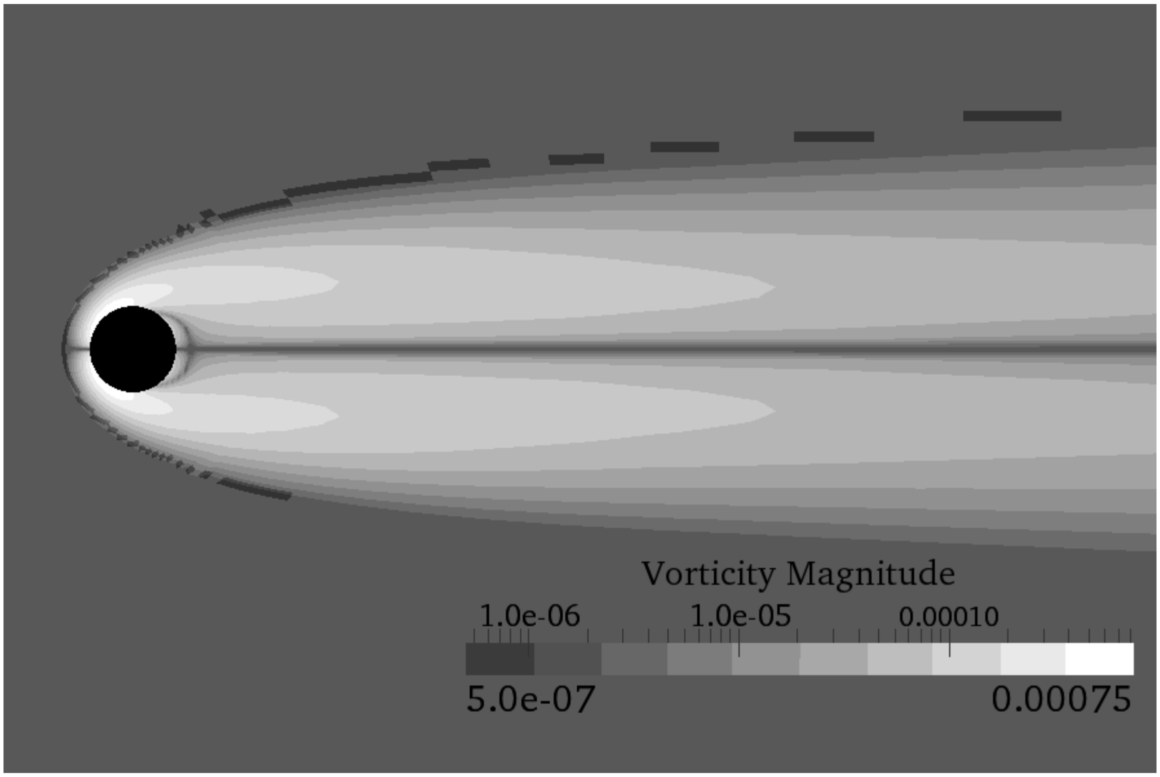

Figure 4.6: Vorticity contours with cells where δ is located shown in dark gray for flow over a circular cylinder at Re = 60 with $\alpha_{\text{vort}} = 0.01$.

fluid velocity, as in the flat plate case. Figure 4.6 shows how δ follows the boundary between the lighter and darker gray, where the vorticity has dropped two orders of magnitude since $\alpha_{\text{vort}} = 0.01$ in this case. The location of δ shifts off of the boundary between the lighter and darker gray in the wake region due to the decrease in the maximum vorticity which causes δ to be located at a lower vorticity, the shade of which is not resolved in this figure.

The second section of Table 4.9 shows the average error at δ for a range of wake panel distributions. The lowest error is achieved with an initial spacing of $w_{\text{s}} = 0.2D$, and a growth rate of $w_{\text{g}} = 0.25$, as was seen in the flat plate case. For this distribution, eighteen panels are used to extend between the cylinder and the end of the domain. The error is increased by both coarsening and refining the wake distribution from these values, though refining the distribution only slightly increases the error. The number of panels could be reduced as the first few have the most impact, but allowing them to extend to the downstream boundary adds very little computation time with this distribution.

The final section in Table 4.9 shows the influence of the number of iterations on the average error at δ for a given fluid velocity field. The best vorticity fraction and wake distribution, as described above, are used, and the average errors between the viscous potential velocity and the fluid velocity are provided at iterations $0-5$, 10, 15, 20, and 25. Note that the error at iteration zero uses the inviscid potential velocity. The initial error between the inviscid potential velocity and the fluid velocity is 21%, which is approximately four times the initial error in the flat plate case due to the more complex geometry. The error decreases most significantly in the first ten iterations, reaching a value of 1.3%; therefore, ten iterations will be used in the solver. The errors in the first two sections of Table 4.9 are higher because only four iterations were used to get those values. Increasing the number of iterations would increase the accuracy if higher accuracy is desired. More iterations are necessary on the circular cylinder than the flat plate to achieve a similar level of accuracy, which is not surprising given the more complex geometry.

The influence of including the viscous effects in the viscous potential velocity through the body boundary condition can be seen in the streamlines and contours shown in Figure 4.7. The background of each image shows the potential velocity magnitude contours. The black lines represent streamlines of the converged total fluid velocity $\mathbf{u}$ from the RANS solver on the coarse $50D$ domain and are the same in the top and bottom images. The blue lines represent streamlines of the potential velocity. The top image shows the inviscid potential velocity contours and streamlines, and it is evident that the inviscid streamlines do not match the total fluid velocity streamlines over the body and in the wake. Including the viscous effects through the body boundary condition pushes the viscous potential velocity streamlines out away

Table 4.9: Influence of the vorticity limit fraction, α_{vort}, wake distribution, and number of iterations on the average error between the viscous potential velocity and the fluid velocity at δ for all body panels for flow over a circular cylinder at Re = 60.

α_{vort}	n_{wp}	w_{s}/D	w_{g}	Iter.	Err(δ)
0.1	18	0.20	0.25	4	467.75%
0.01	18	0.20	0.25	4	3.36%
0.001	18	0.20	0.25	4	3.41%
0.0001	18	0.20	0.25	4	4.02%
0.01	0	–	–	4	6.55%
0.01	15	0.40	0.25	4	4.47%
0.01	18	0.20	0.25	4	3.36%
0.01	21	0.10	0.25	4	3.63%
0.01	37	0.01	0.20	4	3.62%
0.01	18	0.20	0.25	0	20.65%
0.01	18	0.20	0.25	1	9.41%
0.01	18	0.20	0.25	2	5.48%
0.01	18	0.20	0.25	3	4.20%
0.01	18	0.20	0.25	4	3.36%
0.01	18	0.20	0.25	5	2.72%
0.01	18	0.20	0.25	10	1.31%
0.01	18	0.20	0.25	15	1.05%
0.01	18	0.20	0.25	20	0.89%
0.01	18	0.20	0.25	25	0.80%

from the body and the centerline of the wake, causing them to match the total fluid velocity streamlines quite well outside of the vortical region, as shown in the lower image. Ten iterations were used to calculate the body boundary condition for the viscous potential shown.

The final two parameters are the residual, res_{update}, at which to update the total fluid velocity boundary conditions, and the number of times to update the fluid velocity boundary conditions. To determine recommended values for these parameters, the velocity decomposition solver was applied to a reduced domain, and the result compared to the RANS solution on the full domain. The coarse $50D$ circular cylinder mesh described above was trimmed to extend $3.5D$ from the body in the inlet and farfield directions. The outlet extent was not modified. Further details on the

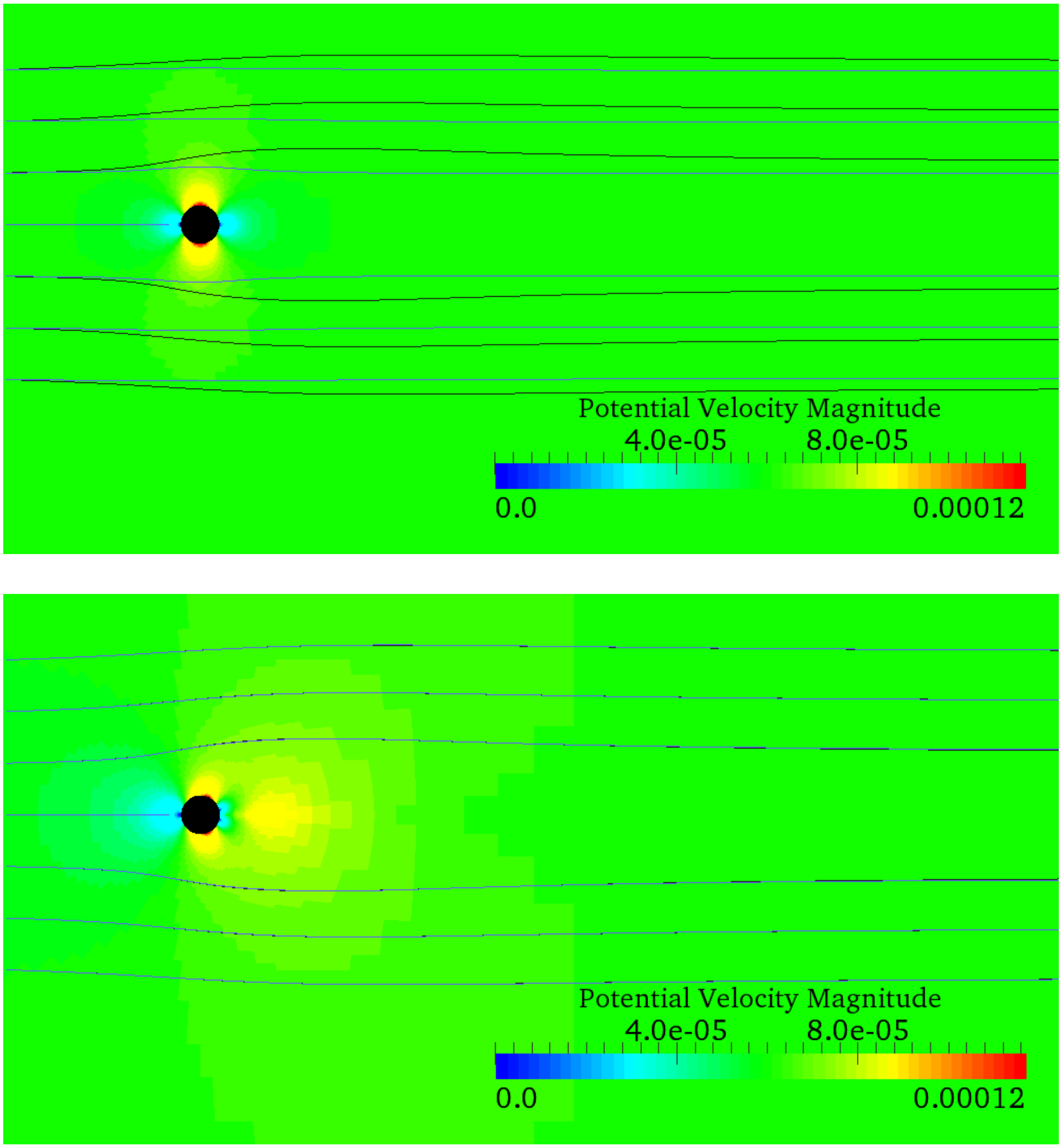

Figure 4.7: Potential velocity contours with streamlines of the converged fluid velocity (black) and the potential velocity (blue) at 0 iterations – inviscid potential (top) and 10 iterations (bottom) for flow over a circular cylinder at Re = 60.

reduced mesh case will be provided in the following section. The coarse $50D$ mesh RANS solution is used as the benchmark. The RMS velocity error is based on the x-component of the velocity, u, at twelve points located at $y/D = 0.55$ and 1.0 and

$x/D = -0.45, -0.25, 0.0, 0.25, 0.45$, and 1.

The first section of Table 4.10 shows the influence of the residual, res_{update}, at which the boundary condition update occurs. Decreasing res_{update} from 1×10^{-3} to 1×10^{-4} reduces the error seen in the velocity field and the drag coefficient. Reducing the residual limit further to 1×10^{-5} slightly increases both errors since it extends δ and therefore relaxes the inclusion of the viscous effects. A residual of 1×10^{-4} will be used.

The influence of the number of times that the inlet and farfield boundary conditions are updated by setting the total fluid velocity on those boundaries equal to the viscous potential velocity is shown in the second section of Table 4.10. The velocity on the reduced domain tends to initially overshoot the value expected based on the large domain result. Each update of the inlet and farfield boundary conditions then decreases the magnitude of the velocity, bringing it to around the expected values at three updates. Further updates continue to decrease the velocity slightly from the expected value to converge to a solution with a drag coefficient error of approximately 0.9% and a RMS velocity error of approximately 0.5%. While it would be preferred that the velocity decomposition converge exactly to the RANS solution on the large domain, it is expected that the solution may be slightly different; the RANS solution also contains errors. The error in the converged result may be reduced by increasing the number of iterations used to determine the viscous potential velocity body boundary condition for a given fluid velocity field. Since three updates appears to usually be where the best solution is achieved, three updates will be used in the solver for the laminar circular cylinder.

The parameters selected to be used in the velocity decomposition solver on the reduced domain for the laminar circular cylinder case are summarized in Table 4.11.

Table 4.10: Influence of update residual, res_{update}, and the number of updates on the drag coefficient error and RMS velocity error for flow over a circular cylinder at Re = 60.

res_{update}	# of Updates	Cd Error	RMS Error
1.0x10^{-3}	2	1.4%	0.76%
1.0x10^{-4}	2	0.44%	0.28%
1.0x10^{-5}	2	0.45%	0.29%
1.0x10^{-4}	1	3.1%	1.6%
1.0x10^{-4}	2	0.44%	0.28%
1.0x10^{-4}	3	0.36%	0.23%
1.0x10^{-4}	4	0.65%	0.37%
1.0x10^{-4}	5	0.80%	0.44%
1.0x10^{-4}	50	0.90%	0.48%
1.0x10^{-4}	200	0.90%	0.49%

Table 4.11: Velocity decomposition solver parameters selected for flow over a circular cylinder at Re = 60.

Parameter	Value
α_{vort}	0.01
n_{wp}	18
w_{s}/D	0.2
w_{g}	0.25
# of iterations	10
res_{update}	1.0x10^{-4}
# of updates	3

4.2.3 Velocity Decomposition Results

The coarse $50D$ domain used for the RANS solver was trimmed to extend $3.5D$ from the body in the inlet and farfield directions. The vorticity thickness, defined as the distance for the maximum vorticity on the normal from the centerline to drop two orders of magnitude, is approximately $4D$ at the outlet of the computational domain. The reduced domain extent of $4D$ from the centerline therefore just encompasses the thickness of the wake.

The domain reduction decreased the number of cells by 24%, from 6,766 to 5,146. The parameters summarized in Table 4.11 are used in the velocity decomposition solver. The value of $\delta_{\max}$ for the body was set to $2.0D$ as in the previous section, and reduced from $5D$ to $3.5D$ in the wake to stay within the reduced domain. These limits allowed δ to be found on the majority of the body as discussed in the previous section, and for the first ten of the eighteen wake panels.

Velocity profiles at $x/D = -0.45, -0.25, 0.0, 0.25, 0.45,$ and 1 are shown for the velocity decomposition solver on the coarse $3.5D$ mesh and the RANS solver on the coarse $50D$ mesh in Figure 4.8. The velocity profiles visually match very well. The RMS error of the x-component of the velocity, u, at twelve points located at $y/D = 0.55$ and 1.0 and $x/D = -0.45, -0.25, 0.0, 0.25, 0.45,$ and 1 is 0.23%, as shown in Table 4.12. The error between the drag coefficients is 0.36%. The RMS velocity error and the drag coefficient error are lower than the errors between the RANS solver solutions on the coarse $50D$ domain and fine $50D$ domain of 0.79% and 0.64% respectively. The drag coefficient from the velocity decomposition solver on the $3.5D$ domain is closer to the RANS solver solution on the fine $50D$ domain than the coarse $50D$ solution, with an error of 0.31%. The velocity fields and drag coefficients indicate that the velocity decomposition solver matches the RANS solver quite well in this laminar circular cylinder case.

For this case, the velocity residuals were required to fall below 1.0×10^{-10} and the pressure residual was required to fall below 1.0×10^{-8}. The computation time is reduced from 19.2 seconds for the RANS solver to 18.6 seconds for the velocity decomposition solver, representing a decrease of 2.8%. The increase in speed is not as significant in the laminar circular cylinder case as in the laminar flat plate case. The bluff body shape requires more iterations to include the viscous effects in the viscous potential body boundary condition. The thick vortical region around the body, and especially in the wake, also limits the domain reduction.

Table 4.12: Velocity decomposition solver on $3.5D$ domain compared to RANS solver on $50D$ domain for flow over a circular cylinder at Re = 60.

# of cells RANS	6,766
# of cells Vel. Decomp.	5,146
Decrease in # of Cells	24%
RMS u error	0.23%
RANS Cd	1.301
Vel. Decomp. Cd	1.297
Cd Error	0.36%
RANS Time (sec)	19.2
Vel. Decomp. Time (sec)	18.6
Decrease in Time	2.8%

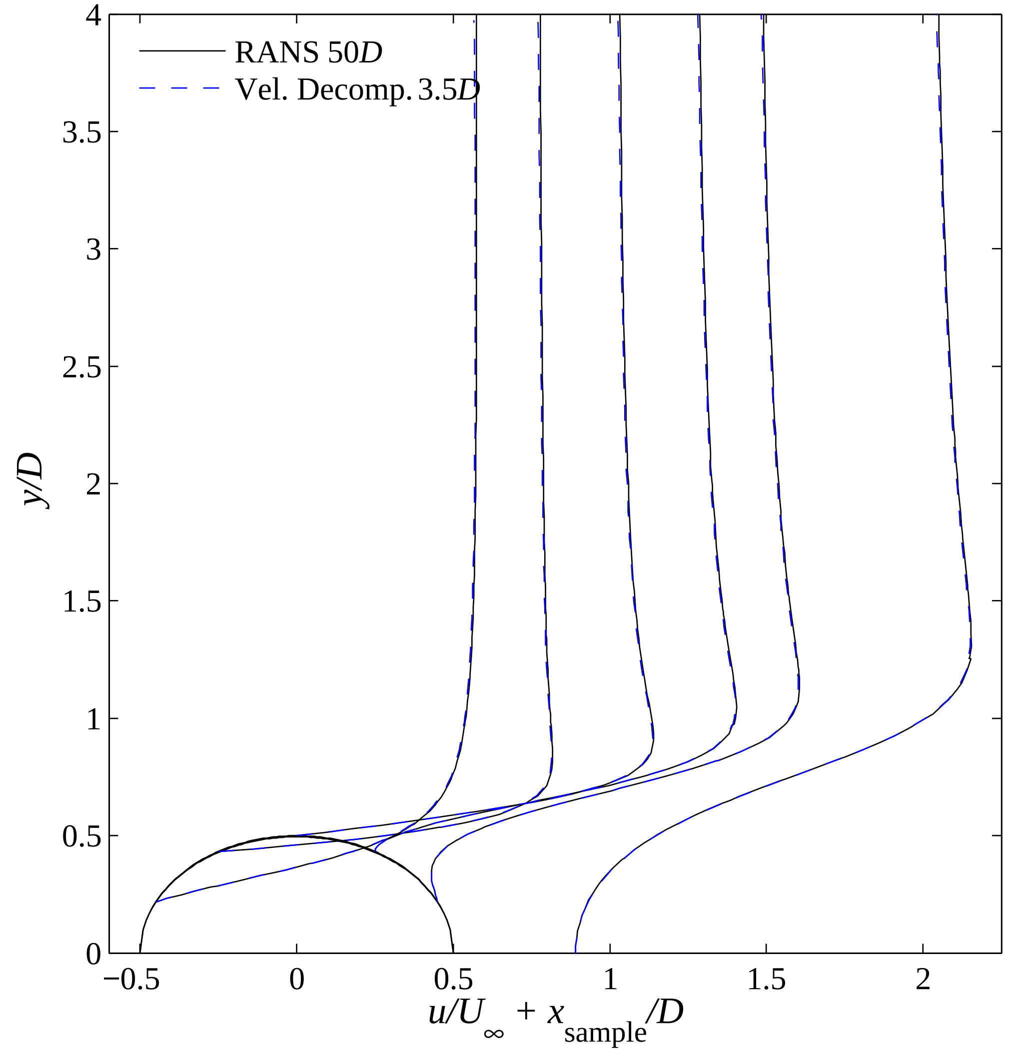

Figure 4.8: RANS and velocity decomposition velocity profiles for flow over a circular cylinder at Re = 60.

4.3 Laminar NACA 0012

Laminar flow over a NACA 0012 airfoil at a Reynolds number of 2000 based on the chord is studied with a RANS solver and the velocity decomposition solver. The computational domain and coarse-medium $20L$ mesh are shown in Figure 4.9, where $L = 1.0$ m is the chord. The reduced domain for the velocity decomposition solver is outlined to show the scale of the reduction. The airfoil is centered vertically on the $x-$axis from $x = 0$ to $x = 1$. For the RANS solver, the velocity is set equal to the free-stream velocity, $U_\infty = 0.002$ m/s at the inlet and farfield boundaries, and zero at the wall. The outlet pressure is set to zero to serve as the reference pressure. The velocity at the outlet, and the pressure at the inlet, farfield, and wall are calculated to achieve zero normal gradient. The pressure field is initially set to zero, and the velocity is initially set equal to the free-stream velocity.

The only modifications to the boundary and initial conditions for the velocity decomposition solver are that the flow velocity is initially set equal to the inviscid potential velocity, and the fluid velocity at the inlet and farfield boundaries is set equal to the potential velocity.

4.3.1 RANS Domain Dependence Study

To ensure the accuracy of the RANS solution used to validate the velocity decomposition solver, a study of the computational domain resolution and extent was performed. Coarse-medium, medium, medium-fine, and fine structured meshes extending twenty chords in the inlet, farfield, and outlet directions from the airfoil were systematically created. The meshes are concentrated around the leading and trailing edges of the airfoil, in the boundary layer, and in the wake. Table 4.13 provides the mesh resolution given as the number of cells across the outlet by the number along one side of the inlet and farfield boundaries, number of body panels, total number of cells, and mesh refinement factor. The domain extents of the coarse-medium

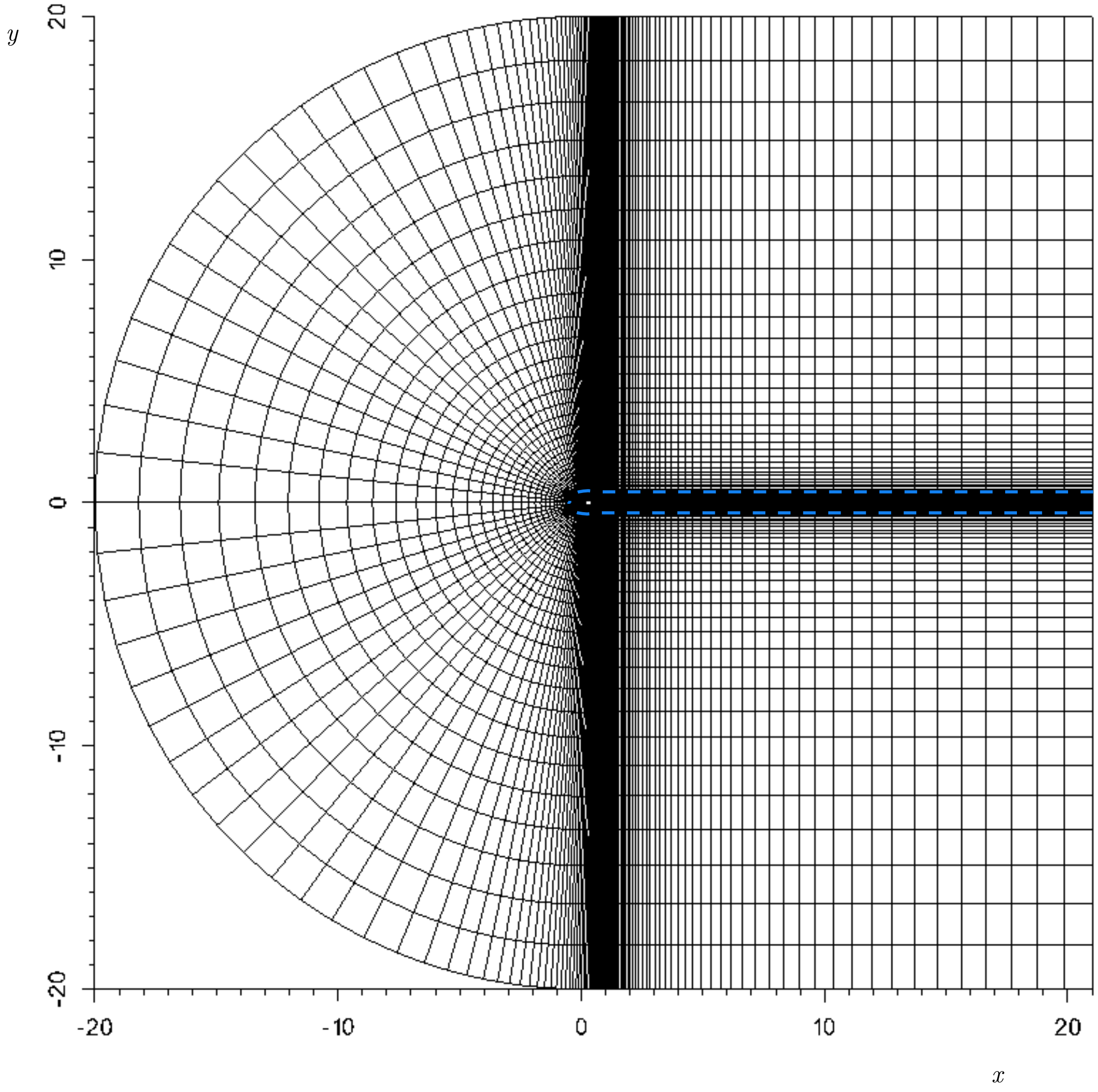

Figure 4.9: Laminar NACA 0012 airfoil coarse-medium $20L$ mesh with the reduced $0.4L$ domain outlined by the blue dashed line.

mesh were doubled from twenty to forty times the chord by extending the original coarse-medium mesh to ensure the overlapping portion is identical.

Velocity profiles at $x/L = 0.05, 0.25, 0.5, 0.95$, and 1.5 from the four mesh resolutions on the $20L$ domain, and the coarse-medium $40L$ domain are shown to match quite well in the top of Figure 4.10. The bottom of Figure 4.10 shows the error in the drag coefficient and the RMS of the error in the x-component of the velocity, u, at ten

Table 4.13: Laminar NACA 0012 airfoil mesh characteristics.

Mesh	Resolution	Body panels	# of Cells	$r_j = h_j/h_{\text{fine}}$
Fine 20L	302 x 398	398	120,196	1.00
Medium-Fine 20L	226 x 298	298	67,348	1.34
Medium 20L	150 x 198	198	29,700	2.01
Coarse-Medium 20L	112 x 148	148	16,576	2.69
Coarse-Medium 40L	134 x 163	148	21,842	4.65

points located at $y/L = 0.075$ and 0.15 and $x/L = 0.05, 0.25, 0.5, 0.95$, and 1.5 with respect to the fine mesh solution as a function of the mesh refinement factor. The coarse-medium 40L mesh has a larger mesh refinement factor due to the addition of larger cells outside of the original 20L domain. Table 4.14 provides the error values described above, as well as the errors with respect to the next finer or smaller mesh, and the drag coefficient values. All of the errors are less than 0.2%. The error in the drag coefficient between the coarse-medium 20L mesh and the medium 20L mesh, which is 1.5 times finer, is 0.034%, and the error between the coarse-medium 40L mesh and the coarse-medium 20L mesh is 0.075%. The coarse-medium 20L mesh appears to sufficiently capture the solution with the least computational expense and will be the standard against which to compare the velocity decomposition solver.

Table 4.14: Laminar NACA 0012 airfoil at Re = 2000 drag coefficients and error in RANS solver due to domain resolution and extent.

Mesh	Cd	Cd error w/fine	Cd rel. error	RMS velocity error w/ fine	RMS velocity relative error
Fine 20L	0.08348				
Med.-Fine 20L	0.08348	0.0083%	0.0083%	0.024%	0.024%
Medium 20L	0.08351	0.039%	0.030%	0.043%	0.042%
Coarse-Med. 20L	0.08354	0.073%	0.034%	0.15%	0.12%
Coarse-Med. 40L	0.08348	0.0026%	0.075%	0.16%	0.048%

4.3.2 Velocity Decomposition Parameters

In the interest of demonstrating the ability of the velocity decomposition solver without completing a study of the parameters, the parameters were selected for the

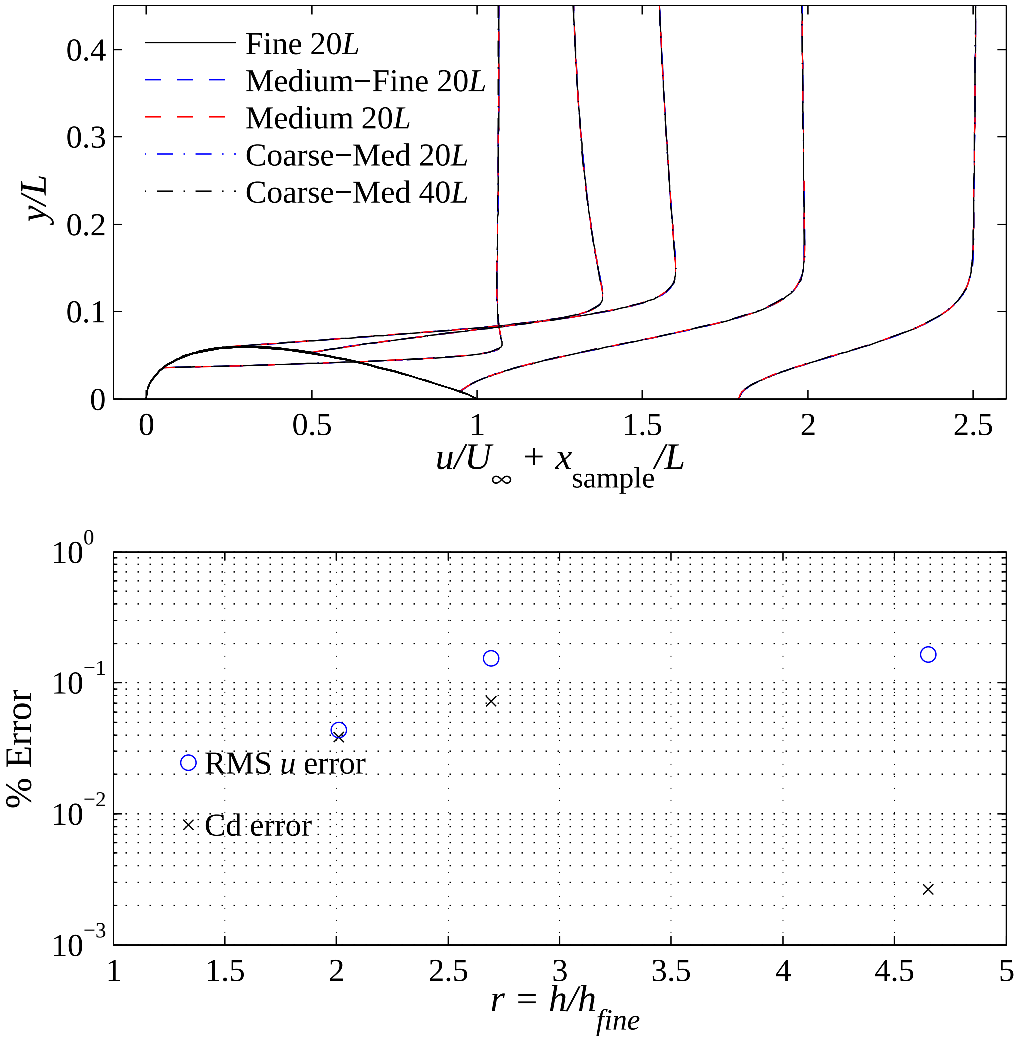

Figure 4.10: RANS solver results for laminar flow over a NACA 0012 airfoil at Re = 2000. Top: Velocity profiles at $x/L = 0.05, 0.25, 0.5, 0.95$, and 1.5. Bottom: Drag coefficient error and RMS velocity error with respect to the finest resolution as a function of mesh refinement factor.

NACA 0012 airfoil based on their effects in the laminar flat plate and circular cylinder cases. The parameters selected to be used in the velocity decomposition solver on the reduced domain for the laminar NACA 0012 airfoil case are summarized in Table 4.15.

Table 4.15: Velocity decomposition solver parameters selected for flow over a NACA 0012 airfoil at Re = 2000.

Parameter	Value
α_{vort}	0.01
n_{wp}	14
w_{s}/L	0.2
w_{g}	0.25
# of iterations	3
res_{update}	1.0x10^{-4}
# of updates	3

4.3.3 Velocity Decomposition Results

The coarse-medium $20L$ domain used for the RANS solver was trimmed to extend $0.4L$ in the inlet and farfield directions. The vorticity thickness is approximately $0.2L$ at the end of the airfoil, and $0.4L$ at the outlet of the computational domain. The reduced domain extends two times the vorticity thickness from the body, and extends slightly past the vorticity thickness at the outlet of the domain.

The domain reduction decreased the number of cells by 55%, from 16,576 to 7,400. The parameters summarized in Table 4.15 are used in the velocity decomposition solver. The values of δ_{max} are $0.3L$ on the body and $0.35L$ in the wake. These limits allow the desired vorticity decrease to be found everywhere over the body, and on nine of the fourteen wake panels.

Velocity profiles at $x/L = 0.05, 0.25, 0.5, 0.95$, and 1.5 are shown for the velocity decomposition solver on the coarse-medium $0.4L$ mesh and the RANS solver on the coarse-medium $20L$ mesh in Figure 4.11. The velocity profiles visually match very well. The RMS error of the x-component of the velocity, u, at ten points located at $y/L = 0.075$ and 0.15 and $x/L = 0.05, 0.25, 0.5, 0.95$, and 1.5 is 0.064%, as shown in Table 4.16. The error between the drag coefficients is 0.21%. The velocity fields and drag coefficients indicate that the velocity decomposition solver matches the RANS solver very well for the laminar NACA 0012 airfoil case using parameters based on the flat plate and cylinder cases.

For this case, the velocity residuals were required to fall below 1.0×10^{-10} and the pressure residual was required to fall below 1.0×10^{-8}. The computation time is reduced from 108.8 seconds for the RANS solver to 59.8 seconds for the velocity decomposition solver, representing a decrease of 45%.

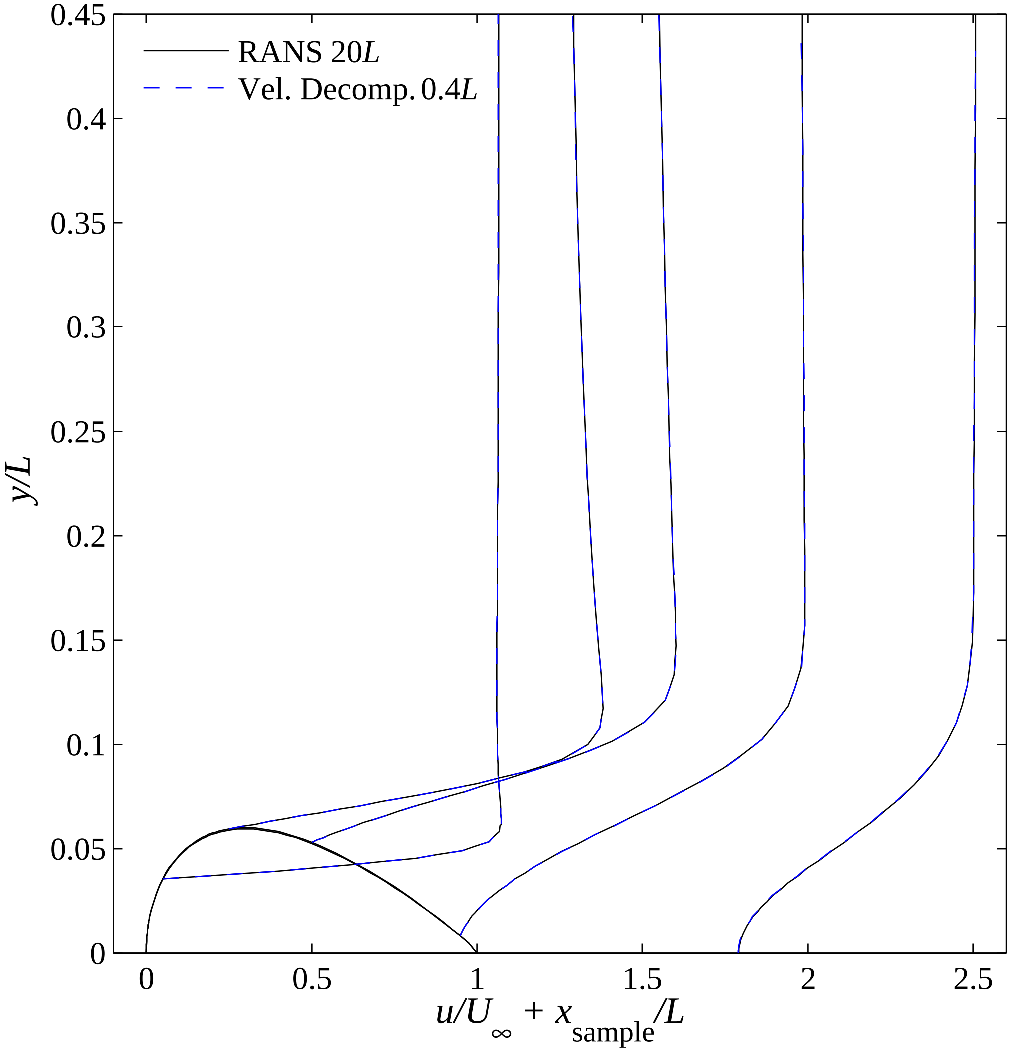

Figure 4.11: RANS and velocity decomposition velocity profiles for flow over a NACA 0012 airfoil at Re = 2000.

Table 4.16: Velocity decomposition solver on $0.4L$ domain compared to RANS solver on $20L$ domain for flow over a NACA 0012 airfoil at Re = 2000.

# of cells RANS	16,576
# of cells Vel. Decomp.	7,400
Decrease in # of Cells	55%
RMS u error	0.064%
RANS Cd	0.08354
Vel. Decomp. Cd	0.08371
Cd Error	0.21%
RANS Time (sec)	108.8
Vel. Decomp. Time (sec)	59.8
Decrease in Time	45%

CHAPTER V

Turbulent Two-Dimensional Results

Results for steady turbulent flow over a flat plate and a NACA 0012 airfoil are presented. The RANS solver is used to generate solutions with which to compare the velocity decomposition solver results. The parameters used in the velocity decomposition solver are studied in the turbulent flat plate case. The turbulent flat plate case, in addition to the laminar flat plate and circular cylinder cases, are then used to guide the selection of the parameters for the NACA 0012 airfoil. The velocity decomposition solver is shown to obtain results that compare very well with the RANS solutions in less computation time.

For each case, the problem is stated and the RANS solution is developed. The velocity decomposition parameters are then discussed. Finally, the velocity decomposition solver solutions are compared to the RANS solver solutions.

5.1 Turbulent Flat Plate

Turbulent flow over a flat plate at a Reynolds number of 6×10^6 based on the plate length was modeled with a RANS solver and the velocity decomposition solver. The computational domain and coarse $0.5L$ mesh used for the RANS solver are shown in Figure 5.1, where $L = 1.0$ m is the plate length. The reduced domain used for the velocity decomposition solver is outlined to show the scale of the reduction. The plate is located on the $x-$axis from $x = 0$ to $x = 1$.

For the RANS solver, the velocity is set equal to the free-stream velocity, $U_\infty = 6.0$ m/s, at the inlet and farfield boundaries, and zero at the wall. The outlet pressure is set to zero to serve as the reference pressure. The velocity at the outlet, and the pressure at the inlet, farfield, wall, and center plane are calculated to achieve zero normal gradient. A slip boundary condition, which sets the normal component to zero and enforces zero normal gradient on the tangential component, is used for the velocity on the center plane before and after the plate. The pressure field is initially set to zero, and the velocity is initially set equal to the free-stream velocity.

The $k-\omega$ SST turbulence model is used. The free-stream turbulent kinetic energy used as the initial condition and the boundary condition on the inlet and farfield boundaries is calculated using Equation 5.1.

$$k = \frac{3}{2}(U_\infty I)^2 \tag{5.1}$$

where I is the turbulence intensity, which was set to 2% in this case. The kinematic eddy viscosity is initially set equal to ten times the kinematic viscosity, $\nu_t = 10\nu$. The free-stream value of the specific dissipation rate, ω, used for the initial condition and the inlet and farfield boundary conditions, is set according to the relation $\omega = k/\nu_t$. The turbulent kinetic energy and the specific dissipation rate are calculated to achieve zero normal gradient on the center plane before and after the plate and the outlet. Wall functions are used in this case. Low-Reynolds number models, such as the Spalart-Allmaras model without wall functions, have also been used successfully with the velocity decomposition solver.

The only modification to the boundary conditions for the velocity decomposition solver is that the fluid velocity at the inlet and farfield boundaries is set equal to the potential velocity.

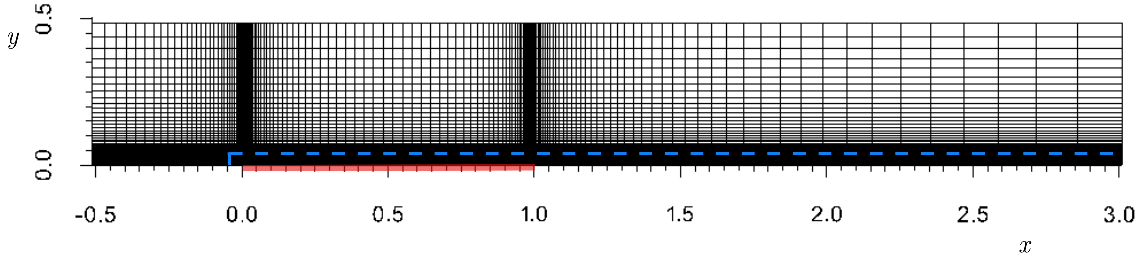

Figure 5.1: Turbulent flat plate coarse $0.5L$ mesh with the reduced $0.04L$ domain outlined by the blue dashed line.

5.1.1 RANS Domain Dependence Study

To ensure the accuracy of the RANS solution used to validate the velocity decomposition solver, a study of the computational domain resolution and extent was performed. Coarse and fine structured meshes extending one plate length in the inlet and farfield directions and two plate lengths in the outlet direction from the plate were systematically created by doubling the resolution. The meshes are concentrated around the leading and trailing edges of the plate, and in the boundary layer. Table 5.1 provides the mesh resolution given as the number of cells normal to the plate by the number along the length of the domain, number of panels along the plate, total number of cells, and mesh refinement factor. The domain extents of the coarse mesh were trimmed from one to one-half a plate length in the inlet and farfield directions while leaving the outlet extent at two plate lengths.

Table 5.1: Turbulent flat plate mesh characteristics.

Mesh	Resolution	Plate panels	# of Cells	$r_j = h_j/h_{\text{fine}}$
Fine $1L$	159 x 337	159	53,583	1.0
Coarse $1L$	79 x 167	79	13,193	2.0
Coarse $0.5L$	72 x 159	79	11,448	1.4

Velocity profiles at $x/L = 0.25, 0.5, 0.95$, and 1.5 from the two mesh resolutions on the $1.0L$ domain, and the coarse $0.5L$ domain are shown to match fairly well in Figure 5.2. There is a minor difference between the coarse meshes and the fine mesh in the boundary layer towards the leading edge of the plate. The error in the drag coefficient and the RMS of the error in the x-component of the velocity, u, at ten points located at $y/L = 0.01$ and 0.035 and $x/L = 0.05, 0.25, 0.5, 0.95$, and 1.5 with respect to the fine mesh solution are provided in Table 5.2. The errors with respect to the next finer or smaller mesh, and the drag coefficient values are also provided in Table 5.2. All of the errors are less than 1%. The error in the drag coefficient between the coarse $1L$ mesh and the fine $1L$ mesh is 0.86%, and the error between the coarse $0.5L$ mesh and the coarse $1L$ mesh is 0.64%, so the coarse $0.5L$ mesh appears to sufficiently capture the solution and will be used as the standard against which to compare the velocity decomposition solver results.

Table 5.2: Turbulent flat plate at Re $= 6 \times 10^6$ drag coefficients and error in RANS solver due to domain resolution and extent.

Mesh	Cd	Cd error w/fine	Cd relative error	RMS velocity error w/ fine	RMS velocity relative error
Fine $1L$	0.002912				
Coarse $1L$	0.002887	0.86%	0.86%	0.061%	0.061%
Coarse $0.5L$	0.002906	0.22%	0.64%	0.12%	0.10%

5.1.2 Velocity Decomposition Parameters

To determine the effects of the velocity decomposition parameters, the velocity decomposition solver was used to calculate the viscous potential velocity given the converged coarse $0.5L$ RANS fluid velocity field described in the previous section. For the flat plate at a Reynolds number of 6×10^6, δ_{max} was set to $0.02L$ on the body and $0.04L$ in the wake. These values allowed the algorithm to find the desired vorticity drop for all panels.

As shown in the first section of Table 5.3, fractions ranging from 0.1 to 0.0001 were tested as the fraction, α_{vort}, of the maximum vorticity on a given panel normal that is used to define a negligible vorticity. The trend in the average error at δ is similar to the laminar cases in that it decreases significantly as α_{vort} is lowered from 0.1 to

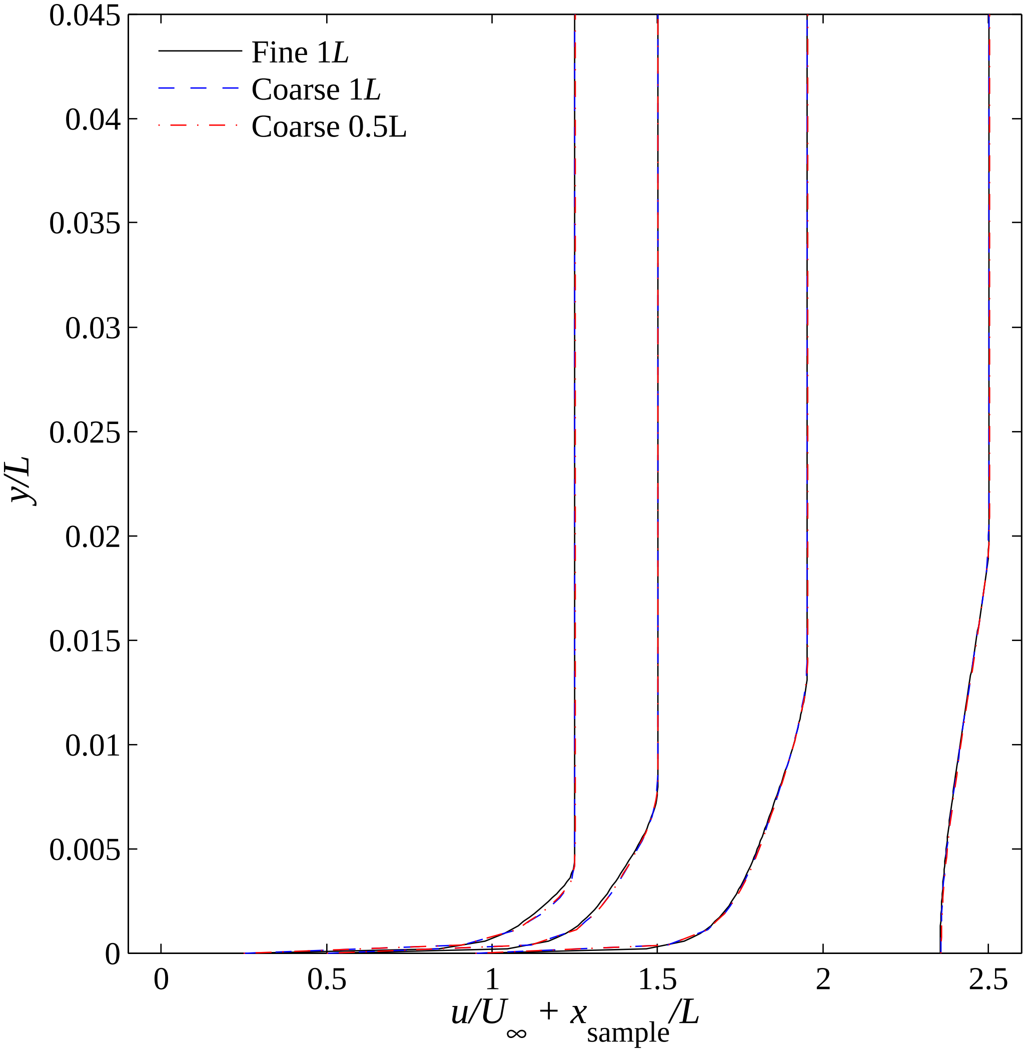

Figure 5.2: Velocity profiles at $x/L = 0.25, 0.5, 0.95$, and 1.5 from the RANS solver for turbulent flow over a flat plate at $\mathrm{Re} = 6 \times 10^6$.

0.01, then increases slightly again when α_{vort} is lowered to 0.001. Unlike the laminar cases, further lowering α_{vort} to 0.0001 decreases the average error at δ slightly more. The error appears to be oscillating slightly around an error of 0.185% for the three lower values of α_{vort}. Since the three lower limits have approximately the same error and using the higher values of α_{vort}, which lead to lower δ values, tends to achieve a better solution in fewer iterations, $\alpha_{\mathrm{vort}} = 0.01$ will be used as in the laminar cases.

The second section of Table 5.3 shows the average error at δ for a range of wake panel distributions. Refining the wake by decreasing the initial spacing, w_{s}, decreases the average error at δ. The gain from increasing the resolution from an initial spacing of $0.1L$ with eight panels to an intial spacing of $0.01L$ with twenty panels is only 0.001%, so the former is used as the distribution for the velocity decomposition solver on the reduced domain.

The final section in Table 5.3 shows the influence of the number of iterations on the average error at δ for a given fluid velocity field. The vorticity fraction and wake distributions selected above are used, and the average errors between the viscous potential velocity and the fluid velocity are provided at iterations $0-5$, 10, 15, 20, and 25. Note that the error at iteration zero uses the inviscid potential velocity. The viscous potential velocity approximates the fluid velocity at δ quite well, and converges toward a solution with an average error of approximately 0.185% by 3 iterations. Since the majority of the error reduction occurs in the first two iterations, two iterations are used in the velocity decomposition solver on the reduced domain. As expected based on the smaller viscous boundary layer in turbulent flows, the average error at δ between the inviscid potential velocity and the fluid velocity is lower in the turbulent case than the laminar case – 0.3% versus 5%.

The final two parameters are the residual, res_{update}, at which to update the velocity boundary conditions, and the number of times to update the velocity boundary conditions. To determine recommended values for these parameters, the velocity decomposition solver was applied to a reduced domain, and the result compared to the RANS solution on the full domain. The coarse $0.5L$ flat plate mesh described above was trimmed to extend $0.04L$ in the inlet and farfield directions. The outlet extent was not modified. Further details on the reduced mesh case are provided in the following section. The coarse $0.5L$ mesh RANS solution is used as the benchmark. The RMS velocity error is based on the x-component of the velocity, u, at ten points

Table 5.3: Influence of the vorticity limit fraction, α_{vort}, wake distribution, and number of iterations on the average error between the viscous potential velocity and the fluid velocity at δ for all body panels for flow over a flat plate at $\mathrm{Re} = 6 \times 10^6$.

α_{vort}	n_{wp}	w_{s}/L	w_{g}	Iter.	$\mathrm{Err}(\delta)$
0.1	8	0.20	0.25	4	0.417%
0.01	8	0.20	0.25	4	0.185%
0.001	8	0.20	0.25	4	0.186%
0.0001	8	0.20	0.25	4	0.184%
0.01	0	–	–	4	0.211%
0.01	3	0.40	0.25	4	0.194%
0.01	5	0.20	0.25	4	0.189%
0.01	8	0.10	0.25	4	0.185%
0.01	20	0.01	0.20	4	0.184%
0.01	8	0.10	0.25	0	0.349%
0.01	8	0.10	0.25	1	0.191%
0.01	8	0.10	0.25	2	0.186%
0.01	8	0.10	0.25	3	0.185%
0.01	8	0.10	0.25	4	0.185%
0.01	8	0.10	0.25	5	0.185%
0.01	8	0.10	0.25	10	0.185%
0.01	8	0.10	0.25	15	0.185%
0.01	8	0.10	0.25	20	0.185%
0.01	8	0.10	0.25	25	0.185%

located at $y/L = 0.01$ and 0.035 and $x/L = 0.05, 0.25, 0.5, 0.95$, and 1.5.

The first section of Table 5.4 shows the influence of the residual, res_{update}, at which the boundary condition update occurs. The errors in the drag coefficient and the velocity field are extremely close for the three residuals evaluated. Based on the trends of the laminar cases in addition to the performance of this case, a residual limit of 1×10^{-4} is used in the velocity decomposition solver.

The influence of the number of times that the inlet and farfield boundary conditions are updated by setting the total fluid velocity equal to the viscous potential velocity is shown in the second section of Table 5.4. The drag coefficient error converges to a value of 0.85% and the RMS velocity error converges to 0.27%. Three updates are used in the velocity decomposition solver.

Table 5.4: Influence of update residual, res_{update}, and the number of updates on the drag coefficient error and RMS velocity error for flow over a flat plate at $\text{Re} = 6 \times 10^6$.

res_{update}	# of Updates	Cd Error	RMS Error
$1.0x10^{-3}$	2	1.06%	0.146%
$1.0x10^{-4}$	2	1.06%	0.144%
$1.0x10^{-5}$	2	1.06%	0.144%
$1.0x10^{-4}$	1	1.78%	0.314%
$1.0x10^{-4}$	2	1.06%	0.144%
$1.0x10^{-4}$	3	0.907%	0.234%
$1.0x10^{-4}$	4	0.870%	0.258%
$1.0x10^{-4}$	5	0.860%	0.265%
$1.0x10^{-4}$	10	0.856%	0.267%
$1.0x10^{-4}$	50	0.856%	0.268%

The parameters selected to be used in the velocity decomposition solver on the reduced domain for the turbulent flat plate case are summarized in Table 5.5.

5.1.3 Velocity Decomposition Results

The coarse $0.5L$ domain used for the RANS solver was trimmed to extend $0.04L$ in the inlet and farfield directions. At $x = L$, the Blasius boundary layer thickness

Table 5.5: Velocity decomposition solver parameters selected for flow over a flat plate at Re $= 6 \times 10^6$.

Parameter	Value
α_{vort}	0.01
n_{wp}	8
w_{s}/L	0.1
w_{g}	0.25
# of iterations	2
res_{update}	1.0x10^{-4}
# of updates	3

is $0.002L$. The vorticity thickness, defined as the distance for the maximum vorticity on the normal to drop two orders of magnitude, is approximately $0.02L$ at the end of the plate, and $0.04L$ at the outlet of the computational domain. The reduced domain extends two times the boundary layer thickness from the body, and extends slightly past the vorticity thickness at the outlet of the domain.

The domain reduction decreased the number of cells by 51%, from 11,448 to 5,617. The parameters summarized in Table 5.5 are used in the velocity decomposition solver. The values of δ_{max} are $0.025L$ on the body and $0.035L$ in the wake. These limits allow the desired vorticity decrease to be found everywhere over the body, and on all but the final wake panel.

Velocity profiles at $x/L = 0.25, 0.5, 0.95$, and 1.5 are shown for the velocity decomposition solver on the coarse $0.04L$ mesh and the RANS solver on the coarse $0.5L$ mesh in Figure 5.3. The solutions visually match very well in the velocity profiles, though there is enough difference to show a distinction between the lines in some areas. The RMS error in the x-component of the velocity, u, at ten points located at $y/L = 0.01$ and 0.035 and $x/L = 0.05, 0.25, 0.5, 0.95$, and 1.5 is 0.23%, as shown in Table 5.6. The error between the drag coefficients is 0.91%. The velocity fields and drag coefficients indicate the velocity decomposition solver matches the RANS solver well.

For this case, the velocity residuals were required to fall below 1.0×10^{-10} and the pressure, turbulent kinetic energy, and specific dissipation rate residuals were required to fall below 1.0×10^{-8}. The computation time is reduced from 29.3 seconds for the RANS solver to 26.7 seconds for the velocity decomposition solver, representing a decrease of 8.9%.

Table 5.6: Velocity decomposition solver on $0.04L$ domain compared to RANS solver on $0.5L$ domain for flow over a flat plate at $\mathrm{Re} = 6 \times 10^6$.

# of cells RANS	11,448
# of cells Vel. Decomp.	5,617
Decrease in # of Cells	51%
RMS u error	0.23%
RANS Cd	0.002906
Vel. Decomp. Cd	0.002932
Cd Error	0.91%
RANS Time (sec)	29.3
Vel. Decomp. Time (sec)	26.7
Decrease in Time	8.9%

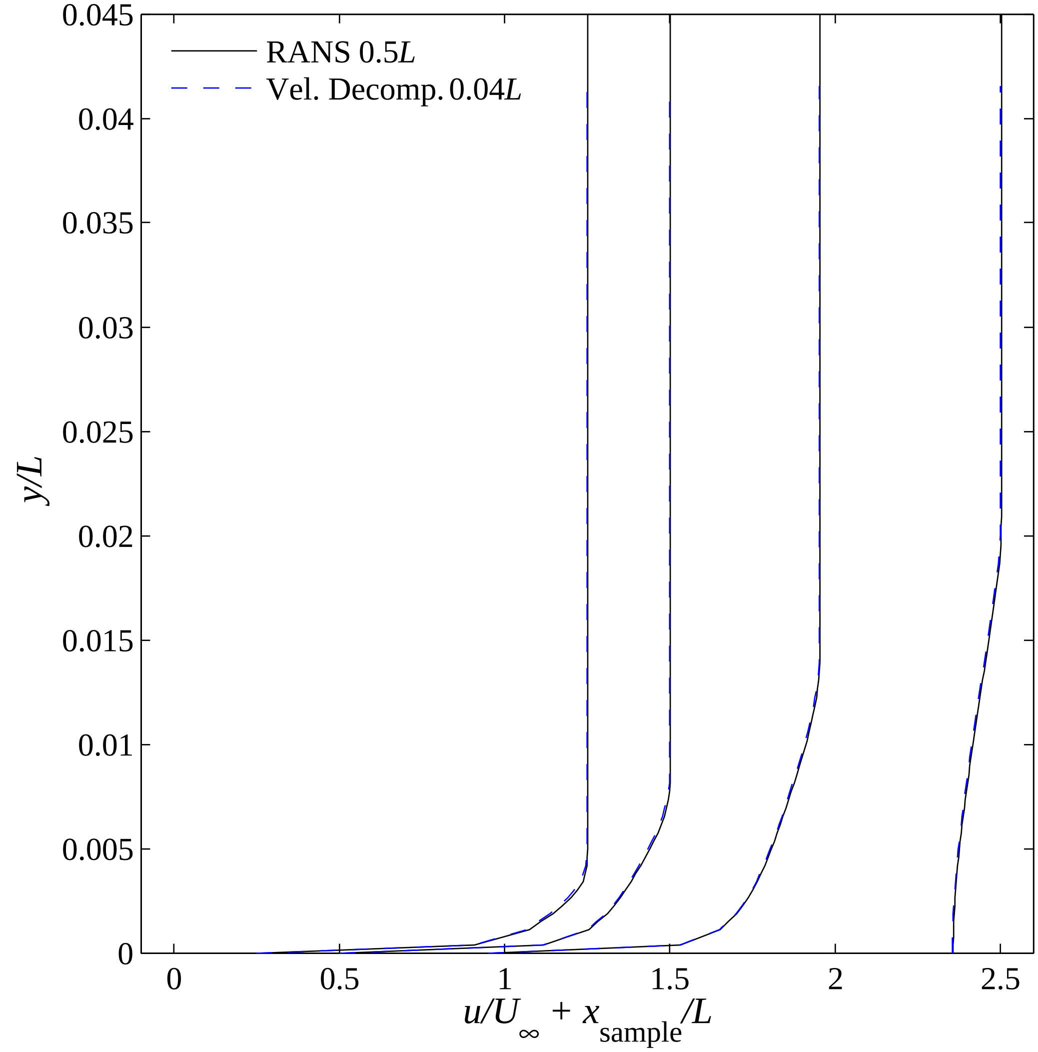

Figure 5.3: RANS and velocity decomposition velocity profiles for flow over a flat plate at $\mathrm{Re} = 6 \times 10^6$.

5.2 Turbulent NACA 0012

Turbulent flow over a NACA 0012 airfoil at a Reynolds number of 6×10^6 based on the chord, L, is modeled with a RANS solver and the velocity decomposition solver. The computational domain and coarse $5L$ mesh are shown in Figure 5.4, where $L = 1.0$ m is the chord. The reduced domain used for the velocity decomposition solver is outlined to show the scale of the reduction. The airfoil is centered vertically on the $x-$axis from $x = 0$ to $x = 1$.

For the RANS solver, the velocity is set equal to the free-stream velocity, $U_\infty = 6.0$ m/s, at the inlet and farfield boundaries, and zero at the wall. The outlet pressure is set to zero to serve as the reference pressure. The velocity at the outlet, and the pressure at the inlet, farfield, and wall are calculated to achieve zero normal gradient. The pressure field is initially set to zero, and the velocity is initially set equal to the free-stream velocity.

The $k-\omega$ SST turbulence model is used. The free-stream turbulent kinetic energy used as the initial condition and the boundary condition on the inlet and farfield boundaries is calculated using Equation 5.1 with a turbulence intensity of $I = 0.1\%$. The kinematic eddy viscosity is initially set equal to ten times the kinematic viscosity, $\nu_t = 10\nu$. The free-stream value of the specific dissipation rate, ω, used for the initial condition and the inlet and farfield boundary conditions, is set according to the relation $\omega = k/\nu_t$. The turbulent kinetic energy and the specific dissipation rate are calculated to achieve zero normal gradient at the outlet. Wall functions are used.

The only modifications to the boundary and initial conditions for the velocity decomposition solver are that the flow velocity is initially set equal to the inviscid potential velocity, and the fluid velocity at the inlet and farfield boundaries is set equal to the potential velocity.

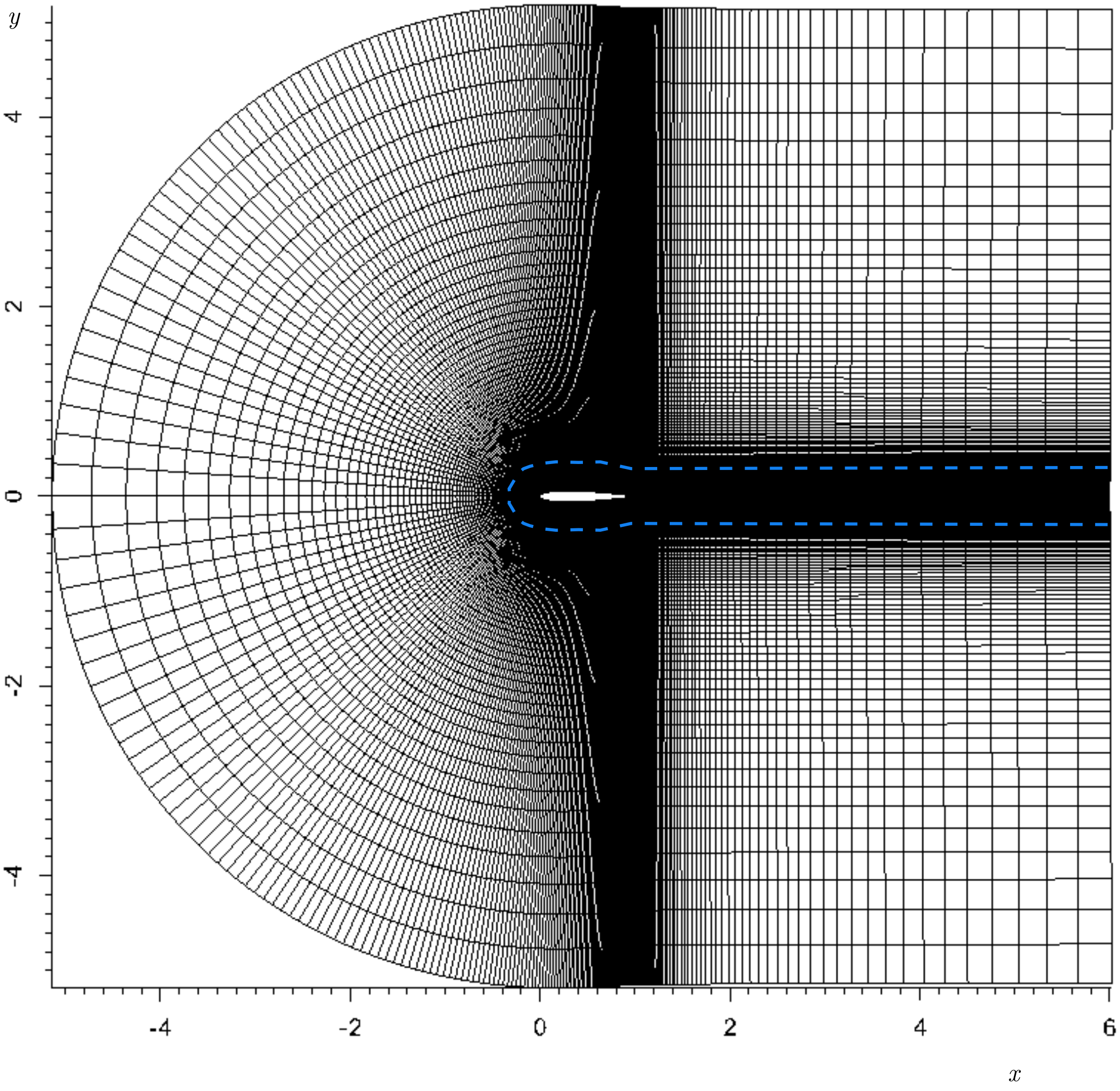

Figure 5.4: Turbulent NACA 0012 airfoil medium $5L$ mesh with the reduced $0.3L$ domain outlined by the blue dashed line.

5.2.1 RANS Domain Dependence Study

To ensure the accuracy of the RANS solution used to validate the velocity decomposition solver, a study of the computational domain resolution and extent was performed. Coarse and fine structured meshes extending five chords in the inlet, farfield, and outlet directions from the airfoil were systematically created by doubling the resolution. The meshes are concentrated around the leading and trailing edges of the airfoil, in the boundary layer, and in the wake. Table 5.7 provides the mesh resolution given as the number of cells across the outlet by the number along one side of the inlet and farfield boundaries, number of body panels, total number of cells, and mesh refinement factor. The domain extents of the coarse mesh were extended from five chords to eleven chords.

Table 5.7: Turbulent NACA 0012 airfoil mesh characteristics.

Mesh	Resolution	Body panels	# of Cells	$r_j = h_j/h_{\text{fine}}$
Fine $5L$	556 x 464	600	257,984	1.0
Coarse $5L$	280 x 232	300	64,960	2.0
Coarse $11L$	294 x 242	300	71,148	4.0

Velocity profiles at $x/L = 0.25, 0.5, 0.95$, and 1.5 from the two mesh resolutions on the $5L$ domain, and the coarse $11L$ domain are shown to match well in Figure 5.5. The error in the drag coefficient and the RMS of the error in the x-component of the velocity, u, at ten points located at $y/L = 0.065$ and 0.09 and $x/L = 0.05, 0.25, 0.5, 0.95$, and 1.5 with respect to the fine mesh solution are provided in Table 5.8. The errors with respect to the next finer or smaller mesh, and the drag coefficient values are also provided in Table 5.8. The error in the drag coefficient between the coarse $5L$ mesh and the fine $5L$ mesh is 1.4%, and the error between the coarse $11L$ mesh and the coarse $5L$ mesh is 0.29%. The coarse $5L$ mesh appears to sufficiently capture the solution and will be used as the standard against which to compare the velocity decomposition solver.

Table 5.8: Turbulent NACA 0012 airfoil at Re $= 6 \times 10^6$ drag coefficients and error in RANS solver due to domain resolution and extent.

Mesh	Cd	Cd error w/fine	Cd relative error	RMS velocity error w/ fine	RMS velocity relative error
Fine $5L$	0.007710				
Coarse $5L$	0.007604	1.4%	1.4%	0.021%	0.021%
Coarse $11L$	0.007582	1.7%	0.29%	0.11%	0.097%

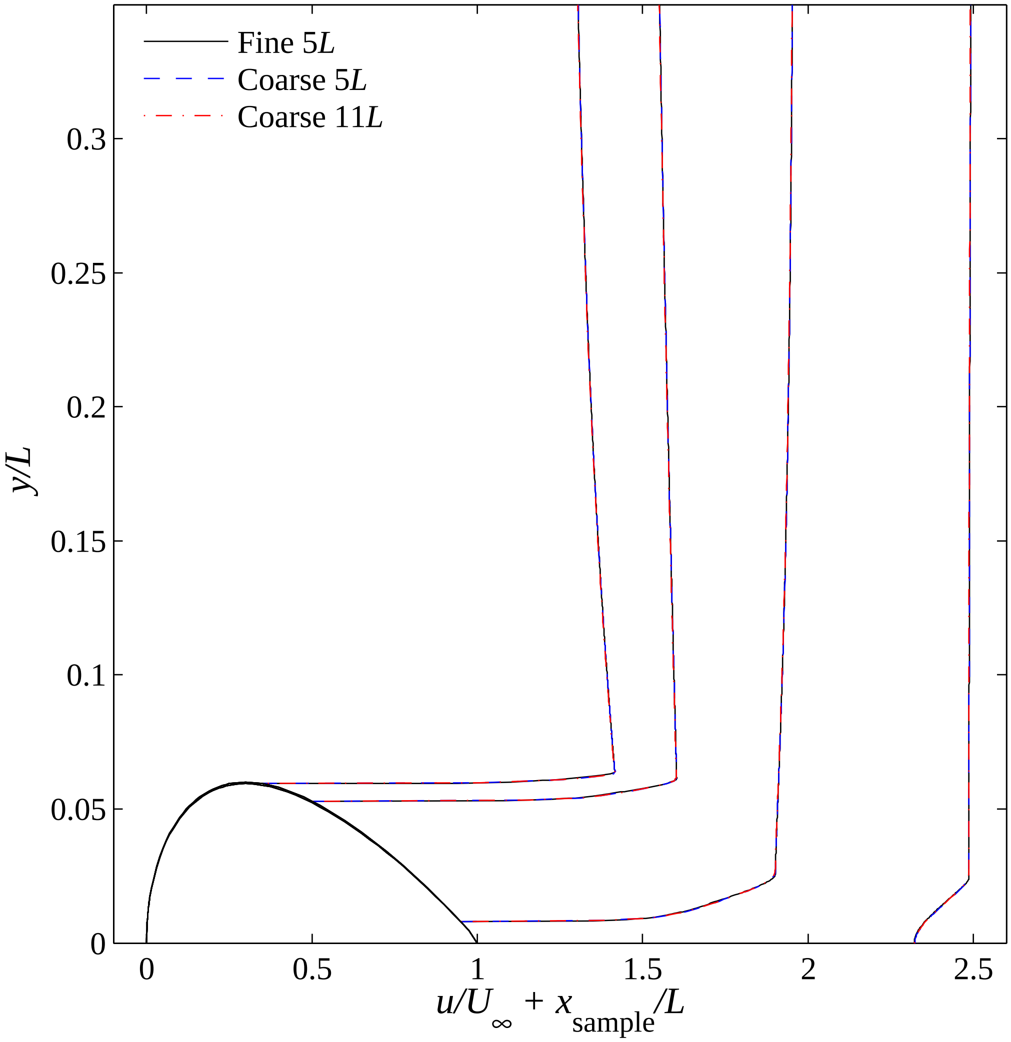

Figure 5.5: Velocity profiles at $x/L = 0.25, 0.5, 0.95$, and 1.5 from the RANS solver for flow over a NACA 0012 airfoil at $\mathrm{Re} = 6 \times 10^6$.

5.2.2 Velocity Decomposition Parameters

In the interest of demonstrating the ability of the velocity decomposition solver without completing a study of the parameters, the parameters were selected for the NACA 0012 airfoil based on their effects in the laminar flat plate and circular cylinder cases, and the turbulent flat plate case. The parameters selected to be used in the velocity decomposition solver on the reduced domain for the turbulent NACA 0012 airfoil case are summarized in Table 5.9.

Table 5.9: Velocity decomposition solver parameters selected for flow over a NACA 0012 airfoil at Re = 6×10^6.

Parameter	Value
α_{vort}	0.01
n_{wp}	11
w_{s}/L	0.1
w_{g}	0.25
# of iterations	3
res_{update}	1.0x10^{-4}
# of updates	3

5.2.3 Velocity Decomposition Results

The coarse $5L$ domain used for the RANS solver was trimmed to extend $0.3L$ in the inlet and farfield directions. The vorticity thickness, defined as the distance for the maximum vorticity on the normal to drop two orders of magnitude, is approximately $0.02L$ at the end of the airfoil, and $0.15L$ at the outlet of the computational domain. The reduced domain extends approximately two times the vorticity thickness at the outlet of the domain.

The domain reduction decreased the number of cells by 43%, from 64,960 to 37,120. The parameters summarized in Table 5.9 are used in the velocity decomposition solver. The values of δ_{max} are $0.05L$ on the body and $0.1L$ in the wake. These limits allow the desired vorticity decrease to be found on all but one panel.

Velocity profiles at $x/L = 0.25, 0.5, 0.95$, and 1.5 are shown for the velocity decomposition solver on the coarse $0.3L$ mesh and the RANS solver on the coarse $5L$ mesh in Figure 5.6. The solutions visually match very well in the velocity profiles. The RMS error in the x-component of the velocity, u, at ten points located at $y/L = 0.065$ and 0.09 and $x/L = 0.05, 0.25, 0.5, 0.95$, and 1.5 is 0.03%, as shown in Table 5.10. The velocity fields from the velocity decomposition solver and the RANS solver match quite well. The error in the drag coefficient is 1.5%, which is similar to the error of

1.4% between the drag coefficients on the coarse $5L$ mesh and the fine $5L$ mesh from the RANS solver. The error between the drag coefficients from the velocity decomposition solver on the coarse $0.3L$ mesh and the RANS solver on the fine $5L$ mesh is only 0.1%. The velocity decomposition solver on the coarse $0.3L$ mesh provides a more accurate solution than the RANS solver on the coarse $5L$ mesh.

For this case, the velocity residuals were required to fall below 1.0×10^{-8} and the pressure, turbulent kinetic energy, and specific dissipation rate residuals were required to fall below 1.0×10^{-6}. The computation time is reduced from 4,430 seconds for the RANS solver to 2,180 seconds for the velocity decomposition solver, representing a decrease of 51%.

Table 5.10: Velocity decomposition solver on $0.3L$ domain compared to RANS solver on $5L$ domain for flow over a NACA 0012 airfoil at $\mathrm{Re} = 6 \times 10^6$.

# of cells RANS	64,960
# of cells Vel. Decomp.	37,120
Decrease in # of Cells	43%
RMS u error	0.030%
RANS Cd	0.007604
Vel. Decomp. Cd	0.007718
Cd Error	1.5%
RANS Time (sec)	4,430
Vel. Decomp. Time (sec)	2,180
Decrease in Time	51%

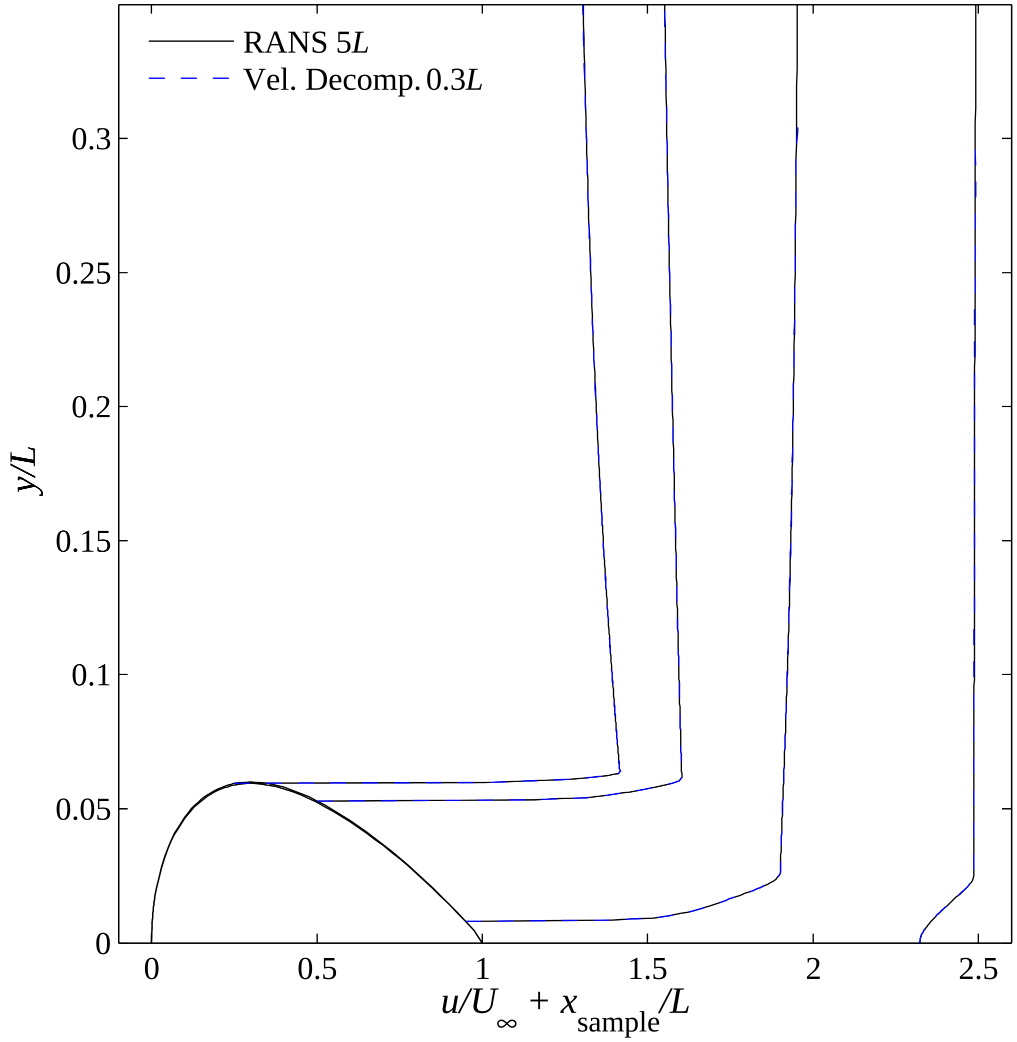

Figure 5.6: RANS and velocity decomposition velocity profiles for flow over a NACA 0012 airfoil at $\mathrm{Re} = 6 \times 10^6$.

CHAPTER VI

Three-Dimensional Results

Results for steady laminar and turbulent flow over the Afterbody 1 are presented. The Afterbody 1 is an axisymmetric body with a fine convex stern that has been studied experimentally (Huang et al. 1976). Figure 6.1 shows the profile of the Afterbody 1. Since the Afterbody 1 is axisymmetric and we expect the flow field to also be axisymmetric, it could be simplified to a two-dimensional problem; however, we are using it to demonstrate the ability of the velocity decomposition solver to handle three-dimensional cases, so the full body and domain were discretized and solved in three-dimensions. The RANS solver is used to generate solutions with which to compare the velocity decomposition solver results.

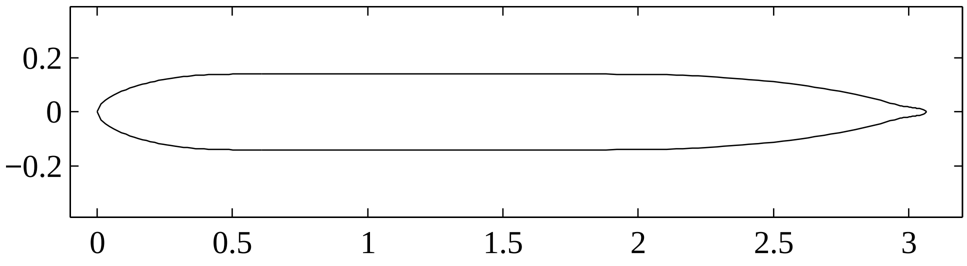

Figure 6.1: Afterbody 1 profile.

The laminar problem is stated and the RANS solution is developed. The velocity decomposition parameters are discussed and the velocity decomposition solver solution is compared to the RANS solver solution. The turbulent flow problem is then described. The velocity decomposition solver parameters are established, and the velocity decomposition solver results are compared to both the RANS solver and the experimental data of Huang et al (1978).

6.1 Laminar Afterbody 1

Laminar flow over the Afterbody 1 at a Reynolds number of 2000 based on the body length was simulated with a RANS solver and the velocity decomposition solver. The computational domain and coarse $20L$ mesh used for the RANS solver are shown in Figure 6.2, where $L = 3.066$ m is the body length. The reduced domain used for the velocity decomposition solver is outlined to show the scale of the reduction. The body is centered on the $x-$axis from $x = 0$ to $x = 3.066$.

For the RANS solver, the velocity is set equal to the free-stream velocity, $U_\infty = 0.0006523$ m/s, at the inlet and farfield boundaries, and zero at the wall. The outlet pressure is set to zero to serve as the reference pressure. The velocity at the outlet, and the pressure at the inlet, farfield, and wall are calculated to achieve zero normal gradient. The pressure field is initially set to zero, and the velocity is initially set equal to the free-stream velocity.

The only modification to the boundary conditions for the velocity decomposition solver is that the fluid velocity at the inlet and farfield boundaries is set equal to the potential velocity.

6.1.1 RANS Domain Dependence Study

To ensure the accuracy of the RANS solution used to validate the velocity decomposition solver, a study of the computational domain resolution and extent was performed. Coarse and fine structured meshes extending 19 body lengths in the inlet direction, 21 body lengths in the farfield directions, and 39 body lengths in the out-

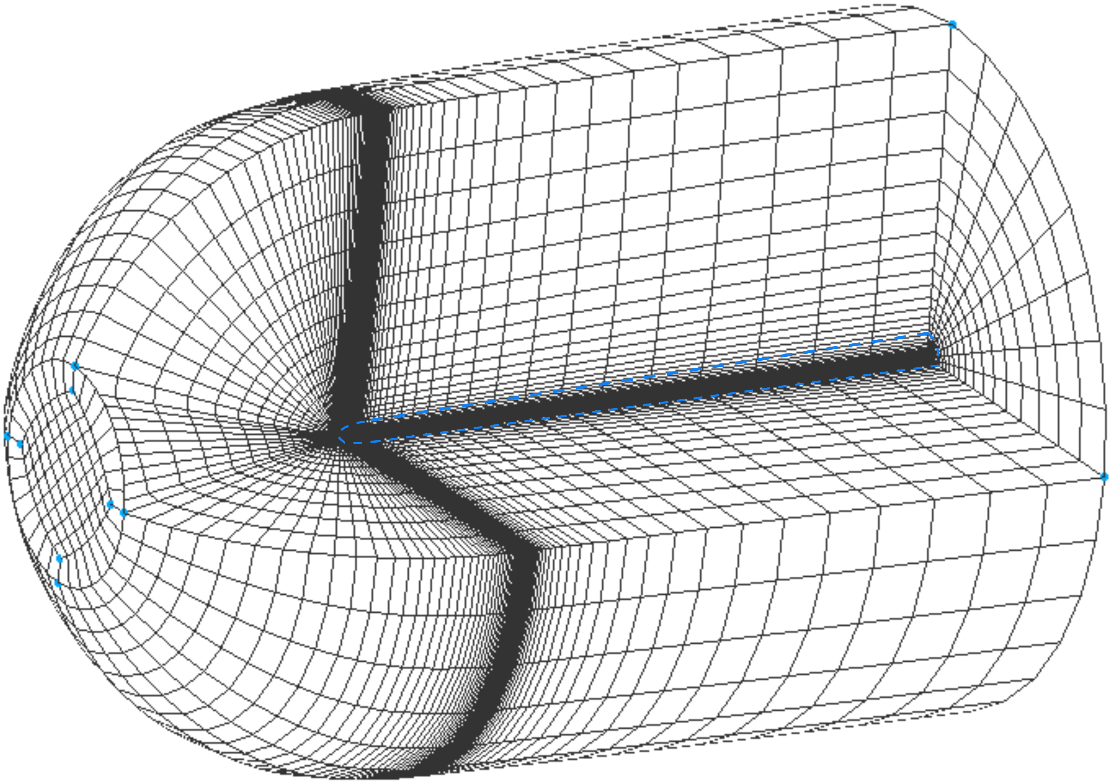

Figure 6.2: Laminar Afterbody 1 coarse $20L$ mesh with the reduced $0.7L$ domain outlined by the blue dashed line.

let direction from the body were systematically created by doubling the resolution. These meshes will be referred to as $20L$ meshes. Center cones in the meshes extending from the front of the body to the inlet and from the back of the body to the outlet allow the application of quadrilateral panels on the front and back of the body. Table 6.1 provides the mesh resolution given as the number of cells along the outlet from the center cone to the farfield boundary by the number of cells axially along the inlet and farfield boundaries by the number of cells forming the ring around the body. The number of panels on the body, total number of cells, and mesh refinement factor are also provided in Table 6.1. The domain extents of the coarse mesh were extended to 37 body lengths in the inlet direction and 39 body lengths in the farfield direction while leaving the outlet extent at 39 body lengths. This extended mesh will be referred to as the $40L$ mesh.

Table 6.1: Laminar Afterbody 1 mesh characteristics.

Mesh	Resolution	Body panels	# of Cells	$r_j = h_j/h_{\text{fine}}$
Fine $20L$	76 x 202 x 64	8,704	974,080	1.0
Coarse $20L$	38 x 101 x 32	2,176	121,760	2.0
Coarse $40L$	43 x 101 x 32	2,176	138,240	3.2

Velocity profiles at $x/L = 0.05, 0.25, 0.5, 0.95$, and 1.5 from the two mesh resolutions on the $20L$ domain, and the coarse $40L$ domain are shown to match well in Figure 6.3. Note that r is the radial coordinate. The error in the drag coefficient and the RMS of the error in the x-component of the velocity, u, at ten points located at $r/L = 0.098$ and 0.16 and $x/L = 0.05, 0.25, 0.5, 0.95$, and 1.5 with respect to the fine mesh solution are provided in Table 6.2. The errors with respect to the next finer or smaller mesh, and the drag coefficient values are also provided in Table 6.2. All of the errors are less than 0.2%. The error in the drag coefficient between the coarse $20L$ mesh and the fine $20L$ mesh is 0.10%, and the error between the coarse $40L$ mesh and the coarse $20L$ mesh is 0.00095%, so the coarse $20L$ mesh appears to sufficiently capture the solution and will be used as the standard against which to compare the velocity decomposition solver results.

Table 6.2: Laminar Afterbody 1 at Re = 2000 drag coefficients and error in RANS solver due to domain resolution and extent.

Mesh	Cd	Cd error w/fine	Cd relative error	RMS velocity error w/ fine	RMS velocity relative error
Fine $20L$	0.1266				
Coarse $20L$	0.1265	0.10%	0.10%	0.18%	0.18%
Coarse $40L$	0.1265	0.11%	0.00095%	0.18%	0.0095%

6.1.2 Velocity Decomposition Parameters

The velocity decomposition solver parameter studies on the laminar flat plate and circular cylinder, and the turbulent flat plate were used to guide the selection

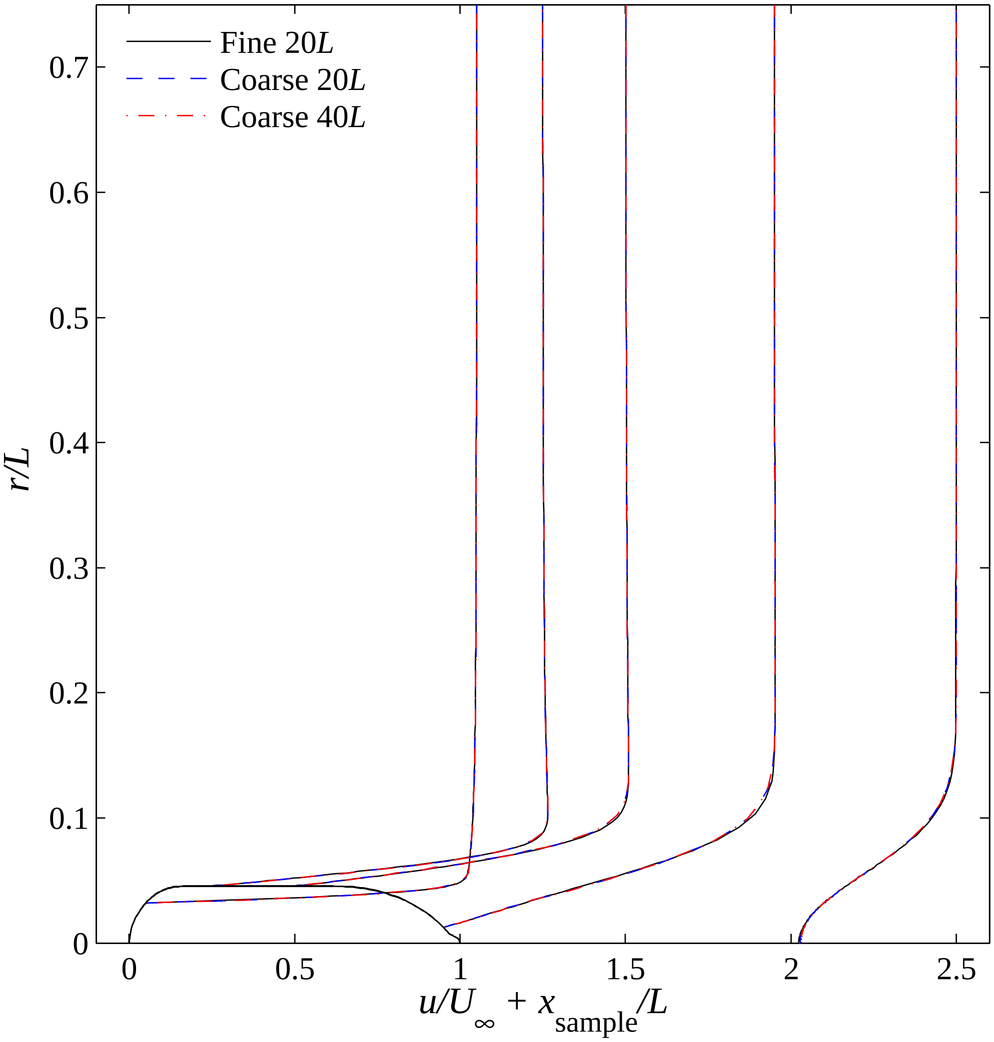

Figure 6.3: Velocity profiles at $x/L = 0.05, 0.25, 0.5, 0.95$, and 1.5 from the RANS solver for laminar flow over the Afterbody 1 at Re = 2000.

of parameters for the Afterbody 1. The ability of the velocity decomposition solver to function without wake sources is demonstrated by this case. The selected parameters for the velocity decomposition solver on the reduced domain for the laminar Afterbody 1 case are summarized in Table 6.3.

Table 6.3: Velocity decomposition solver parameters selected for flow over the Afterbody 1 at Re = 2000.

Parameter	Value
α_{vort}	0.01
n_{wp}	0
w_{s}/L	–
w_{g}	–
# of iterations	2
res_{update}	1.0x10^{-4}
# of updates	2

6.1.3 Velocity Decomposition Results

The coarse $20L$ domain used for the RANS solver was trimmed to extend $0.69L$ from the body in the inlet direction and $0.78L$ from the body in the farfield direction, which corresponds to a farfield extent of $1.5L$ from the centerline at the outlet. The outlet extent was not modified from $39L$. The reduced domain is referred to as the coarse $0.7L$ mesh. The vorticity thickness is approximately $0.2L$ at the end of the body, and $0.8L$ at the outlet of the computational domain. The reduced domain extends approximately two times the vorticity thickness at the outlet of the domain.

The domain reduction decreased the number of cells by 41%, from 121,760 to 72,320. The value of δ_{max} is $0.57L$ on the body. The desired vorticity decrease is found for all of the body panels using this limit.

Velocity profiles at $x/L = 0.05, 0.25, 0.5, 0.95$, and 1.5 are shown for the velocity decomposition solver on the coarse $0.7L$ mesh and the RANS solver on the coarse $20L$ mesh in Figure 6.4. The solutions visually match well in the velocity profiles. The RMS error in the x-component of the velocity, u, at ten points located at $r/L = 0.098$ and 0.16 and $x/L = 0.05, 0.25, 0.5, 0.95$, and 1.5 is 0.12%, as shown in Table 6.4. The error between the drag coefficients is 0.23%. The velocity fields and drag coefficients indicate the velocity decomposition solver matches the RANS solver well. The velocity decomposition solver performs well without wake sources in this case.

To evaluate the computation time, the velocity residuals were required to fall below 1.0×10^{-10} and the pressure residual was required to fall below 1.0×10^{-8}. The computation time is reduced from $1,599.8$ seconds for the RANS solver to $1,302.5$ seconds for the velocity decomposition solver, representing a decrease of 18.6%.

Table 6.4: Velocity decomposition solver on $0.7L$ domain compared to RANS solver on $20L$ domain for flow over the Afterbody 1 at Re $= 2000$.

# of cells RANS	121,760
# of cells Vel. Decomp.	72,320
Decrease in # of Cells	41%
RMS u error	0.12%
RANS Cd	0.1265
Vel. Decomp. Cd	0.1268
Cd Error	0.23%
RANS Time (sec)	1,599.8
Vel. Decomp. Time (sec)	1,302.5
Decrease in Time	18.6%

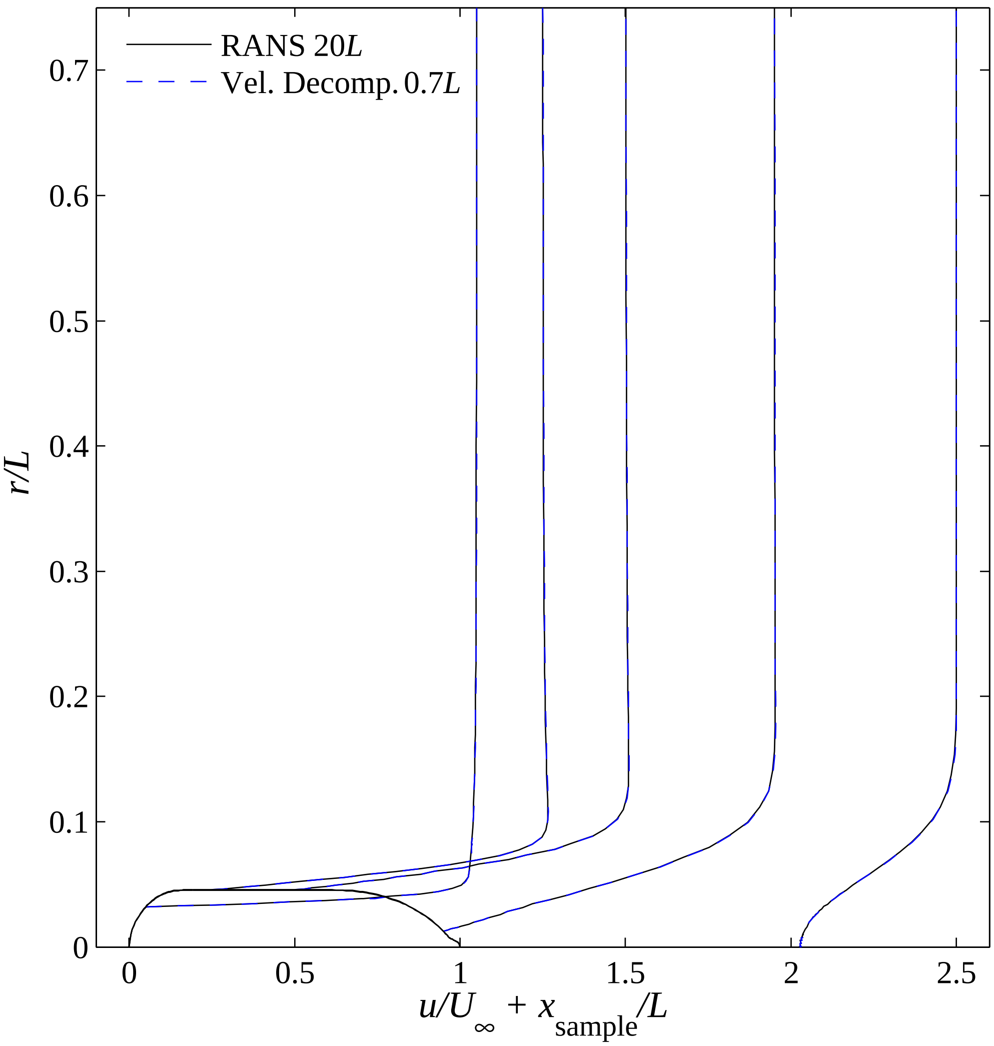

Figure 6.4: RANS and velocity decomposition velocity profiles for flow over the Afterbody 1 at Re = 2000.

6.2 Turbulent Afterbody 1

Turbulent flow over the Afterbody 1 at a Reynolds number of 6.6×10^6 based on the body length was modeled with a RANS solver and the velocity decomposition solver. The results are compared to the experimental results of Huang et al. (1978). The fine $20L$ mesh presented in the laminar Afterbody 1 case is used for the RANS solver. The computational domain for the fine $20L$ mesh is the same as the domain shown in Figure 6.2, and the resolution is doubled from the coarse mesh shown. The body length is $L = 3.066$ m, as in the laminar case.

For the RANS solver, the velocity is set equal to the free-stream velocity, $U_\infty = 30.48$ m/s, at the inlet and farfield boundaries, and zero at the wall. The outlet pressure is set to zero to serve as the reference pressure. The velocity at the outlet, and the pressure at the inlet, farfield, and wall are calculated to achieve zero normal gradient. The pressure field is initially set to zero, and the velocity is initially set equal to the free-stream velocity.

The $k-\omega$ SST turbulence model is used. The free-stream turbulent kinetic energy used as the initial condition and the boundary condition on the inlet and farfield boundaries is calculated using Equation 5.1 with a turbulence intensity of $I = 0.1\%$ based on the experimental measurements (Huang et al. 1978). The kinematic eddy viscosity is initially set equal to ten times the kinematic viscosity, $\nu_t = 10\nu$. The free-stream value of the specific dissipation rate, ω, used for the initial condition and the inlet and farfield boundary conditions, is set according to the relation $\omega = k/\nu_t$. Wall functions are used.

The only modification to the boundary conditions for the velocity decomposition solver is that the fluid velocity at the inlet and farfield boundaries is set equal to the potential velocity.

6.2.1 Velocity Decomposition Parameters

The velocity decomposition solver parameter studies on the laminar flat plate and circular cylinder, and the turbulent flat plate were used to guide the selection of parameters for the Afterbody 1. The ability of the velocity decomposition solver without wake sources is demonstrated by this case. The selected parameters are the same as those used in the laminar Afterbody 1 case presented previously, as summarized in Table 6.5.

Table 6.5: Velocity decomposition solver parameters selected for flow over the Afterbody 1 at Re = 6.6×10^6.

Parameter	Value
α_{vort}	0.01
n_{wp}	0
w_{s}/L	–
w_{g}	–
# of iterations	2
res_{update}	$1.0\text{x}10^{-4}$
# of updates	2

6.2.2 Velocity Decomposition Results

The fine $20L$ mesh presented in the laminar Afterbody 1 case is used for the RANS solver. A reduced domain for the velocity decomposition solver was created by trimming the fine $20L$ mesh to extend $0.12L$ from the body in the inlet direction and $0.13L$ from the body in the farfield direction, which corresponds to a farfield extent of $0.35L$ from the centerline at the outlet. The outlet extent was not modified from $39L$. The reduced domain is referred to as the fine $0.1L$ mesh, and is shown in Figure 6.5 with the outlet extent truncated. The vorticity thickness is approximately $0.05L$ at the end of the body, and $0.2L$ at the outlet of the computational domain. The reduced domain extends less than two times the vorticity thickness at the outlet of the domain.

The domain reduction decreased the number of cells by 61%, from 974,080 to 380,800. The value of $\delta_{\max}$ is $0.10L$ on the body.

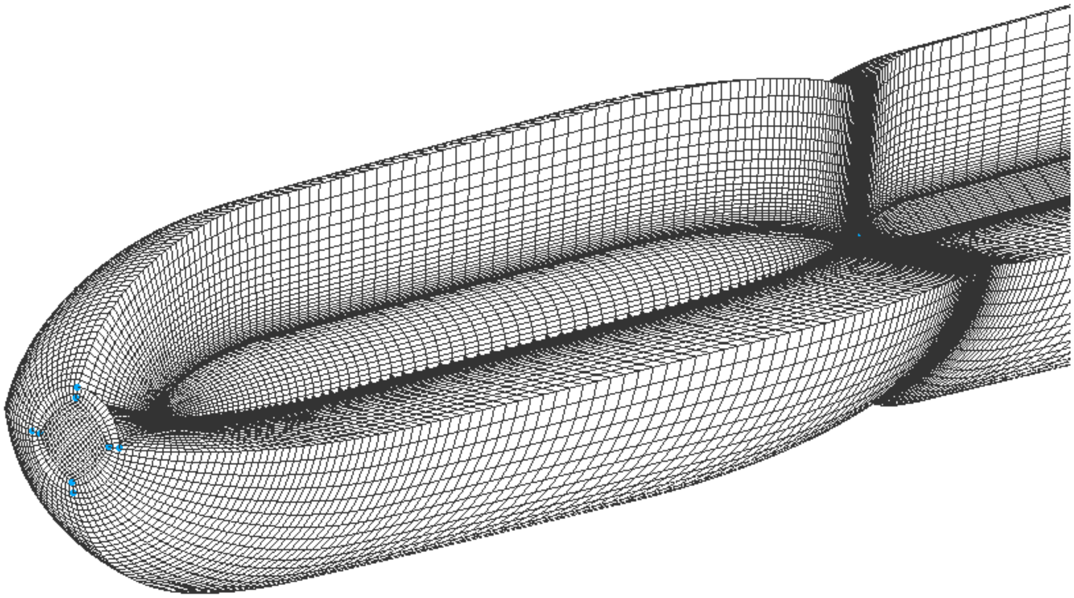

Figure 6.5: Turbulent Afterbody 1 fine $0.1L$ mesh around the body with the outlet extent truncated.

Velocity profiles at $x/L = 0.755, 0.914, 0.977$, and 1.057 are shown for the velocity decomposition solver on the fine $0.1L$ mesh and the RANS solver on the fine $20L$ mesh in Figure 6.6. Experimental data from Huang et al. (1978) is also included in Figure 6.6. The velocity decomposition solver matches the RANS solver result very well, and both computational results are close to the experimental data from Huang et al. (1978). The RMS errors with respect to the experimental data in the x-component of the velocity, u, for the RANS solver and the velocity decomposition solver are 1.75% and 1.70% respectively, as shown in Table 6.6. The locations of the eight points used to determine the RMS velocity error are shown in Table 6.7. The error between the drag coefficients from the RANS solver and the velocity decomposition solver is 0.70%. The velocity fields and drag coefficients demonstrate good agreement between the velocity decomposition solver and the RANS solver. The velocity data also indicate that the velocity decomposition and RANS solvers match the experimental data equally well.

The velocity residuals were required to fall below 1.0×10^{-10} and the pressure, turbulent kinetic energy, and specific dissipation rate residuals were required to fall below 1.0×10^{-8}. The computation time is reduced from 8.92 hours for the RANS solver to 4.39 hours for the velocity decomposition solver, representing a decrease of 50.8%.

Table 6.6: Velocity decomposition solver on $0.1L$ domain compared to RANS solver on $20L$ domain and the experimental work of Huang et al. (1978) for flow over the Afterbody 1 at Re $= 6.6 \times 10^6$.

# of cells RANS	974,080
# of cells Vel. Decomp.	380,800
Decrease in # of Cells	61%
RANS RMS u error (with exp.)	1.75%
Vel. Decomp. RMS u error (with exp.)	1.70%
RANS Cd	0.008196
Vel. Decomp. Cd	0.008253
Cd Error (Vel. Decomp. & RANS)	0.70%
RANS Time (hrs)	8.92
Vel. Decomp. Time (hrs)	4.39
Decrease in Time	50.8%

Table 6.7: Points used to sample the turbulent Afterbody 1 velocity field.

x/L	r/L
0.755	0.0493
0.755	0.0819
0.914	0.0333
0.914	0.0729
0.977	0.0195
0.977	0.0735
1.057	0.0177
1.057	0.0665

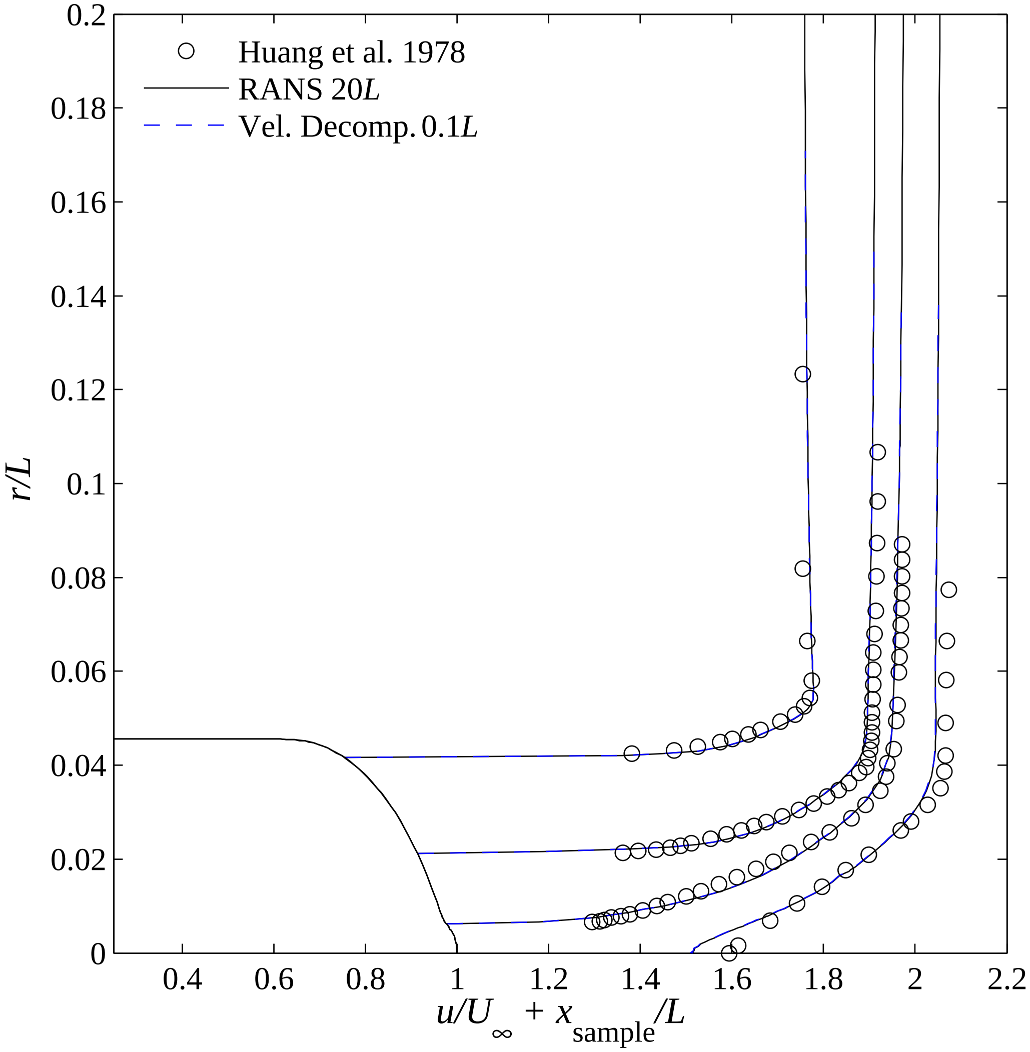

Figure 6.6: RANS and velocity decomposition velocity profiles for flow over the Afterbody 1 at $\mathrm{Re} = 6.6 \times 10^6$.

CHAPTER VII

Contributions and Future Work

7.1 Contributions

The velocity decomposition approach presented in this thesis is a novel numerical implementation of a mechanism to include the effects of viscosity in the potential velocity through the body boundary condition coupled with the use of the viscous potential velocity to specify the inlet and farfield boundary conditions on computational domains extending just beyond the vortical region. The velocity decomposition solver was developed, implemented, and demonstrated in this work.

The velocity decomposition solver has matched the accuracy of a RANS solver in decreased computation time for a variety of steady, two-dimensional and three-dimensional, laminar and turbulent, external, incompressible flows. The computation time was reduced between 3% and 68% for the cases studied in this thesis. A description of the effects of the velocity decomposition solver parameters is provided for a variety of flows. The parameter studies presented have successfully guided the selection of parameters for other cases.

The inclusion of the effects of viscosity in the viscous potential velocity through the body boundary condition allows the viscous potential velocity to fully capture the real fluid velocity outside of the vortical region. Wake sources improve the ability of the viscous potential velocity to match the total fluid velocity. The novel numerical implementation of this body boundary condition was demonstrated to work well for a variety of flows in this work.

The benefits of decomposing the velocity were determined to be fully available through its application to the boundary conditions. Solving the RANS equations rather than the complementary RANS equations of Kim et al. (2005) reduces the number of terms and allows the utilization of any of the techniques developed to solve the RANS equations.

The velocity decomposition method presented in this thesis utilizes the strengths of both RANS solvers and potential flow solvers to provide the benefits of each in a unified methodology. Applying the velocity decomposition to the body boundary condition allows the effects of viscosity to be included in the viscous potential velocity field. The viscous potential velocity field then fully represents the fluid velocity outside of the vortical region surrounding the body and in the wake. The computational domain can therefore be reduced to extend just beyond the vortical region with the viscous potential velocity acting as the inlet and farfield boundary conditions for the total fluid velocity. The accuracy of the RANS solver is maintained in the velocity decomposition solver while the computational cost is decreased due to the reduction of the domain size. Further time savings will be achieved as mesh generation for smaller domains is also less time consuming.

7.2 Future Work

The velocity decomposition approach can accurately and efficiently handle deeply submerged, steady, two-dimensional and three-dimensional, laminar and turbulent, external, incompressible flows over rigid bodies without lift. The formulation of the velocity decomposition method should also apply directly to bodies with lift and multi-body problems; the implementation of the solver, and particularly of the potential velocity, will require modifications in these cases. With minor adjustments to the theoretical formulation and the numerical implementation, the velocity decomposition approach may also offer improved computational efficiency for compressible flows, unsteady problems, and free-surface flows around bodies. The computational efficiency of the velocity decomposition solver may be improved by the implementation of more efficient potential solution methods, and improvements in the coding structure.

Flows over bodies with lift, such as airfoils at an angle of attack, bodies near a free surface, or ships at a yaw angle, are among the possible applications of the velocity decomposition solver. The formulation applies directly; however, we expect a lifting potential, or a potential that includes vorticity, to be necessary to allow significant domain reduction.

Problems involving multiple bodies, such as multi-hull ships and passing vessels, are another exciting possible application of the velocity decomposition method. Rather than discretizing the fluid flow in a large domain that encompasses all of the bodies, the flow can be modeled in small domains surrounding each body individually. The influence of each body on the others would be included in the viscous potential velocity that acts as the inlet and farfield boundary conditions for the RANS solution around each body.

The velocity decomposition approach may also be utilized for compressible flows in the aeronautical and automotive industries. The viscous potential velocity body boundary condition formulation is theoretically applicable to compressible flows if the vortical velocity is solenoidal (Morino 1986, Appendix C).

Unsteady problems of interest may include maneuvering ships and bodies with relative motion. The velocity decomposition method should be applicable to unsteady flows using either a steady potential based on the average total velocity components, or an unsteady potential velocity. In turbulent cases and other cases where the unsteadiness is primarily limited to the vortical regions, it may be preferable to apply a steady potential velocity, and account for the unsteadiness in the vortical velocity term. If the unsteadiness is present throughout the domain, including the areas with negligible vorticity where the potential velocity should fully capture the total velocity, an unsteady potential velocity will probably be necessary. The velocity decomposition solver may be implemented with models other than RANS, such as large eddy simulations.

Bodies on or near a free-surface, or other problems with complex farfield boundary conditions, are particularly well suited for the velocity decomposition method. These problems may include ships, submarines, offshore wind platforms, and bodies in experimental towing facilities with wave generation, among others. The potential velocity solution must be modified to include the free surface. A submerged body at a finite depth may be studied by including the effects of the free surface through the potential velocity on the inlet and farfield boundaries of a computational domain that surrounds the vortical regions around the body and in the wake. The extent of the flow domain between the vortical region and the free surface does not need to be discretized to include the presence of the free surface. Free-surface problems are being studied using the velocity decomposition method presented in this work with the addition of desingularized sources above the free-surface and collocation points along the numerically predicted free-surface for bodies at a finite depth with promising results (Rosemurgy et al. 2012).

APPENDIX

APPENDIX A

RANS Discretization Error

The ASME (Celik et al. 2008) procedure and a similar procedure utilizing a least squares fit presented by Eça and Hoekstra (2006) are used to estimate the uncertainty due to discretization. The drag coefficient for laminar flow over a NACA 0012 airfoil at a Reynolds number of 2000 is used to analyze the uncertainty.

Six meshes were generated using systematic refinement. Table A.1 includes the mesh resolution expressed as the number of cells along one side of the inlet and farfield boundaries by the number of cells across the outlet, the total number of cells, the representative mesh size h, and the grid refinement factor $r = h_j/h_{\text{fine}}$ where j is the mesh being evaluated. The representative mesh size h is defined for the two-dimensional case by

$$h = \left[\frac{1}{N} \sum_{i=1}^{N} \Delta A_i \right]^{1/2} \tag{A.1}$$

where N is the number of cells in the mesh and ΔA_i is the area of the ith cell.

ASME procedure

The ASME procedure determines the discretization error based on the value of the variable of interest from simulations on three systematically refined meshes. The

Table A.1: Laminar NACA 0012 airfoil mesh characteristics for the discretization uncertainty analysis.

Mesh	Resolution	# of Cells	h	$r_j = h_j/h_{\text{fine}}$
Fine	302 x 398	120,196	0.111	1.00
Medium-Fine	226 x 298	67,348	0.148	1.34
Medium	150 x 198	29,700	0.222	2.01
Coarse-Medium	112 x 148	16,576	0.298	2.69
Coarse	74 x 98	7,252	0.450	4.07
Coarsest	36 x 48	1,728	0.919	8.32

procedure was applied to the four possible sets of consecutive meshes presented in Table A.1. The results for the coarse-medium, medium, and medium-fine meshes are presented since this set of three meshes has an observed order of accuracy of 1.3 which is in the expected range of 1.0 to 2.0, and consequently indicates that it is in the asymptotic range. The observed order of accuracy for the other sets exceeded the theoretical value of 2.0, which may be due to not being in the asymptotic range, and for the set of the three finest meshes, may be due to the small error between the drag coefficients for the fine and medium-fine meshes. Being in the asymptotic range indicates that the variable is approaching an asymptotic numerical value, and hence the leading order of error dominates. The meshes are assigned the indices 1, 2, and 3 with 1 corresponding to the finest mesh. The relative grid refinement factors are defined as $r_{21} = h_2/h_1$ and $r_{32} = h_3/h_2$, and are reported in Table A.2. The observed or apparent order of accuracy, $p = 1.3$, was calculated using fixed point iteration to solve the following set of equations.

$$p = \frac{1}{\ln(r_{21})} \left| \ln \left| \frac{\phi_3 - \phi_2}{\phi_2 - \phi_1} \right| + q(p) \right| \tag{A.2}$$

$$q(p) = \ln \left(\frac{r_{21}^p - s}{r_{32}^p - s} \right) \tag{A.3}$$

$$s = 1 \cdot \mathrm{sgn} \left(\frac{\phi_3 - \phi_2}{\phi_2 - \phi_1} \right) \tag{A.4}$$

where ϕ_j is the drag coefficient on the jth mesh. The value of s was positive, indicating monotonic convergence. The extrapolated value ϕ_{ext}^{21} of the drag coefficient is then computed as

$$\phi_{\text{ext}}^{21} = \frac{r_{21}^p \phi_1 - \phi_2}{r_{21}^p - 1} \tag{A.5}$$

The relative error between the two finer meshes, e_{rel}^{21}, extrapolated relative error between the extrapolated value and the value on the finest mesh, e_{ext}^{21}, and the fine-grid convergence index, $\text{GCI}_{\text{fine}}^{21}$, are defined as follows. Please note that 'fine' here refers to the finest mesh in the set of three used for this analysis, which corresponds to the medium-fine mesh presented in Table A.1.

$$e_{\text{rel}}^{21} = \left| \frac{\phi_1 - \phi_2}{\phi_1} \right| \qquad \text{Relative error} \tag{A.6}$$

$$e_{\text{ext}}^{21} = \left| \frac{\phi_{\text{ext}}^{21} - \phi_1}{\phi_{\text{ext}}^{21}} \right| \qquad \text{Extrapolated relative error} \tag{A.7}$$

$$\text{GCI}_{\text{fine}}^{21} = \frac{F_s e_{\text{rel}}^{21}}{r_{21}^p - 1} \qquad \text{Fine} - \text{grid convergence index} \tag{A.8}$$

Table A.2: ASME discretization uncertainty values for the traditional RANS solver based on flow over a NACA 0012 airfoil at Re = 2000 using the medium-fine, medium, and coarse-medium meshes.

Property	Value
r_{21}	1.506
r_{32}	1.338
Cd_1	0.08348
Cd_2	0.08351
Cd_3	0.08354
p	1.299
$\mathrm{Cd}_{\mathrm{ext}}$	0.08345
e^{21}_{rel}	0.03042%
e^{21}_{ext}	0.04339%
$\mathrm{GCI}^{21}_{\mathrm{fine}}$	0.05421%

where F_s is a safety factor which is usually taken as 1.25. The GCI represents the numerical uncertainty in the solution on a given mesh. The values of the extrapolated drag coefficient and the three forms of error are presented in Table A.2.

Least squares procedure

Eça and Hoekstra (2006) present a very similar procedure to estimate the discretization uncertainty based on a least squares version of the grid convergence index (GCI). The elements are essentially the same, only a least squares approach is used rather than the fixed point iteration. This difference allows the use of more than three meshes. Their procedure uses the GCI to define the discretization uncertainty U as

$$U = F_s|\delta_{RE}| \tag{A.9}$$

where F_s is a safety factor as in the ASME procedure, and δ_{RE} is an estimate of the error using Richardson extrapolation:

$$\delta_{RE} = \phi_j - \phi_o = \alpha h_i^p \tag{A.10}$$

ϕ_o is the estimated exact solution which is similar to ϕ_{ext}^{21} in the ASME procedure, and α is a constant. The values for p, ϕ_o, and α are determined using a least squares root approach that minimizes the function

$$S(\phi_o, \alpha, p) = \sqrt{\sum_{j=1}^{n_m} \left(\phi_j - \left(\phi_o + \alpha h_j^p\right)\right)^2} \tag{A.11}$$

where n_m is the number of meshes available. The four finest meshes presented in Table A.1 are used in this procedure since including the coarser meshes leads to values of the observed order of accuracy over 2.0 which indicate that they may not be in the asymptotic range, as was mentioned with the ASME procedure. The standard deviation, U_s, of the least squares root fit is calculated as

$$U_s = \sqrt{\frac{\sum_{j=1}^{n_m} \left(\phi_j - \left(\phi_o + \alpha h_j^p\right)\right)^2}{n_m - 3}} \tag{A.12}$$

To check for oscillatory convergence, p^* is determined using $\phi_j^* = |\phi_{j+1} - \phi_j|$ in Equation (A.11). Monotonic convergence is observed in this case, as indicated by a positive value of both p and p^*. The uncertainty for this case, where $0.95 \leq p \leq 2.05$, is calculated as

$$U_\phi = F_s|\delta_{RE}| + U_s \tag{A.13}$$

where the safety factor has a value of 1.25 as in the ASME procedure.

The observed order of accuracy using the least squares approach on the four finest meshes is 1.7, which is close to the theoretical value of 2.0. The numerical uncertainty for the drag coefficient on the fine mesh, $U_{\text{Cd}}^{\text{fine}}$, is 0.002028%. The values of the drag coefficient on the four meshes, the extrapolated value, $C_{d,\text{ext}}$, and the uncertainties are provided in Table A.3.

Table A.3: Least squares root discretization uncertainty values for the traditional RANS solver based on flow over a NACA 0012 airfoil at Re = 2000 using the fine, medium-fine, medium, and coarse-medium meshes.

Property	Value
$\mathrm{Cd}_{\mathrm{fine}}$	0.08348
$\mathrm{Cd}_{\mathrm{medium-fine}}$	0.08348
$\mathrm{Cd}_{\mathrm{medium}}$	0.08351
$\mathrm{Cd}_{\mathrm{coarse-medium}}$	0.08354
p	1.664
$\mathrm{Cd}_{\mathrm{ext}}$	0.08346
U_s	9.020×10^{-7}
$U_{\mathrm{Cd}}^{\mathrm{fine}}$	0.002028%

Summary

The ASME procedure provided an observed order of accuracy of $p = 1.3$ and a numerical uncertainty of $\mathrm{GCI}_{\mathrm{fine}}^{21} = 0.05\%$. The least squares root procedure presented by Eça and Hoekstra (2006) gave an observed order of accuracy of $p = 1.7$ and a numerical uncertainty of $U_{\mathrm{Cd}}^{\mathrm{fine}} = 0.002\%$. Both of the observed orders are close to, but lower than, the theoretical value of 2.0. The numerical uncertainties on the medium-fine grid in the ASME procedure, and the fine grid in the least squares procedure, are quite low. It should be noted that the least squares root uncertainty is not normalized by the extrapolated value as the ASME version is.

BIBLIOGRAPHY

BIBLIOGRAPHY

Celik, I., U. Ghia, P. Roache, C. Freitas, H. Coleman, and P. Raad (2008). Procedure for estimation and reporting of uncertainty due to discretization in CFD applications. *Journal of Fluids Engineering 130*.

Eça, L. and M. Hoekstra (2006). Discretization uncertainty estimation based on a least squares version of the grid convergence index. In *Proceedings of the 2nd Workshop on CFD Uncertainty Analysis*.

Eça, L. and M. Hoekstra (2009). On the numerical accuracy of the prediction of resistance coefficients in ship stern flow calculations. *Journal of Marine Science and Technology 14*(1), 2–18.

Gresho, P. and R. Sani (1987). On pressure boundary conditions for the incompressible Navier-Stokes equations. *International Journal for Numerical Methods in Fluids 7*, 1111–1145.

Hafez, M., A. Shatalov, and M. Nakajima (2007). Improved numerical simulations of incompressible flows based on viscous/inviscid interaction procedures. *Computers and Fluids 36*(10), 1588 – 91.

Hafez, M., A. Shatalov, and E. Wahba (2006). Numerical simulations of incompressible aerodynamic flows using viscous/ inviscid interaction procedures. *Computer Methods in Applied Mechanics and Engineering 195*(23-24), 3110 – 3127.

Hess, J. and A. Smith (1967). *Calculation of Potential Flow about Arbitrary Bodies.* Douglas Aircraft Company.

Huang, T., N. Santelli, and G. Belt (1978). Stern boundary-layer flow on axisymmetric bodies. In *Twelfth Symposium on Naval Hydrodynamics*. National Academy of Sciences.

Huang, T., H. Wang, N. Santelli, and N. Groves (1976). Propeller/stern/boundary-layer interaction on axisymmetric bodies: Theory and experiment. *David W. Taylor Naval Ship Research and Development Center*.

Katz, J. and A. Plotkin (2001). *Low-Speed Aerodynamics* (Second Edition ed.). Cambridge University Press.

Kendon, T. E., S. J. Sherwin, and J. M. R. Graham (2003). An irrotational/vortical split-flow approach to viscous free surface flow. In K. J. Bathe (Ed.), *Second MIT Conference on Computational Fluid and Solid Mechanics*, pp. 950–955.

Kim, K., A. I. Sirviente, and R. F. Beck (2005). The complementary RANS equations for the simulation of viscous flows. *International Journal for Numerical Methods in Fluids 48*(2), 199 – 229.

Lemmerman, L. and V. Sonnad (1979). Three-dimensional viscous-inviscid coupling using surface transpiration. *Journal of Aircraft 16*(6), 353 – 8.

Lighthill, M. J. (1958). On displacement thickness. *Journal of Fluid Mechanics 4*(04), 383–392.

Luquet, R., P. Ferrant, B. Alessandrini, G. Ducrozet, and L. Gentaz (2007). Simulation of a TLP in waves using the SWENSE scheme. In *Proceedings of the Seventeenth (2007) International Offshore and Polar Engineering Conference*, Lisbon, Portugal, pp. 1916 – 1922. The International Society of Offshore and Polar Engineers.

Luquet, R., L. Gentaz, P. Ferrant, and B. Alessandrini (2004). Viscous flow simulation past a ship in waves using the SWENSE approach. In *25th Symposium on Naval Hydrodynamics*, St. John's, Newfoundland and Labrador, Canada.

Menter, F. (1994). Two-equation eddy-viscosity turbulence models for engineering applications. *AIAA Journal 32*(8), 1598 – 605.

Menter, F. (1996). A comparison of some recent eddy-viscosity turbulence models. *Transactions of the ASME. Journal of Fluids Engineering 118*(3), 514 – 19.

Menter, F., M. Kuntz, and R. Langtry (2003). Ten years of industrial experience with the SST. *Turbulence, Heat and Mass Transfer 4*.

Morino, L. (1986). Helmholtz decomposition revisited: Vorticity generation and trailing edge condition. I - Incompressible flows. *Computational Mechanics 1*(1), 65–90.

Morino, L. (1994). Toward a unification of potential and viscous aerodynamics - boundary integral formulation. *Mathematical Concepts and Methods in Science and Engineering 44*.

Morino, L. (2003). Is there a difference between aeroacoustics and aerodynamics? An aeroelastician's viewpoint. *AIAA Journal 41*(7), 1209 – 23.

Morino, L., M. Gennaretti, and S. Shen (1995). Lighthill transpiration velocity revisited. An exact formulation. *Meccanica 30*(2), 127 – 137.

Morino, L., F. Salvatore, and M. Gennaretti (1999). New velocity decomposition for viscous flows: Lighthills equivalent-source method revisited. *Computer Methods in Applied Mechanics and Engineering 173*(3), 317–336.

Muscari, R. and A. Di Mascio (2003a). A local model for the simulation of two-dimensional spilling breaking waves. *Journal of marine science and technology 8*, 61 – 67.

Muscari, R. and A. Di Mascio (2003b). A model for the simulation of steady spilling breaking waves. *Journal of Ship Research 47*(1), 13 – 23.

Newman, J. (1977). *Marine Hydrodynamics.* The MIT Press.

Patankar, S. V. (1980). *Numerical Heat Transfer and Fluid Flow, Series in Computational and Physical Processes in Mechanics and Thermal Sciences.* Taylor & Francis.

Rempfer, D. (2006). On boundary conditions for incompressible Navier-Stokes problems. *Applied Mechanics Reviews 59*, 107–125.

Rempfer, D. (2008). Two remarks on a paper by Sani et al. *Int. J. Numer. Meth. Fluids 56*, 1961–1965.

Rhee, S. H. and F. Stern (2002). RANS model for spilling and breaking waves. *ASME Transactions 124*, 424 – 432.

Rosemurgy, W., D. Edmund, K. Maki, and R. Beck (2012). A velocity decomposition approach for steady free-surface flow. In *29th Symposium on Naval Hydrodynamics.*

Sani, R., J. Shen, O. Pironneau, and P. Gresho (2006). Pressure boundary condition for the time-dependent incompressible Navier-Stokes equations. *Int. J. Numer. Meth. Fluids 50*, 673–682.

Wilcox, D. (2006). *Turbulence Modeling for CFD* (Third Edition ed.). DCW Industries.